



Politecnico  
di Bari

Repository Istituzionale dei Prodotti della Ricerca del Politecnico di Bari

Advanced nanophotonics for gas spectroscopy

This is a PhD Thesis

*Original Citation:*

Advanced nanophotonics for gas spectroscopy / Thottoli, Ajmal. - ELETTRONICO. - (2025). [10.60576/poliba/iris/thottoli-ajmal\_phd2025]

*Availability:*

This version is available at <http://hdl.handle.net/11589/289460> since: 2025-07-15

*Published version*

DOI:10.60576/poliba/iris/thottoli-ajmal\_phd2025

Publisher: Politecnico di Bari

*Terms of use:*

(Article begins on next page)

**A doctoral thesis submitted in fulfillment of the requirements for  
a double doctoral degree**



Politecnico  
di Bari

Department of Electrical and Information Engineering

ELECTRICAL AND INFORMATION

ENGINEERING

SSD: ING-INF/02–ELECTROMAGNETIC FIELDS



**MTU**

Ollscoil Teicneolaíochta na Mumhan  
Munster Technological University

Department of Physical Science

Centre for Advanced Photonics and Process Analysis

DOCTOR OF PHILOSOPHY

**Final Dissertation**

---

**Advanced Nanophotonics for Gas  
Spectroscopy**

---

by

Ajmal Thottoli

Supervisors (POLIBA):

Prof. Antonella D’Orazio

Dr. Giovanni Magno

Supervisors (MTU):

Prof. William Whelan Curtin

Dr. Ganga Chinna Rao Devarapu

*Coordinator of Ph.D. Program:*

*Prof. Carpentieri Mario*

---

*Course n°37, 01/11/2021-30/04/2025*



Politecnico  
di Bari

Department of Electrical and Information Engineering  
ELECTRICAL AND INFORMATION ENGINEERING

Ph.D. Program

SSD: ING-INF/02 –ELECTROMAGNETIC FIELDS

Final Dissertation

---

# Advanced Nanophotonics for Gas Spectroscopy

---

by  
Ajmal Thottoli

Referees

Prof. Harold M.H Chong  
University of Southampton  
School of Electronics and Computer Science.  
Southampton, SO17 1BJ, United Kingdom.  
Email: hmhc@ecs.soton.ac.uk

Prof. Juntao Li  
State Key Laboratory of Optoelectronic Materials  
& Technologies, School of Physics,  
Sun Yat-sen University, Guangzhou 510275, China.  
Email: lij3@mail.sysu.edu.cn.

Supervisors (POLIBA):

Prof. Antonella D'Orazio

---

Dr. Giovanni Magno

Supervisors (MTU):

Dr. William Whelan Curtin

---

Dr. Ganga Chinna Rao Devarapu

---

*Coordinator of Ph.D. Program: Prof. Carpentieri Mario*



Politecnico  
di Bari

LIBERATORIA PER L'ARCHIVIAZIONE DELLA TESI DI DOTTORATO

Al Magnifico Rettore  
del Politecnico di Bari

Il sottoscritto Ajmal Thottoli nato a Kondotty, Kerala il 28/11/1996 residente a 15 Anglesea Street, Cork, Co. Cork, Irlanda T12 F883, e-mail [iamajmal.t@gmail.com](mailto:iamajmal.t@gmail.com) iscritto al 3° anno di Corso di Dottorato di Ricerca in Ingegneria Elettrica e dell'Informazione ciclo XXXVII ed essendo stato ammesso a sostenere l'esame finale con la prevista discussione della tesi dal titolo: Advanced Nanophotonics for Gas Spectroscopy

#### DICHIARA

- 1) di essere consapevole che, ai sensi del D.P.R. n. 445 del 28.12.2000, le dichiarazioni mendaci, la falsità negli atti e l'uso di atti falsi sono puniti ai sensi del codice penale e delle Leggi speciali in materia, e che nel caso ricorressero dette ipotesi, decade fin dall'inizio e senza necessità di nessuna formalità dai benefici conseguenti al provvedimento emanato sulla base di tali dichiarazioni;
- 2) di essere iscritto al Corso di Dottorato di ricerca in Ingegneria Elettrica e dell'Informazione ciclo XXXVII, corso attivato ai sensi del "Regolamento dei Corsi di Dottorato di ricerca del Politecnico di Bari", emanato con D.R. n.286 del 01.07.2013;
- 3) di essere pienamente a conoscenza delle disposizioni contenute nel predetto Regolamento in merito alla procedura di deposito, pubblicazione e autoarchiviazione della tesi di dottorato nell'Archivio Istituzionale ad accesso aperto alla letteratura scientifica;
- 4) di essere consapevole che attraverso l'autoarchiviazione delle tesi nell'Archivio Istituzionale ad accesso aperto alla letteratura scientifica del Politecnico di Bari (IRIS-POLIBA), l'Ateneo archiverà e renderà consultabile in rete (nel rispetto della Policy di Ateneo di cui al D.R. 642 del 13.11.2015) il testo completo della tesi di dottorato, fatta salva la possibilità di sottoscrizione di apposite licenze per le relative condizioni di utilizzo (di cui al sito <http://www.creativecommons.it/Licenze>), e fatte salve, altresì, le eventuali esigenze di "embargo", legate a strette considerazioni sulla tutelabilità e sfruttamento industriale/commerciale dei contenuti della tesi, da rappresentarsi mediante compilazione e sottoscrizione del modulo in calce (Richiesta di embargo);
- 5) che la tesi da depositare in IRIS-POLIBA, in formato digitale (PDF/A) sarà del tutto identica a quelle **consegnate**/inviolate/da inviarsi ai componenti della commissione per l'esame finale e a qualsiasi altra copia depositata presso gli Uffici del Politecnico di Bari in forma cartacea o digitale, ovvero a quella da discutere in sede di esame finale, a quella da depositare, a cura dell'Ateneo, presso le Biblioteche Nazionali Centrali di Roma e Firenze e presso tutti gli Uffici competenti per legge al momento del deposito stesso, e che di conseguenza va esclusa qualsiasi responsabilità del Politecnico di Bari per quanto riguarda eventuali errori, imprecisioni o omissioni nei contenuti della tesi;
- 6) che il contenuto e l'organizzazione della tesi è opera originale realizzata dal sottoscritto e non compromette in alcun modo i diritti di terzi, ivi compresi quelli relativi alla sicurezza dei dati personali; che pertanto il Politecnico di Bari ed i suoi funzionari sono in ogni caso esenti da responsabilità di qualsivoglia natura: civile, amministrativa e penale e saranno dal sottoscritto tenuti indenni da qualsiasi richiesta o rivendicazione da parte di terzi;
- 7) che il contenuto della tesi non infrange in alcun modo il diritto d'Autore né gli obblighi connessi alla salvaguardia di diritti morali ed economici di altri autori o di altri aventi diritto, sia per testi, immagini, foto, tabelle, o altre parti di cui la tesi è composta.

Luogo e data Cork, Irlanda 10/07/2025 Firma

Il/La sottoscritto, con l'autoarchiviazione della propria tesi di dottorato nell'Archivio Istituzionale ad accesso aperto del Politecnico di Bari (POLIBA-IRIS), pur mantenendo su di essa tutti i diritti d'autore, morali ed economici, ai sensi della normativa vigente (Legge 633/1941 e ss.mm.ii.),

#### CONCEDE

- al Politecnico di Bari il permesso di trasferire l'opera su qualsiasi supporto e di convertirla in qualsiasi formato al fine di una corretta conservazione nel tempo. Il Politecnico di Bari garantisce che non verrà effettuata alcuna modifica al contenuto e alla struttura dell'opera.
- al Politecnico di Bari la possibilità di riprodurre l'opera in più di una copia per fini di sicurezza, back-up e conservazione.


Luogo e data Cork, Irlanda 10/07/2025

Firma




## DECLARATION

This thesis is entirely the candidate's work, except otherwise accredited. This thesis has not been submitted for an award in any other institution.

Author's signature :   
Ajmal Thottoli

Supervisor's signature : \_\_\_\_\_  
Prof. Antonella D'Orazio

Supervisor's signature :   
Dr. William Whelan Curtin

Supervisor's signature : \_\_\_\_\_  
Dr. Giovanni Magno

Supervisor's signature : \_\_\_\_\_  
Dr. Ganga Chinna Rao Devarapu

## Acknowledgements

I would first like to thank my supervisor, Prof. Marco Grande, for his great support and guidance. He has not only been a guide, but also a wonderful person to look up to. He gave me a very good research environment, gave me chances to be part of his collaborative projects and use the right facilities. He always encouraged me to participate in international conferences, and invited talks, and workshops. He supported me in building a good career while also reminding me of the importance of family. We used every moment to talk about science and life. I learned a lot from him. You will always be in my heart with lots of love.

A big thanks goes to another great person, Prof. William. I am always surprised how he could find time for me to discuss everything, science, research, and administrative matters. He was always supportive. His constant care, support, ideas, and feedback on my publications and thesis truly helped me in finalizing my work.

I would also like to thank the head of our research group, Prof. Antonella D'Orazio, for her administrative support, which helped me continue my work smoothly. I am also thankful to Dr. Giovanni Magno for his time discussing and sharing scientific ideas, administrative support, and the many good moments we shared. He is my favorite publication reviewer, and I truly appreciate his thoughtful comments and helpful feedback.

I would also like to thank my colleague Dr. Gabriele Biagi for all our discussions about science and life. His support in improving the research at every stage was valuable. He contributed a lot to turning ideas into practical work. We spent a lot of time together in the lab, thank you for all the jokes, advice, and encouragement. Words are not enough to express my gratitude.

I would like to extend my deepest appreciation to the founding agencies, research centres, and universities whose support was instrumental in the successful completion of this work. I must acknowledge the European project H2020-ICT-37-2020 "Photonic Accurate and Portable Sensor Systems Exploiting Photo-Acoustic and Photo-Thermal Based Spectroscopy for Real Time Outdoor Air Pollution Monitoring- PASSEPARTOUT" no. 101016956, for making it possible to achieve the results presented in this study.

I would like to thank all of my colleagues at nPEG, POLIBA for their advice, kindness, and valuable discussions, especially Jesus Hernan for his constant support, care, and thoughtful conversations; Michele Paparella for his kindness and encouragement; Giovanni Piscopo for always sharing good moments and being a true partner in crime; Davide Monopoli for all the jokes, warmth, and companionship; and Carla Cantore for her help with technical tasks and friendship. I would also like to thank my AMICO Luigi Melchiorre for the great times we shared in the lab, all the discussions, and his constant love and care. Grazie per tutti i caffè macchiato e cornetti che abbiamo scroccato durante gli eventi al poliba. Spero teniate per voi i miei segreti e tutto ciò che ho detto durante i coffee breaks...

I would like to acknowledge my colleagues from MTU for their wonderful collaboration. I would particularly like to thank Dr. Artem Vorobev for his help with device fabrication at the Tyndall cleanroom, thank you as well for your valuable comments during the review of our publications, Dr. Chinna Devarapu for helping me gain many skills and for our fruitful discussions, and Gautham Vijayan for his theoretical support and guidance. I am also thankful to each of my MTU colleagues for their advice and kindness.

I would like to thank my coffee friends for the wonderful times we shared at POLIBA, particularly Dr. Udith Krishnan from STIIMA, CNR; Rahul Das Kutteeri from POLIBA; Dr. Enes Tabak from DICATECH; Dr. Danish Ali Bhutto; and Dr. Sana Ullah, my colleague from the lab. Many thanks to all of them, for the beautiful time we spent together. I deeply acknowledge the meaningful conversations and hangouts we had in Bari.

I would like to express my sincere gratitude to my friends from CUSAT, Asapana Rajesh from Université de Lille and CNRS, my friends from my hometown, Saleeq Ahammed, and my family for their constant support and prayers.

Finally, I would like to acknowledge my wife, Ubitha, for her patience, care, trust, and, above all, for her understanding and tolerance throughout this journey. Love you.

# Abstract

This thesis introduces advanced nanophotonic integrated devices aimed at improving miniaturized, cost-effective multi-gas detection and on-chip spectroscopic systems. Traditional spectroscopic techniques often require bulky optical components and multiple detectors, limiting their scalability for multi-gas sensing. The proposed integrated duplexers and triplexers enable switching between lasers to detect multiple gases using a single system. The work focuses on the design and optimization of broadband angled multimode interference duplexers, directional coupler-based duplexers, and cascaded directional coupler-based triplexers for combining spectroscopically relevant wavelengths in the near-infrared region. The target gases include ammonia, methane, and carbon dioxide. Through comprehensive simulations and experimental investigations, the proposed on-chip designs demonstrate superior performance compared to existing solutions and have a unique advantage in terms of smaller footprint and improved coupling efficiency. DC-based duplexer has been successfully integrated with laser and GRIN lens components, resulting in a ready-to-use module for multi-gas sensing applications.

A semi-integrated photonic sensing system is presented, exploiting on-chip waveguides with Quartz Enhanced Photoacoustic spectroscopy and Light induced thermoelastic spectroscopy (LITES). Side-polished optical fibers are explored to enhance light-matter interaction path when detecting water vapor and methane gases using LITES method. To further improve integration of integrated nanophotonic devices with spectroscopic devices and to enhance light-matter interaction, a novel wave confinement approach is introduced using high-contrast grating hollow core waveguides. These waveguides feature a reflective surface that maintains high transmission while allowing gas flow through the sidewalls, making them particularly suitable for gas spectroscopic applications. They are specifically optimized for methane sensing at a wavelength of  $3.27\ \mu\text{m}$ . The final goal of this thesis is to develop a complete system that integrates a multiplexer with integrated lasers and high-efficiency interaction pathways, such as hollow core waveguides, into a spectroscopic device. This compact and integration-friendly design holds great promises for enabling the development of portable, high-precision, and real-time multi-gas sensing devices for applications from industrial, agricultural to environmental monitoring.

# List of Publications

## Journal Papers

1. **Ajmal Thottoli**, Gabriele Biagi, Artem S Vorobev, Marilena Giglio, Giovanni Magno, Liam O’Faolain, Marco Grande, *Highly efficient and selective integrated directional couplers for multigas sensing applications*, Scientific Reports, 13, 22720 (2023). <https://doi.org/10.1038/s41598-023-49889-2>.
2. Muhammad Musavir Bilal, Servando Lopez-Aguayo, and **Ajmal Thottoli**, *Numerical Analysis of Solid-Core Photonic Crystal Fiber Based on Plasmonic Materials for Analyte Refractive Index Sensing*, Photonics, 10, 1070 (2023). <https://doi.org/10.3390/photonics10101070>.
3. **Ajmal Thottoli**, Artem S Vorobev, Gabriele Biagi, Simone Iadanza, Marilena Giglio, Giovanni Magno, Marco Grande, Liam O’Faolain, *Compact angled multimode interference duplexers for multi-gas sensing applications*, Opt. Express, 32, 3451–3460 (2024). <https://doi.org/10.1364/OE.503483>.
4. **Ajmal Thottoli**, Gabriele Biagi, Artem S Vorobev, Antonella D’Orazio, Giovanni Magno, Liam O’Faolain, *Cascaded Directional Coupler-Based Triplexer Working on Spectroscopically Relevant Wavelengths for Multiple Gas Detection*, Photonics, 12, no. 3: 192 (2025). <https://doi.org/10.3390/photonics12030192>.
5. Luigi Melchiorre, **Ajmal Thottoli**, Artem S. Vorobev, Giansergio Menduni, Angelo Sampaolo, Giovanni Magno, Liam O’Faolain, Vincenzo Spagnolo, *Study and Characterization of Silicon Nitride Optical Waveguide Coupling with Quartz Tuning Fork Toward Integrated Sensing Platforms*, Sensors, 25, 3663 (2025). <https://doi.org/10.3390/s25123663>.
6. Muhammad Musavir Bilal, **Ajmal Thottoli**, Marco Grande, and Servando Lopez-Aguayo, *Numerical and Experimental Analysis of Side Polished Single-Mode Fiber for Refractive Index Sensing*, accepted in Frontiers in Photonics (2025). <https://doi.org/10.3389/aot.2025.1560454>.

## Conference Proceedings

1. **Ajmal Thottoli**, Artem S Vorobev, Gabriele Biagi, Simone Ladanza, Giovanni Magno, Liam O'Faolain, Marco Grande, *Design and Fabrication of Angled MMI-Based Duplexer for Sensing Applications*, Conference on Lasers and Electro-Optics Europe & European Quantum Electronics Conference (CLEO/Europe-EQEC) (2023). DOI: [10.1109/CLEO/Europe-EQEC57999.2023.10232273](https://doi.org/10.1109/CLEO/Europe-EQEC57999.2023.10232273).
2. **Ajmal Thottoli**, Artem S Vorobev, Gabriele Biagi, Simone Ladanza, Giovanni Magno, Liam O'Faolain, Marco Grande, *Design and Optimization of Broadband Optical Duplexer and Triplexer Couplers*, 23rd International Conference on Transparent Optical Networks (ICTON) (2023). DOI: [10.1109/ICTON59386.2023.10207445](https://doi.org/10.1109/ICTON59386.2023.10207445).
3. **Ajmal Thottoli**, Ganga Chinna Rao Devarapu, Antonella D'Orazio, Giovanni Magno, Liam O'Faolain, *Novel High Contrast Grating Hollow Core Waveguides for Enhanced Gas Spectroscopy*, EPJ Web of Conferences (2024). DOI: [10.1051/epjconf/202430901009](https://doi.org/10.1051/epjconf/202430901009).

This work is dedicated to my beloved  
Professor Marco Grande. He was  
deeply committed to education and  
cared deeply for his students.  
His dedication and kindness will  
always be remembered.

# Contents

<b>Acknowledgements .....</b>	<b>v</b>
<b>Abstract .....</b>	<b>vii</b>
<b>List of Publications .....</b>	<b>viii</b>
<b>Contents .....</b>	<b>xi</b>
<b>Introduction .....</b>	<b>1</b>
<b>Chapter 1- Methodological Framework .....</b>	<b>9</b>
1.1 Numerical Methods in Electromagnetics .....	10
1.1.1 Beam Propagation Method .....	10
1.1.2 Rigorous Coupled Wave Analysis .....	12
1.2 PIC Fabrication Method .....	14
1.3 Free-Space Optical Characterization .....	16
1.3 Laser Modulation and Detection Techniques .....	17
1.3.1 QTF Electrical Characterization .....	18
<b>Chapter 2- Advanced PICs for Multi-Gas Sensing .....</b>	<b>21</b>
2.1 Introduction .....	21
2.2 Design Strategies for Input Waveguide.....	22
2.3 Compact Angled Multimode Interference Duplexers .....	26
2.3.1 Theoretical Principles of MMI and Angled MMI .....	27
2.3.2 Proposed Structure and Numerical Result.....	29
2.3.3 Optical Characterization and Experimental Results .....	34
2.4 Highly Efficient and Selective DC Duplexer .....	38
2.4.1 Evanescent Field Coupling.....	39
2.4.2 Proposed Structure and Numerical Results .....	41
2.4.3 Optical Characterization and Experimental Results .....	45

2.5 Cascaded DC-based Triplexer .....	49
2.5.1 Proposed Structure and Numerical Results .....	49
2.5.2 Optical Characterization and Experimental Results .....	51
<b>Chapter 3 - Integrated Sensing Architecture .....</b>	<b>57</b>
3.1 SPF Integrated Sensing System.....	57
3.1.1 Refractive Index Sensing .....	58
3.1.2 Water Vapor Detection through LITES.....	62
3.1.3 Methane Detection through LITES.....	64
3.2 TLF Integrated Sensing System .....	66
3.2.1 TLF Coupled LITES Measurements.....	67
3.2.2 TLF Coupled QEPAS Measurements.....	69
3.3 PIC Enabled Semi-Integrated Sensing Architecture .....	72
3.3.1 Si <sub>3</sub> N <sub>4</sub> Chip Coupling with QTF for QEPAS Applications .....	73
3.3.2 Si <sub>3</sub> N <sub>4</sub> Chip Coupling with QTF for LITES Applications .....	75
<b>Chapter 4 - High Contrast Grating Hollow Core Waveguide .....</b>	<b>78</b>
4.1 Introduction to PIC based Hollow core waveguide.....	78
4.1.1 Theory and background .....	80
4.2 HCG mechanism for Ultra-High Reflectivity .....	82
4.3 Design Principle of HCG-HCW.....	84
4.4 Light Guiding in HCG-HCW Coupler.....	87
<b>Chapter 5 - Future Work and Conclusion .....</b>	<b>90</b>
5.1 Laser Integration a proof of principle .....	90
5.1.2 Expected sensitivity of duplexer device .....	91
5.2 Characterization Techniques for HCW.....	92
5.3 Design of a Metasurface Based FP Cavity .....	93
5.4 Conclusion .....	97
<b>Reference .....</b>	<b>100</b>

# Introduction

## Introduction to Photonic Integrated Circuits

Photonic integrated circuits (PICs) are compact optical devices that combine lasers, modulators, detectors, and waveguides into a single chip. They find applications in several fields, including biomedical imaging, optical communication, and sensing. This thesis focuses on both theoretical and experimental solutions using PICs for enhancing gas spectroscopy. The demand for compact, efficient, and highly sensitive gas spectroscopy systems has driven research toward advanced photonic integrated devices with improved functionalities. The introduction section provides an overview of photonic integrated circuits (PICs), discussing their advantages and recent advancements in the field. It examines existing gas sensing technologies, highlighting their limitations and drawbacks, which form the foundation for this research. Additionally, the Introduction outlines the scope of the thesis, detailing its objectives and contributions, and explains the organization of each chapter.

Recent progress in PICs is the result of mature microfabrication methods such as complementary metal-oxide-semiconductor (CMOS) technology, advances in semiconductor lasers, improved understanding of optical devices, and the precision of simulation and design tools. The integration of lasers and complex optical operations onto a single solid microchip presents a significant commercial opportunity, offering cost-effective, ultra-fast, and compact alternatives to traditional systems. Silicon (Si) has emerged as a dominant choice due to its large-scale production and natural abundance. The platform offers a substantial refractive index contrast, enabling efficient optical confinement within compact device footprints. Silicon-on-insulator (SOI) platforms are explored for applications involving waveguiding and show great potential for subwavelength structures. This suitability arises from the minimum feature size achievable during fabrication, which enables the precise and efficient development of complex photonic structures.

Among silicon-based platforms, silicon nitride ( $\text{Si}_3\text{N}_4$ ) has gained significant attention due to its unique material properties. In this thesis,  $\text{Si}_3\text{N}_4$  stands out due to its high-volume production capability and low propagation losses (potentially 1.4 dB/m), wide transparency window (0.25–3.5  $\mu\text{m}$ ), which is achieved through precise control of material deposition ratios, low thermo-optic coefficient ( $\sim 10^{-5}/^\circ\text{C}$ ), nonlinear coefficient ( $2.1 \times 10^{-18} \text{ m}^2 \text{ W}^{-1}$ ), high power handling capability ( $>100\text{W}$ ), and potential for 3D integration [1], [2], [3]. Moreover, when comparing bend and propagation losses among various materials, such as silicon (Si) and indium

phosphide (InP), Si<sub>3</sub>N<sub>4</sub> offers significant advantages [4]. These features make Si<sub>3</sub>N<sub>4</sub> devices highly attractive for enabling miniaturized systems with high performance and scalability.

## Gas Spectroscopy Systems

Recent progress in semiconductor lasers has enabled a broad range of applications in gas sensing and spectroscopy, enabling the miniaturization of optical gas sensors by integrating laser sources on-chip. Optical gas sensors are used to detect greenhouse gases and air pollutants by measuring the unique absorption spectra of the target molecules usually located in the mid-IR range. The near-infrared (NIR) wavelength range is also suitable for the detection and quantification of key gas molecules, which can be effectively analyzed using various spectroscopic techniques [5], [6], [7]. Various gas analyzers are commercially available, utilizing spectroscopic techniques such as photothermal, photoacoustic, tunable diode laser absorption spectroscopy (TDLAS), cavity ringdown, thermal FTIR, and comb spectroscopy [8], [9], [10]. TDLAS is a cost-effective and real-time gas detection method but is limited by its requirement for long path lengths which causes precision and stability issues. Photoacoustic-based gas absorption techniques, such as Quartz Enhanced Photoacoustic Spectroscopy (QEPAS), unlock real-time in-situ measurements with response time shorter than  $< 1$  s and offer high gas specificity. They are capable of part-per-quadrillion (ppq) detection sensitivity [8,9]. This technique utilizes a mid-IR source and a Quartz Tuning Fork (QTF) as a transducer, known for its stability and precision, and is independent of wavelength. QTFs are well known for enabling precise oscillation in clocks and watches. The QTF responses are wavelength-independent, enabling the detection of a broad range of gases using lasers emitting across the spectrum, from ultraviolet (UV) to terahertz (THz). The near-infrared (NIR) wavelength band is also suitable for detecting and quantifying key gases, as it provides strong absorption features associated with molecular vibrational transitions. A QTF consists of two cantilever bars (prongs) connected at a shared base. The fundamental mode of vibration occurs at a frequency in the range of 8-32 kHz. The mechanical vibration/stress leads to a displacement of internal charge carriers within the crystal structure of quartz. This stress distorts the atomic lattice, displacing positive and negative charges and creating polarization. This polarization generates an electric potential (voltage) across the surface of the material, which is the piezo electric conversion. If electrodes are placed on the material, this potential drives a weak electric current when the circuit is closed.

A key feature of QEPAS involves a laser beam modulated at half the resonance frequency of the QTF, which is directed and focused between the prongs of the QTF, as shown in Figure 1.

When a molecule absorbs energy from light at the absorption wavelength specific to the gas molecules, it transitions to an excited energy state. As the molecule relaxes back to its ground state through non-radiative processes, it causes localized heating, which results in local pressure changes. This periodic localized effect leads to the generation of photoacoustic waves, with the same frequency as the modulated source. The high-Quality Factor (Q-Factor) of the QTF efficiently transforms acoustic waves, produced by the non-radiative relaxation of the target gas upon absorbing radiation, into an electric signal through the piezoelectric properties of quartz.

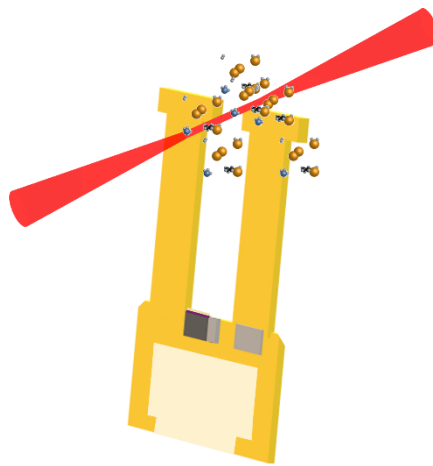


Figure 1 : QEPAS laser- to-QTF configuration.

These signals are weak and must be amplified by a transimpedance amplifier. The strength of these photoacoustic signals is expressed as

$$\text{Photoacoustic Signal} \propto P \cdot \alpha \cdot (Q\text{-Factor}) \cdot \varepsilon$$

Here,  $P$  represents the incident optical power,  $\alpha$  the absorption coefficient of gases and  $\varepsilon$  the conversion efficiency of optical power to sound directly associated with gas concentration. Notably, the QEPAS technique can detect a dynamic range of concentrations ranging from parts-per-trillion (ppt) levels up to a few percent concentration levels. This approach eliminates the need for an optical detector and gas cell, as the QTF itself serves as the detector. In QEPAS systems, the only way to induce QTF vibration is via the photoacoustic effect, which generates sound waves using an acoustic source positioned between the two QTF prongs, thereby exciting a piezo-electric active mode.

Another recently introduced advanced sensing technique, developed by Ma et al. in 2018 is Light-induced thermoelastic spectroscopy (LITES). LITES employs QTFs as photodetectors for gas sensing, exploiting a typical Tunable Diode Laser Absorption Spectroscopy (TDLAS) configuration [11], [12], [13], [14]. The basic idea behind this novel approach is that the light energy is absorbed by the gas molecules before the light reaches the QTF. The prong base of a

custom QTF consists of three layers: a 250 Å gold layer, a 50 Å chromium layer, and a 250 μm thick quartz layer. The QTF features a gold layer on the back side that helps with back reflection and laser beam diffusion, while the front surface of this area is left uncoated, permitting laser transmission and enhanced absorption through the quartz. When the modulated light beam at the characteristic absorption wavelength passes through the chamber, its energy is absorbed by the gas molecules and subsequently released, causing localized heating at the surface of the QTF. It is important to direct the laser beam toward the base of the QTF, where it induces high strain, as shown in Figure. 2. This interaction generates photothermal heating as the quartz absorbs the light, resulting in thermo-elastic conversion. As a result, the QTF prongs undergo elastic deformation and vibrate. These mechanical vibrations are transformed into a piezoelectric signal.

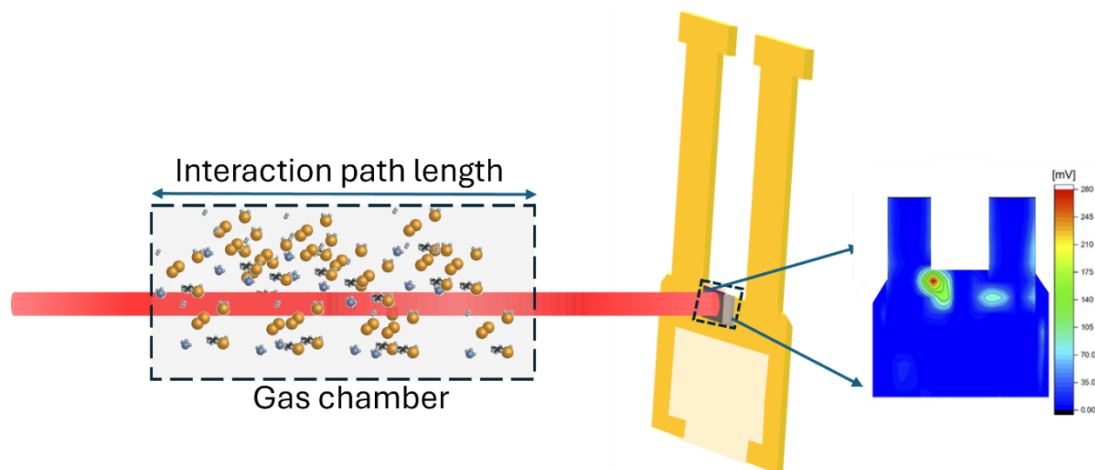


Figure 2: LITES Configuration, showing the integrated path length before the light reaches the QTF. The zoomed-in view highlights the material distribution layers and the precise position where the laser is focused to induce strain.

This feature sets LITES apart from the QEPAS technique by avoiding the need to put QTF in the sensing environment, making it suitable for non-contact and distanced gas detection.

### Scope of the Thesis

To accurately assess the level of pollution in the surrounding air, measurements must be taken at every location. This necessitates the use of air quality sensors that are low-cost, compact, easily deployable in large numbers, suitable for automation-friendly mass production, and capable of detecting multiple harmful gases in real time. Over the years, many QEPAS and LITES studies have targeted different chemical species across a broad range of spectroscopically relevant wavelengths. Through these efforts, sensitivities ranging from a few parts per trillion to parts per million by volume have been achieved, making QEPAS and LITES an excellent choice for applications requiring high sensitivity and small-volume detection. Despite these

advantages, QEPAS and LITES still face significant challenges, including trade-offs among size, weight, sensitivity, selectivity, sensor lifetime, calibration requirements, and performance in harsh environments. Traditional configurations often rely on bulky free-space optical setups with lasers and collimating lenses, which are prone to misalignment over time, thereby reducing device lifespan. Portability remains a key challenge, especially for wide area sensing in agricultural or remote environments. Addressing these issues through lightweight, compact, and cost-effective designs is crucial, particularly for applications such as unmanned-aerial-vehicle-based environmental monitoring.

Another limitation of these devices is that they are designed for single-gas detection, as each analyte requires a dedicated source and detector. These challenges stem from the absence of highly efficient optical multiplexers and from the difficulty of selecting materials capable of covering a broad spectral range while matching the absorption features of each gas molecule. By addressing these technological barriers, this research seeks solutions aligned with the objectives of the European project H2020-ICT-37-2020 “Photonic Accurate and Portable Sensor Systems Exploiting Photo-Acoustic and Photo-Thermal Based Spectroscopy for Real Time Outdoor Air Pollution Monitoring- PASSEPARTOUT” no. 101016956, (<https://www.passepartout-h2020.eu/>). The PASSEPARTOUT project aims to develop portable, cost-effective smart sensors for real-time gas detection for environmental pollution monitoring, bridging the gap between low-cost, low-performance sensors and highly sensitive but bulky equipment. This research contributes to PASSEPARTOUT by exploring and implementing ultra-wideband couplers for spectrally “distant” wavelengths (~600 nm range) for multi-gas sensing applications. The PIC devices were fabricated in collaboration with the Tyndall National Institute in Ireland. Si<sub>3</sub>N<sub>4</sub>-based duplexers or triplexers, which can combine two or three spectroscopically relevant wavelengths, offer portable and compact solutions for multi-gas sensing applications. They enable the detection of key gases such as ammonia (NH<sub>3</sub>), methane (CH<sub>4</sub>), and carbon dioxide (CO<sub>2</sub>), with absorption lines at 1530 nm, 1654 nm, and 2003 nm, respectively. By rapidly switching optical sources, the duplexer or triplexer can facilitate the detection of multiple gases with high temporal resolution. Techniques that can benefit from this duplexer/triplexer include TDLAS, QEPAS, LITES, and various other spectroscopic methods. This thesis specifically focuses on their advantages for multigas detection using QEPAS.

A significant challenge in QEPAS and LITES is the lack of compact and robust integrated devices, and the need for efficient light-matter interaction mechanisms. On the one hand, advancements in near-IR distributed feedback (DFB) butterfly-packaged fiber-coupled laser diodes, tuned to the absorption wavelengths of gas molecules, have significantly improved gas

sensing and spectroscopy. One promising approach to achieving a compact, cost-effective, and highly robust integrated solution for enhancing QEPAS and LITES techniques employs tapered lensed fibers (TLF) and side polished fibers (SPF). A TLF serves as an efficient light-focusing mechanism, enabling evanescent field sensing in QEPAS and providing an interaction path for small-volume detection in LITES. The system has been demonstrated with water vapor molecules, exhibiting an absorption wavelength of 1395 nm, achieving high sensitivity and stability. They serve as an effective interaction pathway, enabling long-distance sensing and facilitating straightforward integration into various systems. The designs proposed later in this thesis exploit SPF technology, which is specifically tailored for detecting methane and water vapor. Methane exhibits a strong absorption peak at 1654 nm, while water vapor absorbs prominently at 1395 nm. Several steps toward the full integration of the QTF-based sensing system with PICs have been evaluated, particularly the photonic-chips/QTF interface. The focus has been on simplifying the integration of laser sources and sensors, paving the way for more efficient and compact gas sensing solutions.

A promising solution for enhancing integration possibilities and enabling low-cost automated assembly, without relying on lenses or fibers, is the use of integrated chip-scale Hollow-Core Waveguides (HCWs). An HCW allows light to travel through air, which serves as the waveguide core and is surrounded by highly reflecting surfaces. Integrated chip-scale systems based on silicon V grooves coated with metals, distributed Bragg reflectors and anti-resonant reflection layers have been reported but suffer from high optical losses due to poor reflection, the challenges of multi-layer fabrication and the complexities of integration with the QTF. This thesis introduces a straightforward, effective design concept for a novel ultra-low-loss single-mode subwavelength high-contrast grating (HCG) HCW. The key innovation is that gases or fluids can flow directly into the waveguide through side openings, greatly improving real-time gas interaction. An HCW guides optical beams through the air via multiple reflections at cladding mirrors, achieved through constructive interference of grating harmonics in a sub-wavelength periodic structure. The proposed design uses silicon (Si) on a silicon dioxide (SiO<sub>2</sub>) platform, which provides high index contrast. The Si-based grating system offers significant advantages, such as a simpler and single-etching fabrication process, which reduces complexity and manufacturing costs. The designs proposed in this study are specifically tailored for detecting methane, which exhibits a strong absorption peak at 3270 nm. Numerical simulations demonstrate the optical performance of HCWs and show how light can be efficiently guided through various coupler configurations using these sidewall-less waveguides.

The integration of laser-based multiplexers and compact coupling with the QTF is outlined as future work in this thesis. A complete sensing device incorporating integrated laser sources at 1530 nm and 1653.7 nm for methane detection has been developed and is ready for use. Further research will examine the characterization of the fabricated metasurfaces and the alignment methodologies required for optimization. One proposed alignment technique involves using an HCG-based metasurface with high-finesse Fabry-Perot (FP) cavity to enhance gas-sensing performance. FP structures will also be investigated for their potential to improve QEPAS signal enhancement in real-world applications.

This thesis is organized with the ultimate goal of developing a complete system that integrates a multiplexer, integrated lasers, and high-efficiency interaction pathways, such as HCG HCWs, into a spectroscopic device. It is organized as follows:

**Chapter 1:** This chapter elaborates on numerical simulation methods, such as Beam Propagation Method (BPM) and the Rigorous Coupled-Wave Analysis (RCWA), used for the design of PICs. It then outlines a step-by-step procedure for various fabrication techniques and provides an overview of QTF electrical characterization followed by QEPAS and LITES detection schemes.

**Chapter 2:** Recent advances in multiplexers are reviewed, and basic theory of angled Multimode Interference couplers (MMI) and Directional couplers (DCs) are briefly presented. It includes the designs of angled MMI and DC as duplexers, with both numerical and experimental results. Additionally, the design and experimental outcomes of a triplexer utilizing a DC are presented.

**Chapter 3:** This chapter introduces SPF as a refractive index sensor utilizing evanescent field interaction is presented, followed by its application in detecting water vapor and methane using LITES. This chapter also covers the integration of TLF for QEPAS and demonstrates the proof of concept of semi-integrated PIC chips with a QTF for both QEPAS and LITES methodologies.

**Chapter 4:** Chapter 4 presents HCG-HCWs, which simultaneously guide light and enable enhanced light-matter interaction and integration capabilities, focusing on their application to LITES gas-sensing techniques. This chapter includes the theory and design of various HCWs optimized for operation at 1550 nm and 3270 nm, targeted for ammonia and methane detection, respectively.

**Chapter 5:** This chapter presents the future work and the conclusion of this thesis. It covers the development of ready-to-use laser-integrated duplexer chips and their testing with QEPAS.

The characterization and alignment setup for HCW is demonstrated. Preliminary characterization results validate RCWA results with FTIR, and the design concept of a high-finesse FP cavity is presented.

# Chapter 1- Methodological Framework

In this chapter, the methodologies employed for the design, fabrication, and characterization of the optical devices developed in this work are explained. The numerical simulation methods include the Beam Propagation Method (BPM) and Rigorous Coupled-Wave Analysis (RCWA). BPM is used to perform coupled-mode analysis for duplexer and triplexer design, evaluate commercial laser output modes, calculate the effective modes of side-polished fibers, and design of HCG-HCW. RCWA is used to design high-contrast subwavelength gratings on the silicon-on-insulator platform. A key step in PIC fabrication is lithography, a process that defines complex patterns on substrates with nanoscale precision. This thesis makes use of two widely used techniques: electron-beam lithography (EBL) and stepper lithography, each offering distinct advantages. Precise patterning is critical, with EBL being utilized for the fabrication of  $\text{Si}_3\text{N}_4$  based duplexers and triplexers, and photolithography for high-contrast silicon-based grating elements. EBL is highly effective for creating precise nanostructures, achieving exceptionally small feature sizes. For example, EBL is utilized to fabricate  $\text{Si}_3\text{N}_4$  structures with a resolution of  $0.25 \mu\text{m}$ , leveraging its smaller exposure area. Conversely, stepper is used for silicon HCG with a feature size of  $0.6 \mu\text{m}$ . This technique is ideal for large-area exposures, offering benefits such as single etching, faster processing times, and cost-efficient fabrication. Together, these lithography methods form the foundation of PIC manufacturing, enabling the integration of optical components such as waveguides, gratings, and resonators onto a single chip.

Additionally, the characterization of duplexers, triplexers, spirals, rings, and Fabry-Perot devices is performed using the end-fire method, which is configured differently for each application. The specific configurations are explained alongside the results in their respective sections. The end-fire method involves launching light into the input of the sample devices and collecting it from the output using free-space optics. Moreover, the QEPAS and LITES detection configurations, as well as the electrical characterization of the QTF for determining resonance frequency and Q-Factor, are detailed.

## 1.1 Numerical Methods in Electromagnetics

### 1.1.1 Beam Propagation Method

The Beam Propagation Method (BPM) is widely utilized in computational dynamics for designing photonic integrated circuits, such as multimode interference couplers, bent waveguides, DCs, and fiber optics [15], [16]. The BPM utilizes an approximation technique to simulate slowly varying optical waveguides. It is based on the assumption that the envelope of a forward-traveling wave pulse changes gradually in time and space compared to its period or wavelength. When a wave propagates along a waveguide over a long distance, much greater than the wavelength, rigorous numerical simulations become computationally expensive. BPM addresses this challenge by employing approximate differential equations, whose solutions are focused on the spatial propagation direction, rather than evolution over time. The basic approach is the formulation of the problem in terms of the scalar field (i.e. neglecting polarization effects) and paraxiality (i.e. propagation restricted to a narrow range of angles) approximations [17]. Initially, BPM requires two key pieces of information: the refractive index distribution,  $n(x, y, z)$ , and the input wave field,  $u(x, y, z=0)$ . Additionally, a specific spatial domain must be defined with the transverse grid sizes,  $\Delta x$  and  $\Delta y$ , and longitudinal step size,  $\Delta z$ .

The theoretical foundation of BPM originates from the wave equation, the well-known Helmholtz equation in a three-dimensional space:

$$\frac{\partial^2 E}{\partial x^2} + \frac{\partial^2 E}{\partial y^2} + \frac{\partial^2 E}{\partial z^2} + k^2(x, y, z)E = 0 \quad (1.1)$$

where  $k$  is the spatial dependent wavenumber, i.e.  $k(x, y, z) = k_0 n(x, y, z)$ , with  $k_0$  being the free space wavenumber. Here the scalar slowly varying electric field is given by

$$E(x, y, z) = u(x, y, z)e^{-j\beta z} \quad (1.2)$$

where  $\beta$  is the propagation constant representing the average phase variation of the field  $E$ . In typical guided-wave problems, the most rapid variation in the field  $u$  arises from the phase variation due to propagation along the guiding axis. Assuming that this axis is predominant along the  $z$ -direction, it is beneficial to factor out this rapid variation by introducing a so-called slowly varying field. By substituting the expression in (1.1) of the rapidly varying phase into the Helmholtz equation, the following equation is derived for governing the behaviour of the slowly varying field:

$$-\frac{\partial^2 u}{\partial z^2} + 2j\beta \frac{\partial u}{\partial z} = \frac{\partial^2 u}{\partial x^2} + \frac{\partial^2 u}{\partial y^2} + (k^2 - \beta^2)u \quad (1.3)$$

At this point, the above equation is completely equivalent to the exact Helmholtz equation, except that it is expressed in terms of  $u$ .

$$\left| \frac{\partial^2 u}{\partial z^2} \right| \ll \left| 2\beta \frac{\partial u}{\partial z} \right| \quad (1.4)$$

It is now assumed that the variation of  $u$  with  $z$  is sufficiently slow, allowing us to neglect the Equation (1.4). This assumption is known as the Slowly Varying Envelope Approximation (SVEA) and is also referred to as paraxial or parabolic approximations. With this assumption, and after slight rearrangement, the equation derived earlier simplifies under SVEA to become the fundamental Beam Propagation Method (BPM) equation in three dimensions (3D):

$$2j\beta \frac{\partial u}{\partial z} = \frac{\partial^2 u}{\partial x^2} + \frac{\partial^2 u}{\partial y^2} + (k^2 - \beta^2)u \quad (1.5)$$

Several numerical methods are used to solve the basic BPM equations, the Fast Fourier Transform Beam Propagation Method (FFT-BPM), and the Finite-Difference Beam Propagation Method (FD-BPM) are the most prominent. FD-BPM is generally preferred over FFT-BPM due to its simplicity, higher accuracy, and improved efficiency. The Crank-Nicolson scheme is further utilized to solve any stability issues in the equations [18], [19]. In FD-BPM, the optical field is represented along the propagation direction  $z$  (longitudinal direction) at discrete points in the transverse plane ( $x, y$ ). The field at the next  $z$ -plane is derived from the field at the previous  $z$ -plane. For the 2D case, the finite-difference discretization equation can be expressed as follows, and this process is then repeated iteratively to compute the field throughout the entire structure.

$$j \frac{u_i^{n+1} - u_i^n}{\Delta z} = \frac{1}{2\beta} \frac{u_{i+1}^n - 2u_i^n + u_{i-1}^n}{\Delta x^2} + \frac{1}{2\beta} (k_i^2 - \beta^2) \quad (1.6)$$

In this formulation,  $u_i^n$  represents the field at the  $i$ -th transverse grid point and the  $n$ -th longitudinal plane, while  $\Delta x$  and  $\Delta z$  denote the grid sizes in the transverse and longitudinal directions, respectively.

The inherent limitations of the basic BPM approach, such as restrictions on angular propagation and one-way assumptions, have been addressed through advanced implementations. These include wide-angle BPM algorithms, which enable simulations of larger angular ranges, and bi-directional BPM algorithms, which account for wave propagation in both forward and backward directions. The BPM was initially based on the Fourier Transform algorithm. Later, it was extended to finite-difference-based BPM schemes (FD-BPM) and finite-element BPM (FE-BPM), and many others. FE-BPM methods extend its capabilities by supporting wide-angle propagation, full-vectorial analysis, back-propagation and reflection evaluations, polarization effects, and the incorporation of transparent boundary conditions. Additionally, BPM can model anisotropic and nonlinear materials, enhancing its functionality. As the BPM is an approximation method of the guided wave equation and doesn't account for scattering and

back-propagating light, makes BPM computationally faster as compared to other methods like Finite-Difference Time-Domain (FDTD) methods, without compromising the accuracy of results.

In this work, simulations were conducted using a commercial BPM package from RSoft, called BeamPROP, which offers robust tools for advanced analyses, used for parameterizing and estimating the optimum results using FD-BPM [15], [19]. Transparent boundary conditions (TBC) are placed appropriately, which completes the system of equations since the poor choice of boundary condition can lead to artificial reflection of incident light reversing into the computational domain. The semi-vector approach is used for high accuracy and rapid computation. Also, the popular and most accurate Pade approximation method is used for wide-angle BPM to reduce paraxial limitations [16]. For angles lower than 10 degrees, the Pade order (0,1) is used. In most cases, BeamPROP has optimum results while the effort is considered on choosing the appropriate grid size in the numerical simulation region from the convergence test performance.

### 1.1.2 Rigorous Coupled Wave Analysis

The Rigorous Coupled Wave Analysis (RCWA) is a well-established technique based on the full vectorial solution of Maxwell's equations, which was first introduced in the mid-1980s [20], [21]. RCWA is also known as the Fourier Modal Method, Transfer Matrix Method with a plane wave basis. It is primarily applied to solve the scattering problems of periodic structures[22]. In the RCWA method, Maxwell's equations are solved in the Fourier domain, where fields are represented as a sum of coupled waves, and the periodic dielectric function of the structure is expressed as Fourier harmonics[23]. By factoring out an assumed time harmonic factor  $\exp[-i\omega t]$ , Maxwell's equations can be expressed in the frequency domain in 1D as:

$$\begin{aligned}
 \frac{\partial H_z}{\partial y} - \frac{\partial H_y}{\partial z} &= j\omega\epsilon_0\epsilon_{r,x}E_x \\
 \frac{\partial H_z}{\partial x} - \frac{\partial H_x}{\partial z} &= j\omega\epsilon_0\epsilon_{r,y}E_y \\
 \frac{\partial H_y}{\partial x} - \frac{\partial H_x}{\partial y} &= j\omega\epsilon_0\epsilon_{r,z}E_z \\
 \frac{\partial E_z}{\partial y} - \frac{\partial E_y}{\partial z} &= -j\omega\mu_0H_x \\
 \frac{\partial E_z}{\partial x} - \frac{\partial E_x}{\partial z} &= j\omega\mu_0H_y \\
 \frac{\partial E_y}{\partial x} - \frac{\partial E_x}{\partial y} &= -j\omega\mu_0H_z
 \end{aligned} \tag{1.7}$$

The above equations can be expressed in terms of the transverse fields by eliminating the dependencies on  $E_z$  and  $H_z$ . The medium is characterized by a diagonal index tensor concerning principal axes with diagonal elements  $\varepsilon_{r,x}$ . The resulting equations are written as.

$$\begin{aligned}\frac{\partial E_x}{\partial z} &= \left( \frac{-j}{\omega \varepsilon_0} \frac{\partial}{\partial x} \frac{1}{\varepsilon_{r,z}} \frac{\partial}{\partial y} \right) H_x + \left( \frac{-j}{\omega \varepsilon_0} \frac{\partial}{\partial x} \frac{1}{\varepsilon_{r,z}} \frac{\partial}{\partial y} + j\omega \mu_0 \right) H_y \\ \frac{\partial E_y}{\partial z} &= \left( \frac{-j}{\omega \varepsilon_0} \frac{\partial}{\partial x} \frac{1}{\varepsilon_{r,z}} \frac{\partial}{\partial y} - j\omega \mu_0 \right) H_x + \left( \frac{-j}{\omega \varepsilon_0} \frac{\partial}{\partial x} \frac{1}{\varepsilon_{r,z}} \frac{\partial}{\partial y} \right) H_y \\ \frac{\partial H_x}{\partial z} &= \left( \frac{j}{\omega \mu_0} \frac{\partial}{\partial x} \frac{\partial}{\partial y} \right) E_x + \left( \frac{-j}{\omega \mu_0} \frac{\partial}{\partial x} \frac{\partial}{\partial x} - j\omega \varepsilon_0 \varepsilon_{r,y} \right) E_y \\ \frac{\partial H_y}{\partial z} &= \left( \frac{j}{\omega \mu_0} \frac{\partial}{\partial x} \frac{\partial}{\partial y} + j\omega \varepsilon_0 \varepsilon_{r,x} \right) E_x + \left( \frac{-j}{\omega \mu_0} \frac{\partial}{\partial x} \frac{\partial}{\partial x} \right) E_y\end{aligned}\quad (1.8)$$

For scattering problems, the goal is to determine the reflected and transmitted light waves arising from the incident field. Solving Equation (1.8) directly in the spatial domain with appropriate boundary conditions is computationally intensive. Bloch's theorem is applied to expand both the above equations and the boundary conditions. To ensure accuracy and computational efficiency, the higher-order terms are eliminated, reducing the infinitely large number of terms. To solve period grating structure, the equations must be decomposed into simple building blocks, each consisting of a vertically homogeneous region, i.e. a region with values of  $\varepsilon_{r,x}$  which are independent of  $z$ . After applying Bloch's Theorem, the equation can be written for  $E_x$  as,

$$E_x = e^{j(k_{x,0}x + k_{y,0}y)} \sum_p \sum_q e^{j\left(\frac{2\pi}{\Lambda_x}px + \frac{2\pi}{\Lambda_y}qy\right)} \sum_m a_{x,m,p,q} (f_m e^{jk_m z} + g_m e^{-jk_m z}) \quad (1.9)$$

Using the above formulations, the equation is reduced to an eigenvalue problem of the form:

$$Ax = \lambda x \quad (1.10)$$

Operator  $A$  arises from the discretization and matrix formulation of these differential Equations (1.8). Specifically, “ $A$ ” encapsulates the coefficients and operators form, including terms involving  $\omega$ ,  $\varepsilon_r$  and  $\mu_0$  as well as derivatives  $\partial/\partial x$  and  $\partial/\partial y$ . When the periodic structure is introduced (using Bloch theorem), the field components are expanded into a Fourier series (1.9). This transforms the continuous operator equations into a matrix eigenvalue problem. Here,  $a_{x,m,p,q}$  are the Fourier coefficients for the electric field components  $E_x$  respectively. Similarly,  $b_{x,m,p,q}$  are the Fourier coefficients for the magnetic field components  $H_x$ , respectively. Expression (1.8) is then solved using transmission-line methods. Total reflectance and total transmittance can also be derived, along with the spatial field distribution.

This thesis utilized a commercial software package called RSoft's DiffractMOD to study various diffractive optical structures. This software is a RCWA-based solver that can address

scattering problems for complex periodic structures with both dielectrics and metals, and materials can be lossy and dispersive. DiffractMOD applies to a broad class of devices including diffraction gratings, polarization-sensitive devices, solar cells, and more.

## 1.2 PIC Fabrication Method

Fabrication of passive photonic integrated circuits involves several steps[24], [25]. Figure 1.1 illustrates the complete fabrication process of EBL used for the fabrication process of waveguides, and multiplexers, as it offers a high-resolution patterning technique used to fabricate extremely small structures, often at the nanoscale (sub-10 nm) resolution. A silicon wafer (525  $\mu\text{m}$  thick) is cleaned and polished to ensure a smooth and uniform surface. A thin layer of silicon dioxide ( $\text{SiO}_2$ ) having a 2.2-micron thickness is grown on the surface of the wafer through a thermal oxidation process. A layer of  $\text{Si}_3\text{N}_4$  is deposited onto the oxide layer using a low-pressure chemical vapor deposition (PECVD) process. The thickness of the  $\text{Si}_3\text{N}_4$  layer is 300 nm, which serves as the core waveguide layer. The detailed description of waveguiding will be provided in section 2.2. The wafer is further cleaned in Acetone and Isopropyl alcohol (IPA) and spin-coated with a 450 nm thick layer of ZEP 520A resist onto the  $\text{Si}_3\text{N}_4$  layer, followed by baking. The devices were patterned using EBL at an acceleration voltage of 100 kV, where a highly focused electron beam scans across a resist-coated substrate, modifying its solubility. EBL represents a type of maskless lithography, which removes the necessity for a physical mask to outline the final design. Rather, the intended patterns are created with specialized software, and then directly imprinted onto the resist through the meticulous control of an electron beam as it traverses the surface of the sample. EBL offers exceptional resolution at the nanometre scale, as the wavelength of the high-energy electrons is significantly smaller than that of ultraviolet (UV) photons.

The sample is later developed in n-amyl acetate solution for 90 seconds and rinsed with IPA. Further dry etching, an anisotropic etching process that uses a combination of chemical reactions and ion bombardment to etch materials, is performed. In this process, the patterns are transferred onto the PECVD  $\text{Si}_3\text{N}_4$  layer in a vacuum chamber by performing an inductively coupled plasma (ICP) etch step with  $\text{O}_2$ :  $\text{CHF}_3$  chemistry in a 4:21 ratio. The reactive species in the plasma chemically interact with the exposed material, while the ions strike the wafer, physically removing the reaction products. The resulting etch rate is approximately 90 nm/min. Finally, any residual resist was removed using a bath of 1165 remover for 30 minutes and an  $\text{O}_2$  plasma de-ashing step. Following the inspection of the Scanning electron microscopic image, a 1  $\mu\text{m}$ -thick  $\text{SiO}_2$  layer was deposited using PECVD.

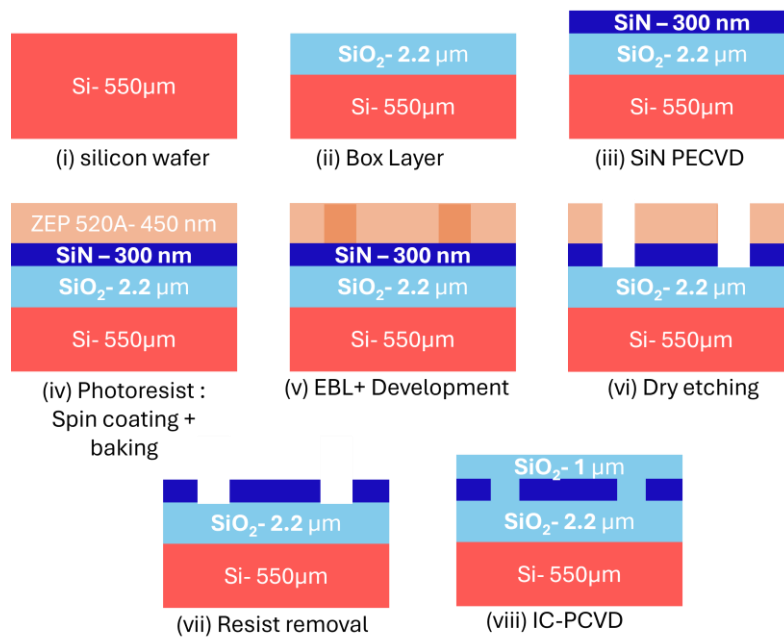


Figure 1.1: Fabrication process flow of  $\text{Si}_3\text{N}_4$  on  $\text{SiO}_2$  platform

EBL is not ideal for large-area exposure due to its high cost. In contact photolithography, involves placing the photomask in direct contact with the wafer, which is simpler and faster but generally offers lower resolution and can risk damaging the mask or wafer due to physical contact. Instead, mask stepper photolithography is employed to fabricate meta surfaces with a minimum feature size of 0.6  $\mu\text{m}$ . In stepper photolithography, a projection-based technique is used to reduce the image of the photomask and is projected onto the wafer in small sections (steps), allowing for high-resolution patterning and better alignment accuracy. This is a single step etching process, used to create  $2.5 \times 2.5$  mm metasurfaces, each designed to operate at a wavelength of 3270 nm. The photolithography process consists of several stages. The sample is exposed to ultraviolet (UV) light through a photomask, which is typically sourced from commercial mask manufacturers. Light-sensitive polymers known as photoresists play a critical role in pattern transfer [26]. Extreme Ultraviolet (EUV) lithography poses unique challenges, as EUV light is strongly absorbed by most materials, necessitating the use of reflective optics. A typical EUV lithography system uses at least three mirrors in the illumination optics and six in the projection optics. Due to the multiple reflections required, the system's total reflectivity is significantly lower, about 100 times less, than that of a single mirror. Enhancing the reflectivity of each mirror can improve overall system efficiency by several times, leading to higher spatial resolution, increased EUV intensity, and faster processing. These improvements also contribute to reduced production costs by shortening exposure times.

### 1.3 Free-Space Optical Characterization

The fabricated sample (multiplexer) underwent optical characterization using end-fire measurement setup, as shown in Figure 1. 2. The sample is positioned on a combined rotational-linear stage. Individual alignment procedures for each wavelength are carried out, using the Yenista Optics tunable laser source (TLS), for 1530 nm, and a diode laser from Eblana Photonics for 1653.7 nm. The light generated is fed to an aspheric collimating lens (10X) through optical fiber and a polarizing beam-splitter (PBS) is used to filter out the TM components. At this stage, the light is coupled to the device using a 60x focusing lens. A symmetrical arrangement is carried out to collect output. This procedure is performed from both the left and right directions to achieve inline alignment. The alignment is achieved by maximizing the output power, using a Thorlabs power meter.

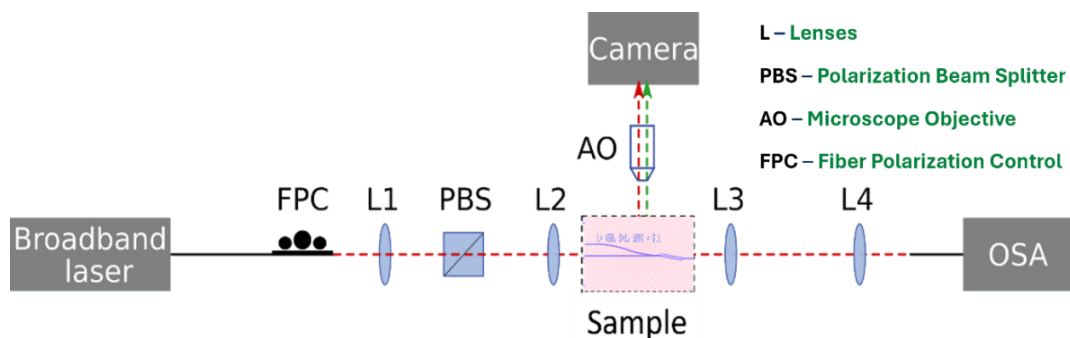


Figure 1. 2: End fire characterization setup for duplexer.

Following the alignment process, the TLS is replaced with an amplified spontaneous emission source (ASE) broadband light source (from Amonics ALS), while the diode laser is substituted with a super luminescent source from Amonics ASLD, to track the performance trend of the device in wide wavelength range.

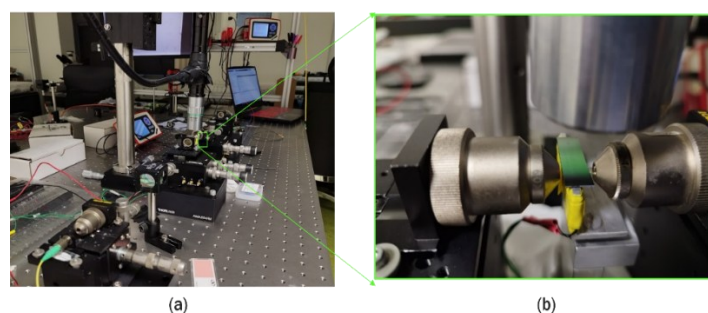


Figure 1. 3: (a) Laboratory arrangement of view end fire setup (b) Zoomed-in view of sample insertion.

For multiplexers, it is important to find the optimal device that provides the maximum coupled output power for each target wavelength. The resulting transmittance spectrum for each

port is separately collected using a Yenista Optics Optical Spectrum Analyzer (OSA). The laboratory setup of end fire method is shown in Figure 1. 3. A similar end-fire measurement setup is shown in Figure 1. 4, replacing the objective lens using lensed fiber. Lensed fiber helps for easy alignment and reduces the free space optical loss in the characterization of fabricated samples. Each device port was measured separately. The light source was focused on input ports and the output was collected using lensed fibers. Two different lensed fibers were used during characterization: the first, made from SMF-28, for input wavelengths of 1530 nm and 1653.7 nm, while the second covered the wavelength of 2003 nm.

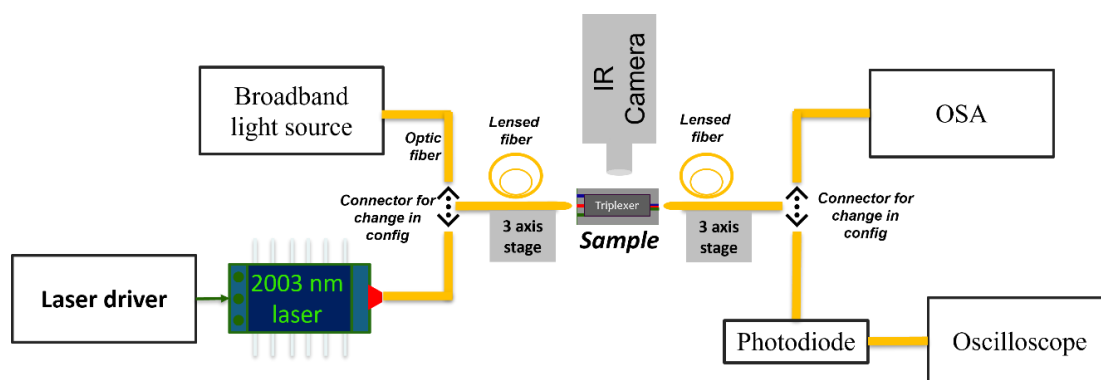


Figure 1. 4: Two different Triplexer characterization setups by switching between dotted connectors.

In the second configuration, dedicated to the characterization of target wavelength 2003 nm, the sample was initially aligned with a 1630 nm TLS source, to which the IR camera is relatively sensitive. This IR camera was employed to ensure precise alignment between the triplexer sample's input/output and the lensed fiber, which is fundamental to these measurements. The TLS was then replaced with a 2  $\mu\text{m}$  diode laser. The wavelength and power of the laser are controlled by the laser driver. The sample was tested using a lensed fiber suitable for the 2  $\mu\text{m}$  range and the output beam was collected using another 2  $\mu\text{m}$  compatible lensed fiber. The output was measured using a photodiode connected to an oscilloscope.

### 1.3 Laser Modulation and Detection Techniques

QEPAS and LITES gas spectroscopic techniques employ diode lasers, QTF and other electronic devices for the detection and quantification of various gas molecules. The lasers are externally modulated at half frequency ( $f_0/2$ ) corresponding to the resonance frequency of the QTF. The frequency of the laser light is modulated using a periodic function, typically a sine wave [27]. This sine wave is applied to the laser current driver (CD) via a sinusoidal external dither, inducing variations in the laser's emission wavelength. This method is known as Wavelength Modulation (WM) and has the primary advantage of minimizing the impact of noise

within the detection bandwidth on trace-gas measurements. Each harmonic of the analytical WM signal can be detected coherently with phase-sensitive detection electronics, such as a lock-in amplifier. However, the detection band should be high enough to limit the  $1/f$  laser noise[28]. To eliminate the need for manually tuning the laser current to generate spectrographic data, an additional ramp signal is applied to the current driver. This ramp enables very high-resolution linear scanning of the laser current, which is proportional to sweeping the laser wavelength across the gas absorption line.

The interaction between the chemical species and the modulated light leads to the generation of acoustic waves in QEPAS and localized heating effect in LITES, at respective modulation frequency and harmonics of QTF. Each harmonic of the analytical WM signal can be detected coherently with phase-sensitive detection electronics, such as a lock-in amplifier. However, the detection band should be high enough to limit the  $1/f$  laser noise[28]. When integrating the WM technique with QEPAS or LITES, the laser light is modulated at half of the QTF resonance frequency, denoted as  $(f_0/2)$ . In this way, a double intersection of the absorption line is obtained for a frequency scan. This approach, also called  $2f$ -WMS detection, is preferred for several reasons. First, when the lock-in amplifier captures the amplitude variation at the chosen harmonic of the modulation frequency, it enables the extraction of the signal envelope. Next, due to the nonlinearity of the absorption coefficient at the central frequency, higher harmonics are generated in  $1f$  signal profile, which deviates from a true first derivative of the absorption line shape.

Ideally, only the laser's wavelength should be modulated, but in practice, the laser's intensity is also modulated. This unintended modulation of intensity is called Residual Amplitude Modulation (RAM) [29]. However, RAM introduces a first-derivative component into the  $2f$  signal, which distorts the  $2f$  signal. To accurately measure gas concentrations, it's crucial to minimize or account for the distortions caused by RAM. For this reason, the laser wavelength modulation depth, and light intensity modulation, must be optimized at each gas pressure to obtain the highest  $2f$ - signal. In some cases, the detection phase can be adjusted to minimize the impact of RAM.

### 1.3.1 QTF Electrical Characterization

This section introduces the methodologies for determining the natural frequency of QTFs, the instrumentation used for these measurements, and the calculation of the Q-Factor. QTFs serve as the core sensing technology in QEPAS and LITES techniques. Their widespread adoption is attributed to their precision, compact size, stability, and the unique piezoelectric properties

of quartz. Quartz exhibits a piezoelectric effect, allowing mechanical stress to generate an electrical signal and, conversely, an electric signal to induce mechanical vibrations. Structurally, a QTF consists of two prongs with a T-shaped base (as illustrated in Figure 1). In general, the QTF prongs used in gas sensing are approximately 20 mm in length, 1.4 mm in width, and 0.8 mm in thickness, with a separation gap of 1 mm between them. The Q-Factor is determined by the physical structural parameters of the QTF. Each QTF possesses a natural resonant frequency at which it vibrates with maximum amplitude, a critical parameter in gas sensing applications. The natural frequency of a QTF is intrinsically determined by its structural parameters, such as length, width, thickness, and separation gap between the prongs. These parameters influence the mass and stiffness of QTF, which in turn define its vibrational characteristics [30], [31]. A higher Q-Factor indicates lower energy loss and sharper resonance peaks, which are important for high-sensitivity gas detection. Electrical characterizations of the QTF, which uses the inverse piezoelectric effect, are conducted at various stages of assembly to ensure the spectrometer is constructed with optimal precision and performance.

For example, the electrical characterization of the QTFs involved is explained for two differently manufactured QTFs, referred to as QTF<sub>1</sub> and QTF<sub>2</sub>. These characterizations involve applying a modulated electric field to induce mechanical vibrations and analyzing the resulting electrical signals to validate the QTF's functionality. The electrical characterization of the QTF was conducted under controlled environmental conditions, maintaining a constant temperature of 24.5°C, a relative humidity of 68% and continuously modulating the electrical voltage, via a sinusoidal voltage signal. This modulation generates piezoelectric charges, which are collected by gold contacts on the QTF prongs. The QTF output signal was amplified using a transimpedance amplifier stage with a feedback resistance of 10 MΩ and is connected to a lock-in amplifier (models from Anfattec and Zurich Instruments) to filter and demodulate the piezoelectric currents generated by the QTF. Before this, an amplitude modulation optimization was performed. A sinusoidal signal with an amplitude of 240 mV<sub>pp</sub> and an offset of 2 V, generated by an Arbitrary Function Generator (WFG), was input to the preamplifier having feedback resistor ( $R_f = 10\text{M}\Omega$ ), and subsequently fed into a lock-in amplifier for reference signal. This Lock in signal is scanned over a narrow frequency range, aiming to extract their respective resonance curves. The lock-in integration time was set to 100 ms, and the demodulated signals were acquired using a DAQ with an acquisition time of 300 ms. These signals were then displayed on a PC as a voltage signal through a NI LabVIEW interface. Alternatively, when using Zurich Instruments' lock-in amplifier, the device was directly connected to the PC. The schematic of the electric characterization setup of the QTF is depicted in Figure 1.5 (a).

The electrical response of the QTFs as a function of frequency, along with the corresponding Lorentzian fits, is presented in Figure 1.5. The QTF response was evaluated across a range of frequencies, with signal amplitudes measured at the resonance frequency ( $f$ ). The Full Width at Half Maximum (FWHM) was derived by fitting the experimental data to a Lorentzian model. QTF<sub>1</sub>, having resonance frequency  $f_1 = 8.12462$  kHz with a calculated Q-factor of 11390, from resonance curve Figure 1.5 (b). Similarly, QTF<sub>2</sub>, having resonance frequency  $f_2 = 12.4527$  kHz with a calculated Q-factor of 14823, from resonance curve Figure 1.5 (c).

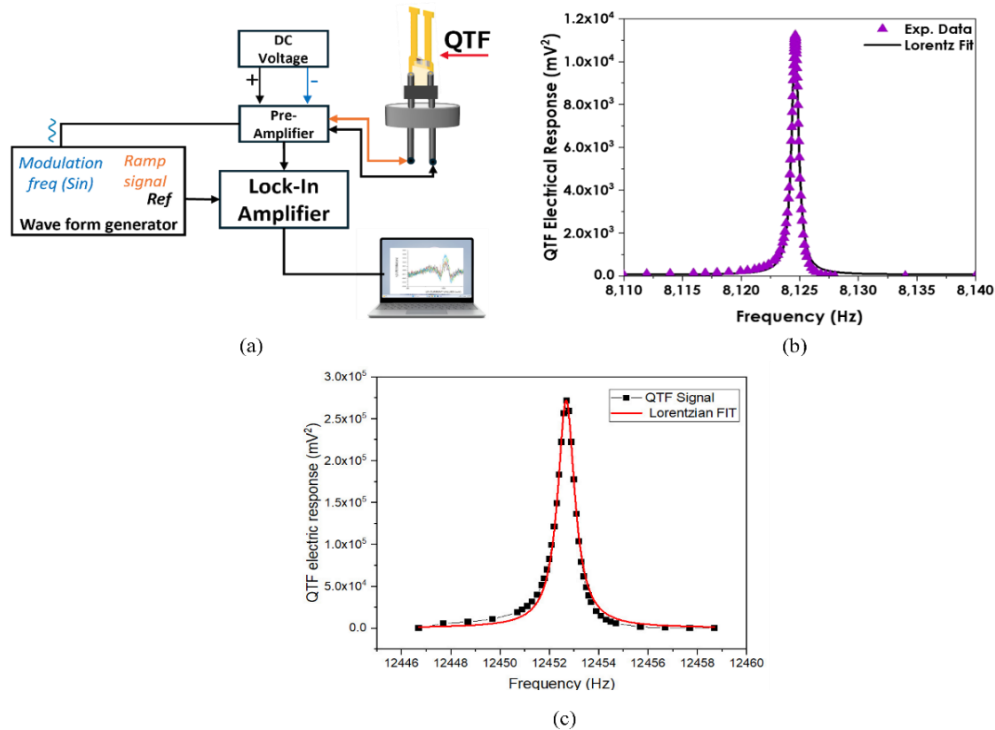


Figure 1.5: (a) Schematic of electric characterization setup of the QTF. Resonance curve as a function of frequency for the electrical characterization of (a) QTF<sub>1</sub> and (b) QTF<sub>2</sub>.

These high Q-Factor values signify minimal energy loss and sharp resonance peaks, which are critical for achieving high sensitivity in measurement applications. The QEPAS and LITES experimental setups are explained in their respective sections of the thesis. The QTF characterization framework, explained in Chapter 3, for sensing applications involving gases like methane and water vapor. QTF electrical characterization for natural frequency is continuously recorded during measurements performed across various characterization setups and experimental conditions. The two commonly used lithography techniques for PIC fabrication EB and stepper-based photolithography are employed multiple times throughout different phases of the research. The fabricated samples undergo optical characterization using an end-fire setup, which is modified as needed based on the research application. This setup is further modified to facilitate chip-to-QTF integration.

# Chapter 2- Advanced PICs for Multi-Gas Sensing

Chapter 2 presents the design, fabrication, and characterization of compact, low-loss, broadband duplexers and triplexers operating in the near-infrared (NIR) region. The focus is on achieving high selectivity and coupling efficiency at spectroscopically relevant wavelengths. These devices utilize an angled Multimode Interference (MMI) coupler and a Directional Coupler (DC), both optimized for operation within the NIR range. The chapter also reviews the theoretical foundations of MMI and DC structures. Additionally, the input waveguide design strategy is described, with particular emphasis on wavelengths corresponding to key gas absorption lines: 1530 nm for ammonia ( $\lambda_{NH_3}$ ), 1653.7 nm for methane ( $\lambda_{CH_4}$ ), and 2003 nm for carbon dioxide ( $\lambda_{CO_2}$ ).

## 2.1 Introduction

The ever-growing demand for real-time, low-loss multi-gas sensors has accelerated the development of optical couplers capable of combining two (duplexers), three (triplexers), or more spectroscopically relevant wavelengths. By rapidly switching between optical sources, integrated multiplexers enable the detection of multiple gases with high temporal resolution. Instead of deploying separate detector systems for each target gas, an on-chip laser paired with a QEPAS sensor can detect multiple gases in real time. This approach yields a lightweight, compact, and highly sensitive sensing system ideal for applications such as agricultural or environmental monitoring. It is worth stressing that the absorption lines of interest are separated by more than  $>600$  nm, posing challenges for the design of the combiner. A Vernier effect-based quantum cascade laser (QCL) system employing QEPAS has been demonstrated for the detection of Carbon Monoxide (CO), Nitrous Oxide (N<sub>2</sub>O), and Carbon Dioxide (CO<sub>2</sub>), with absorption peaks at 4708 nm, 4520 nm, and 4457 nm, respectively [32]. However, this system exhibits limited spectral selectivity, and free-space optical configurations are prone to misalignment of mirrors and lenses. Additionally, these devices also face trade-offs among size, weight, sensitivity, selectivity, lifetime, calibration, and operation in harsh environments. Portability remains a key challenge, especially for wide area sensing in agricultural or remote settings. Addressing these issues through lightweight, compact, and cost-effective designs remains crucial.

Optical fiber-based solutions on the one hand offer benefits in terms of compactness and lightweight designs. On the other hand, challenges are still faced related to material selection, the need for collimators, dispersion, nonlinearity, absorption losses due to interactions with optical phonons, inherent fragility, and complicated deployment in harsh environments [33], [34], [35], [36].

Numerous combiner designs have been proposed to address wide spectral separation. One approach relies on MMI couplers such as straight, angled, butterfly, or cascaded MMI couplers [37], [38]. Other solutions are based on Y-junction couplers, Mach-Zehnder interferometer couplers, and symmetric or asymmetric DCs [39], [40].

The proposed duplexer/triplexer performance was optimized by selecting a suitable refractive index of the guiding region and coupler geometry. A  $\text{Si}_3\text{N}_4$  platform was chosen for its broad bandwidth and lower propagation loss. Coupling efficiencies were evaluated across various mode profiles, including the fundamental, higher-order modes, as well as commercial diode-laser mode profiles. The key parameter is the output power from the multiplexer, which determines sensitivity and selectivity in target gas detection. This lightweight technology can be integrated into unmanned aerial vehicles for wide-area gas sensing. This novel passive coupler system represents a breakthrough in real-time, lightweight, compact sensors for agricultural field monitoring, breath analysis, hydrocarbon monitoring, leak detection, and hotspot monitoring.

## 2.2 Design Strategies for Input Waveguide

The multiplexer device configurations are realized based on the  $\text{Si}_3\text{N}_4$  on silicon dioxide ( $\text{SiO}_2$ ) platform. It is important to consider the future integration and packaging possibilities for sensors and micro lasers. Commercially available distributed feedback lasers from NanoPLUS (Germany), are the preferred choice for spectroscopy. The output mode profiles of DFBs based on InP, emitting at wavelengths of 1654 nm and 2003 nm respectively, are utilized for numerical analysis to optimize the input waveguide dimensions. Optimizing the input waveguide dimensions is essential for achieving maximum coupling efficiency of the laser power from the selected lasers. This involves tailoring the waveguide dimensions to closely match the mode profiles of the lasers, ensuring efficient light transfer and minimal power loss [38], [41]. Figure 2.1 illustrates the micro-lasers and their characteristics: (a) shows an image of the micro-lasers, and (b) presents the simulated output mode profiles. The coupler design was performed using the 3D FD-BPM (BeamPROP simulation tool, provided by RSoft) [15], [16]. The computational mesh grid resolution of the simulation domain was optimized along the three spatial axes

of  $X = 100$  nm,  $Y = 100$  nm, and  $Z = 50$  nm. The Sellmeier equation is utilized to account for material dispersion. Specifically, Philipp 1973 for  $\text{Si}_3\text{N}_4$  [42] and Malitson 1965 for silicon dioxide [43].

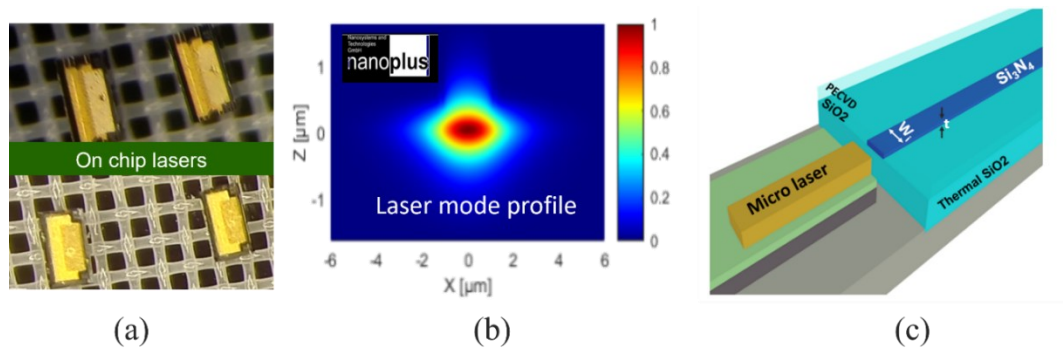


Figure 2.1: (a) commercial diode micro lasers (b) The simulated output mode profile of diode laser (c) the schematic of laser to on-chip waveguide integration

Extinction coefficients ( $k$  values) were approximated as being zero in this process, which is reasonable, given the published loss values for  $\text{Si}_3\text{N}_4$ . To provide a comprehensive evaluation of the dielectric characteristics, various assessment methods for comparison are presented. Figure 2.2 illustrates the refractive index as a function of wavelength for  $\text{Si}_3\text{N}_4$  and silicon dioxide, determined using three methods: the Sellmeier equation, the RSoft material library, and ellipsometry measurements.

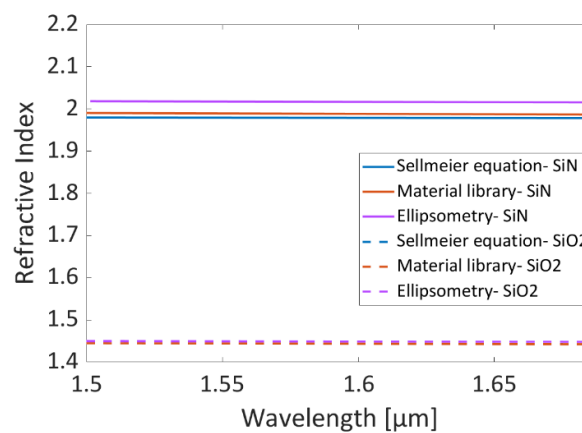


Figure 2.2: Refractive index changes for  $\text{Si}_3\text{N}_4$  and silicon dioxide against wavelength

The width of the input waveguide ( $W_i$ ) and thickness ( $t$ ) from Figure 2.1(c) are optimized to maximize with respective laser mode coupling to the input waveguide dimension. The mode profile is optimized to  $W_i = 3$  μm and  $t = 300$  nm for wavelengths of interest 1530 nm, 1654 nm and 2003 nm. The optimal value was found to be 77%, 75 %, and 80%, respectively. Various cladding materials such as air, PMMA,  $\text{SiO}_2$ , and SU-8 were also investigated. Figure 2.3 (a) and (b) illustrate the transmittance variation with cladding thickness for various material at

1530 nm and 1653.7 nm, respectively. The transmittance is recorded on a scale from 0 to 1, corresponding to a percentage range, representing the fraction of light passing through the waveguide. Due to ease in attaining uniformity in cladding thickness and flat response in transmittance for varying cladding thickness, SiO<sub>2</sub> cladding is selected with a thickness of 1  $\mu\text{m}$  for both wavelengths, as it facilitates integration on the same platform. The cladding thickness equal to 1  $\mu\text{m}$  gives optical power transmittance equal to 92%, 93%, and 80% for input wavelengths equal to 1530 nm, 1653.7 nm, and 2003 nm, respectively.

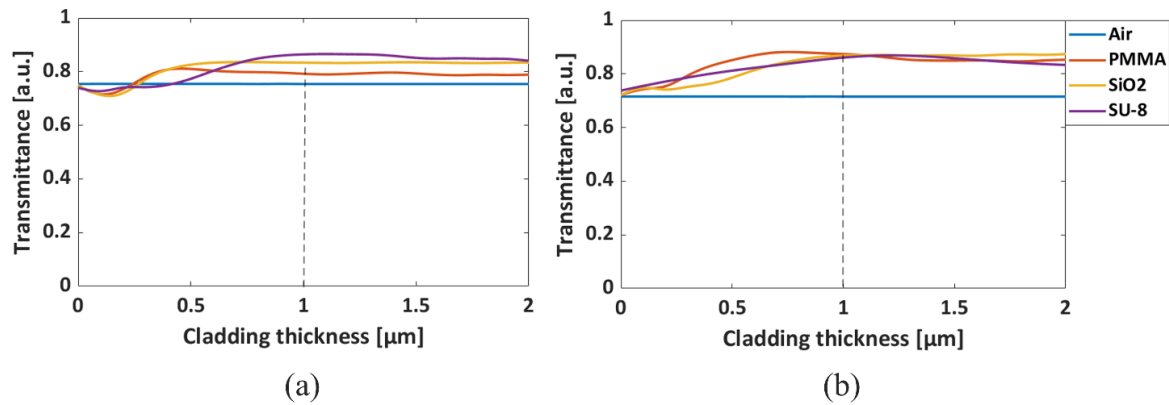


Figure 2.3: Transmittance for various cladding thicknesses at (a) 1530 nm and (b) 1653.7 nm.

The electric field profile of the computed fundamental modes of the waveguide cross-section for wavelengths equal to 1530 nm is shown in Figure 2.4. The effective refractive index ( $n_{eff}$ ) of the fundamental mode (M00) for wavelengths equal to 1530 nm, 1653.7 nm, 1684, and 2003 nm are 1.649, 1.627, 1.621 and 1.535, respectively. It is important to point out that the input waveguide can also support higher order modes M01, which have  $n_{eff}$  of 1.499, 1.448, and 1.38, respectively. However, for the higher wavelength 2003 nm, the higher order mode is not supported. The corresponding mode profiles have been used to investigate the device's performance.

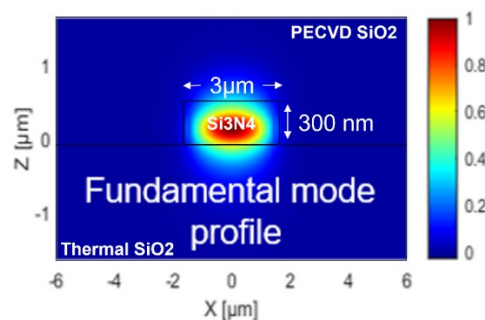


Figure 2.4: Computed fundamental mode profile for 1530 nm at  $W_i=3 \mu\text{m}$  and  $t=300 \text{ nm}$ , with 1  $\mu\text{m}$  SiO<sub>2</sub> cladding thickness.

Higher-order modes can significantly impact waveguide transmittance by causing modal interference, and crosstalk [44]. To account for the distribution of modes within the waveguide, both behaviours of fundamental mode and higher order mode are investigated when launching the laser mode profile.

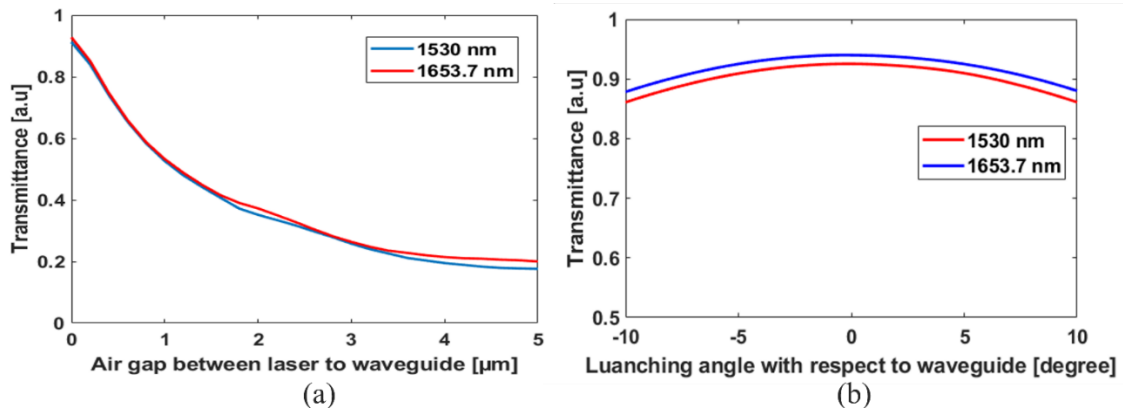


Figure 2.5: S-bend loss of  $\text{Si}_3\text{N}_4$  waveguide (a) Bend angle as a function of wavelength, insight bend radius at a fixed angle of 14 degrees. Laser to chip in integration (b) as a function of the gap between the source and waveguide (c) titling the angle of input waveguide.

For the futuristic integration of multiple diode lasers die at the input waveguides, a minimum separation of 300  $\mu\text{m}$  is required. Furthermore, the coupling loss between the laser and the waveguide at different angles are analyzed. Figure 2.5 (a) illustrates the losses caused by the presence of an air gap between the laser and the chip. Ongoing research aims to minimize or eliminate this gap to enhance integration. Additionally, Figure 2.5 (b) shows the loss resulting from angular deviations between the chip and the source. These deviations can be expected due to imperfections in the chip-cleaving process.

## 2.3 Compact Angled Multimode Interference Duplexers

Multimode Interference (MMI) can perform various optical functions such as splitting, combining, and routing optical signals [45], [46]. These devices are becoming increasingly important in integrated photonics due to their compact size, low loss, and ease of fabrication. They are relatively insensitive to polarization, making them highly suitable for optoelectronic integration [47]. MMI couplers can be classified in several ways, including by their structure and the interference mechanism they employ. Some of these classifications include symmetric, general, angled, butterfly, and cascaded MMI couplers [48]. Several studies have demonstrated the effectiveness of MMI-based wavelength demultiplexers. Devices operating at 1310/1490/1550 nm have shown practical applicability [47], [49], while others support fiber to home applications by combining 980, 1310, 1490, and 1550 nm wavelengths with insertion losses between 0.52 and 1.54 dB and good channel isolation [50]. An InP-based asymmetric multi-section MMI splitter efficiently separates 1.31 and 1.55  $\mu\text{m}$  wavelengths with reduced device length [51]. A  $1 \times 4$   $\text{Si}_3\text{N}_4$  demultiplexer operating in the C-band (1530–1560 nm) achieves insertion losses of 1.986–2.351 dB and low crosstalk [52]. Silica-based  $2 \times 2$  MMI couplers exhibit low insertion losses ( $<0.4$  dB), minimal imbalance, and low polarization sensitivity [58]. A wavelength-independent directional coupler on SOI with MMI structures supports broadband operation (1525–1625 nm) with  $\sim 0.8$  dB excess loss [53], while silicon nanowire-based couplers maintain  $<1.55$  dB loss across 1.49–1.59  $\mu\text{m}$  [54]. Cascaded MMI couplers, such as  $1 \times 4$  demultiplexers made from  $1 \times 2$  sections, enable complex functionality but may increase losses compared to single-stage designs [50].

In contrast, Angled MMI couplers offer more versatility in terms of features and coupling efficiency compared to straight MMI couplers. The angled MMI was first proposed by Y. Hu et al. and shows excellent characteristics in terms of low loss, compactness, superior fabrication tolerances, and the capability to filter out higher-order modes [39]. Angled-MMI-based wavelength splitters designed for  $\text{Si}_3\text{N}_4$  applications in fluorescence sensing demonstrate remarkable performance in visible light [55]. The diplexer, operating at 665 nm and 705 nm, achieves insertion losses below 1.7 dB per channel and crosstalk under -24 dB. The triplexer adds a 638 nm channel with slightly higher insertion losses below 2.5 dB per channel and crosstalk below -17 dB. A more compact alternative that provides both efficient optical power output and the simultaneous integration of various desired wavelengths is the angled MMI approach. The performance of angled MMI couplers is sensitive to geometrical parameters, such as angles and

spacing between waveguides. The lengths of angled MMI devices are determined based on the wavelengths and the  $n_{eff}$ .

A compact, low-loss  $2 \times 1$  angled-multi-mode-interference-based duplexer is proposed as an optical component for integrating several wavelengths with high coupling efficiency. The self-imaging principle in multimode waveguides is exploited to combine two target wavelengths, corresponding to distinctive absorption lines of important trace gases. The devices' performance has been numerically enhanced by engineering the geometrical parameters, offering trade-offs in coupling efficiency ratios. The proposed designs are used as versatile duplexers for detecting gas combinations such as ammonia-methane, ammonia-ethane, and ammonia-carbon dioxide, enabling customization for specific sensing applications. The device is optimized for three different cases, namely, to combine the following wavelength pairs: (i)  $\lambda_{NH_3}$  and  $\lambda_{CH_4}$ , (ii)  $\lambda_{NH_3}$  and  $\lambda_{C_2H_6}$ , (iii)  $\lambda_{NH_3}$  and  $\lambda_{CO_2}$ .

### 2.3.1 Theoretical Principles of MMI and Angled MMI

The principle of self-imaging was first described by H.F. Talbot in 1836, using coherent illumination on periodic objects [56]. Later, in 1995, L. B. Soldano expanded on this concept, providing a theoretical explanation of self-imaging in both symmetric and asymmetric MMIs. MMI devices can accommodate a high number of modes, that are differentiated in terms of their different phase velocities. When a single mode is injected into the multimodal region from an input port, the crossing of the discontinuity at the combiner inlet allows it to spatially disperse, resulting in the excitation of all available modes (while the total power is conserved). These modes then interfere with their reflections from the multimodal region boundaries. Due to the self-imaging principle in the presence of modal dispersion, the injected mode is then regenerated along the propagation direction at positions whose distance from the injection point is an integer multiple of the beating length ( $L_\pi$ ) [57].

Symmetric and general MMI couplers are the most basic type of MMI couplers, these typically feature multiple access waveguides at their input ( $N$ ) and output ( $M$ ) for launching and collecting light, commonly referred to as  $N \times M$  MMI couplers. Starting from the dispersion equation for a waveguide with a  $n_{eff}$ , an injected wavelength ( $\lambda_0$ ), and a supported mode number ( $v$ ), the propagation constant,  $\beta_v$ , can be expressed as:

$$\beta_v = k_0 n_{eff} = \frac{(v+1)\pi}{4\lambda_0 n_{eff} W_{eff}} \quad (2.1)$$

The effective width MMI is approximated to the width of the MMI waveguide ( $W_{mmi}$ ), for high-contrast waveguides. Thus, the  $L_\pi$  is defined for the least of the two lowest-order modes for symmetric MMI,

$$L_\pi = \frac{\pi}{\beta_0 - \beta_1} = \frac{n_{eff} W_{mmi}^2}{\lambda_0} \quad (2.2)$$

These images are symmetrically located along the lateral axis with equal spacing. For the general MMI, the beat length is calculated by

$$L_\pi = \frac{4 \cdot n_{eff} W_{mmi}^2}{\lambda_0} \quad (2.3)$$

Figure 2.6 shows the simulation results for symmetric MMI, showing multiple self-imaging positions for a  $W_{mmi}$  of 10  $\mu\text{m}$  at an input wavelength of  $\lambda_0 = 1530$  nm. From Eq. 2.3 the calculated beat length for straight MMI is  $L_\pi = 110$   $\mu\text{m}$ . For the same configuration, when launching from the non-symmetric position as case of general MMI, the  $L_\pi$  is 430  $\mu\text{m}$ .

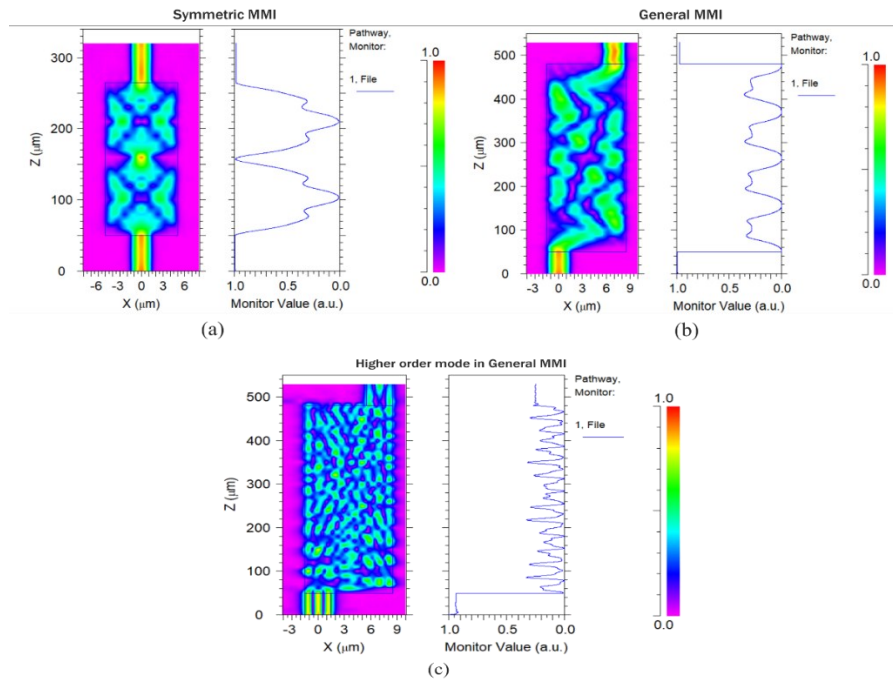


Figure 2.6: Electric field profile for injecting fundamental mode with pathway monitor (a) Symmetric MMI (b) General MMI and (c) higher order mode injection in general MMI.

Figure 2.6 (b) illustrates, demonstrates the effects of higher-order modes, which act as a filtering effect at the output when optimized for fundamental mode operation. The monitor used in simulation corresponds to the field of launch mode. This comes from the fundamental depends on  $L_\pi$  with mode number. A specific operational mechanism in MMI devices exploits the self-imaging principle to achieve power splitting and combining functions.

The operation of angled MMI devices is built upon the fundamental principles of general MMI while introducing angular modifications to enhance functionality. A single mode is injected into the multimodal region and regenerated at the output. Due to the presence of  $\beta$  angled, side coupled adjacent input waveguide ( $WG_2$ ), the multimode region causes discontinuity in the symmetry. To target the regenerated position of  $WG_1$  at higher wavelengths, the position of  $WG_2$  is adjusted. The change in wavelength is directly proportional to gap between the waveguide, ie inversely proportional to effective length of MMI ( $L_{mmi}(WG_2)$ ). A schematic of Angled MMI configuration is presented in Figure 2.7. By differentiating Equation (2.4) and by considering the tilted angle in the multimode region, the minimum channel spacing ( $\Delta\lambda_{min}$ ) of the angled MMI device can be expressed as:

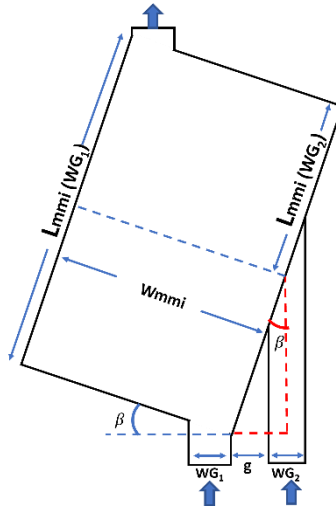


Figure 2.7: Sketch of the Angled MMI configuration representing the theoretical parameters.

$$\Delta\lambda_{min} > \frac{W_{in}+g}{4 n_{eff} \sin \beta} \left( \frac{\lambda_{in}}{W} \right)^2 \quad (2.4)$$

where  $g$  is the minimum separation between the adjacent input waveguides,  $W_{in}$  is the width of the input waveguide and  $\beta$  is the angle between the input waveguides and the multimode waveguide[58]. The introduction of an angled MMI waveguide adds versatility to the device, allowing for finer wavelength separation, as characterized by the minimum channel spacing ( $\Delta\lambda_{min}$ ). These adaptations make angled MMI devices an effective solution for compact, high-performance optical systems requiring precise wavelength multiplexing and minimal crosstalk.

### 2.3.2 Proposed Structure and Numerical Result

The design configuration of angled MMI includes an input section consisting of two waveguide ports, in which two signals of different wavelengths are injected. These ports (labeled as “A” and “B”) are then connected to the coupler, whose function is to combine the two signals while

maximizing their transmittance. The proposed angled MMI -based duplexer, whose sketch is shown in Figure 2.8, exploits  $\text{Si}_3\text{N}_4$  guiding elements placed on top of a silicon dioxide ( $\text{SiO}_2$ ) substrate. The device is composed of three cascaded parts: an input section, a combiner (labeled as “core”), and an output section. The input section consists of two waveguide ports  $WG_1$  and  $WG_2$  separated by a gap  $g$ , allowing the injection of two signals of different wavelengths, namely  $\lambda_{\text{NH}_3}$  and  $\lambda_j$ , into the system. The  $\lambda_j$  will assume the value of wavelengths  $\lambda_{\text{CH}_4}$ ,  $\lambda_{\text{C}_2\text{H}_6}$ , and  $\lambda_{\text{CO}_2}$ , depending on the duplexer configuration, with a different value of  $g$  for each namely  $g_1$ ,  $g_2$ , and  $g_3$ , as depicted in Fig. 2.8). It is worth noting that the position of  $WG_1$  is to be considered fixed (its right edge fits into the combiner at the lower right corner of the latter). Conversely, the position of  $WG_2$ , uniquely identified by the gap  $g$ , is a function of the specific wavelength to be combined with  $\lambda_{\text{NH}_3}$  and will be a subject of optimization (for this reason,  $WG_2$  is depicted with evanescent colors in Figure 2.8).

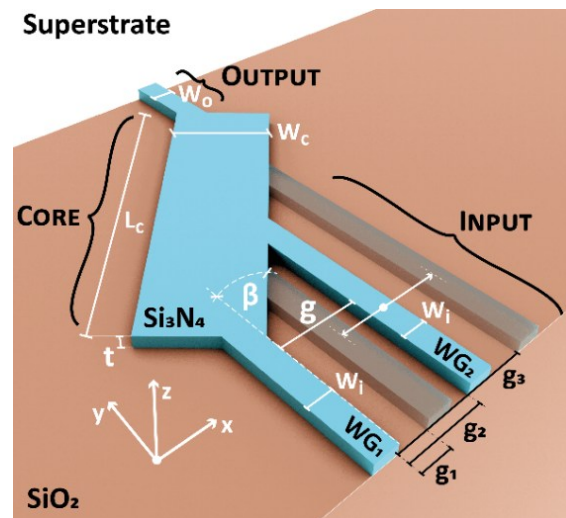


Figure 2.8: Schematic diagram of angled MMI duplexer

These waveguides are then prolonged and connected to the multimode waveguide region, where  $L_C$  is the length and  $W_C$  is the width. This multimode region is tilted on the substrate plane forming an angle  $\beta$  with respect to the direction of the input and output waveguides. Within this section, interference will result in a landscape of electromagnetic field maxima and minima that is determined by geometric parameters as well as spectral parameters and the guiding properties of the structures involved. The MMI structure allows the “long side” of the core region to be exploited as the insertion point of  $WG_2$ . The asymmetry of the structure will depend on the choice of  $g$ , which, in turn, will affect the overall transmittance. Finally, an output section consists of a single waveguide  $WG_o$ , having width  $W_o = W_i$ , whose position mirrors  $WG_1$  with

respect to the center of the core region and the x- and y- directions, where the maximum light intensity is expected according to the self-image principle.

The simulations were performed using the FD-BPM (BeamPROP simulation tool, provided by RSoft). After performing a convergence test, the mesh grid resolution was set to 50 nm, 10 nm, and 100 nm, along the x, y, and z directions, respectively. The material dispersion relation is introduced in simulations to account for the wavelength dependence of the refractive index and effectively manage loss and dispersion effects [59]. The presence of higher-order modes in the output waveguide system harms the performance of the duplexer-based sensor. Higher order modes lead to increased spatial mode dispersion, decreased self-imaging fidelity, and higher crosstalk [60]. MMI couplers excel in suppressing higher-order modes available in the input waveguides, thereby alleviating the performance limitations seen in comparison to alternative coupling methods. When  $\beta = 0$  (i.e., “symmetric” MMI case), no common self-focusing positions of the two waveguides can be found for each target pair of wavelengths. Therefore, from this point on, as the situation where  $\beta > 0$  is considered. Having fixed  $W_i$ ,  $W_o$ ,  $t$ , and  $t_c$ , the performance of the proposed duplexer was optimized by investigating the effects of varying  $L_c$ ,  $W_c$ ,  $\beta$ , and  $g$  on the total transmittance  $T_o$ . Figure 2. 9 shows  $T_o$  as a function of  $L_c$ , with  $W_c$  equal to 10  $\mu\text{m}$ , for different values of  $g$ . When  $WG_1$  and  $WG_2$  are individually excited at wavelengths  $\lambda_{NH3}$  (dotted lines) and  $\lambda_j = \lambda_{CHA}$  (solid lines), respectively - this allows us to identify  $T_o$  depending on the excited waveguide. In particular,  $T_o$  is calculated for different values of  $g$  (0.5  $\mu\text{m}$ , 1  $\mu\text{m}$ , 1.5  $\mu\text{m}$  and 2  $\mu\text{m}$ ). In general, a bell-shaped trend of  $T_o$  with varying  $L_c$  is observed. When  $WG_1$  is solely excited at  $\lambda_{NH3}$ , the change in gap value modulates the transmittance intensity, although the absolute maximum is obtained for almost the same values of  $L_c$  (i.e., in Figure 2. 9 the distribution of the dashed curves does not shift significantly along  $L_c$  axis), indicating that the beating length remains relatively stable with respect to  $g$ . Conversely, when  $WG_2$  is solely excited at  $\lambda_{CHA}$ , changing  $g$  has only a minor effect on the maximum transmittance intensity. Nonetheless, the beating length exhibits significant variation, spanning a range of approximately 10 microns (i.e., in Figure 2. 9 the distribution of the solid curves shifts toward longer  $L_c$  for increasing  $g$ ). For a fixed value of the gap and each different value of  $L_c$ , it is possible to identify a distinct combination of wavelength coupling ratios (i.e.,  $T_o$  for pairs of the same color) can be identified. Ideally, the duplexer must maximize output power  $T_o$  for both the target wavelengths, while keeping the device footprint as small as possible. Therefore, to discriminate the best combination of parameters, a figure of merit (FOM) was defined as  $T_o(\lambda_{NH3}) \times T_o(\lambda_{CHA}) / (100W_c)$ . Table 2.1 summarizes some of the best configurations in terms of FOM for the proposed duplexer, obtained in the investigated parametric space.

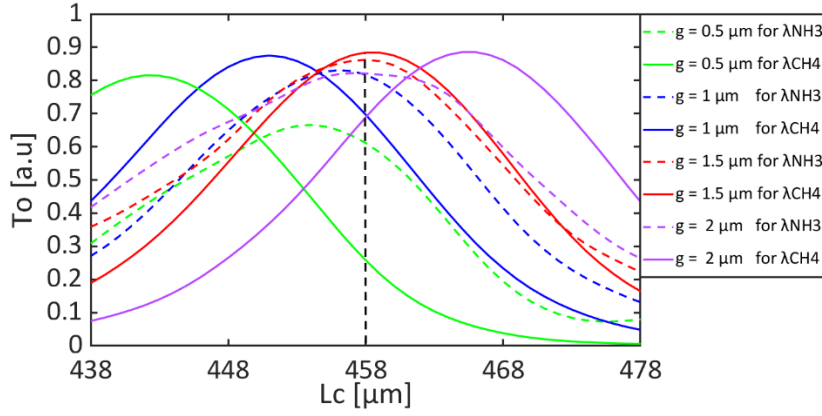


Figure 2. 9: Transmittance  $T_o$  as a function of  $L_c$  for different values of  $g$  at fixed  $W_c = 10 \mu\text{m}$  when  $WG_1$  and  $WG_2$  are individually excited at  $\lambda_{NH_3}$  (dotted lines) and  $\lambda_{CH_4}$  (solid lines), respectively.

Specifically, in Table 2. 1, the best configuration obtained in terms of FOM maximization is the one labeled "case 1". For the latter, a value of  $g$  equal to  $1.56 \mu\text{m}$  is deemed sufficient to prevent evanescent mode coupling between the two input waveguides [61]. The components of the output transmittance  $T_o$  obtained for  $\lambda_{NH_3}$  and  $\lambda_{CH_4}$ , are equal to 86% and 88%, respectively.

**Table 2. 1: Optimized output transmittance results**

Case	$W_c$ [ $\mu\text{m}$ ]	$\beta$ [ $^\circ$ ]	$g$ [ $\mu\text{m}$ ]	$L_c$ [ $\mu\text{m}$ ]	$T_o$ at $\lambda_{NH_3}$ [%]	$T_o$ at $\lambda_{CH_4}$ [%]	FOM
1	10	4	1.56	458	86	88	7.57
2	10	4	1.16	460	70	95	6.65
3	10	5	1.86	460	82	75	6.15
4	9	4	1.28	374	80.5	80	7.15
5	11	4	1.88	547	88%	88%	7.04

To further shed light on the behavior of the device, the transmittance has been studied by varying the angle of the core region. In particular, Figure 2.10 shows  $T_o$  as a function of  $L_c$  for increasing discrete values of  $\beta$  (equal to 3, 4, 5, and 6, degrees respectively), when  $W_c$ ,  $L_c$  and  $g$  are set as in "case 1" (see Table 2. 1) and when  $WG_1$  and  $WG_2$  are individually excited at  $\lambda_{NH_3}$  (dotted lines) and  $\lambda_j = \lambda_{CH_4}$  (solid lines), respectively. The vertical line in Figure 2.10 represents the  $L_c = 458 \mu\text{m}$  at which maximum  $T_o$  obtained using a figure of merit i.e., at  $\beta = 4$ , when wavelengths launched in their respective waveguides. The configuration referred to as "case 1" presents an excellent compromise in terms of both transmittance and compactness.

For this configuration, using the mode profiles of commercially available diode laser as the input excitation leads to  $T_o$  values of 71% and 77% for wavelengths of 1530 nm and 1653.7

nm, respectively. In addition, when launching higher order modes (M01),  $T_o$  reduces to 0.5% and 9% for the same wavelengths, respectively, demonstrating a good high-order mode rejection behavior. Therefore, values of  $W_c$ ,  $L_c$ , and  $\beta$  were set to 10  $\mu\text{m}$ , 458  $\mu\text{m}$ , and  $4^\circ$ , respectively.

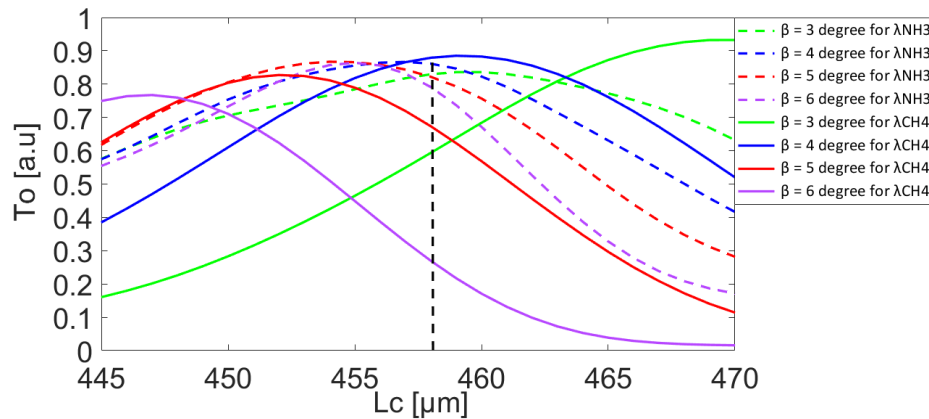


Figure 2.10: Transmittance  $T_o$  as a function of  $L_c$ , for different values of  $\beta$ , when  $WG_1$  and  $WG_2$  are individually excited at wavelengths 1530 nm (dotted lines) and 1653.7 nm (solid lines), respectively.

These geometric parameters of the core region are then used to test the operation of the duplexer in the presence of other desired wavelength combinations (i.e.,  $\lambda_{NH_3} - \lambda_{C_2H_6}$  and  $\lambda_{NH_3} - \lambda_{CO_2}$ ). For each of these combinations, the corresponding gap value is optimized, that maximizes the output transmittance. It is worth noting that the required distance  $g$  increases with increasing wavelength separation between the two input sources. Table 2.2 summarizes the numerical results obtained for the three different wavelength pairs of interest.

**Table 2. 2: Values of transmittances obtained for three different pairs of excitation wavelengths when the distance between the input waveguides  $g$  is optimized.**

Duplexer	$g$ [ $\mu\text{m}$ ]	$T_o$ for computed mode launching at		$T_o$ for laser mode profile launching at		$T_o$ for higher order mode launching at	
		[%]		[%]		[%]	
		$WG_1$	$WG_2$	$WG_1$	$WG_2$	$WG_1$	$WG_2$
$\lambda_{NH_3}$ & $\lambda_{CH_4}$	$g1 = 1.56$	86	88	68	75.5	0.5	9
$\lambda_{NH_3}$ & $\lambda_{C_2H_6}$	$g2 = 2.03$	82	88.5	65.5	77	0	3
$\lambda_{NH_3}$ & $\lambda_{CO_2}$	$g3 = 9.8$	43	84.5	30	60	30	0

Figure 2.11 illustrates the amplitude of the electric field as a function of the  $x$  and  $y$  axis. The distribution of the propagating light in the proposed device is at  $z = t_c/2 = 0.15 \mu\text{m}$ . These maps provide valuable insights into the self-focusing principle and demonstrate how the gap

between the two waveguides influences the focusing effect for different input waveguides targeting specific wavelengths.

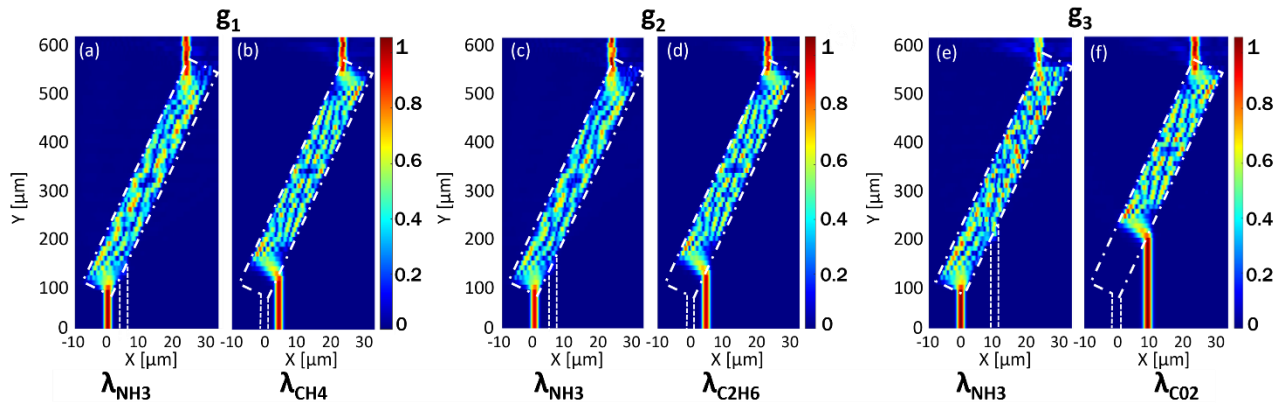


Figure 2.11: Electric field distributions as a function of the  $x$  and  $y$  coordinates at  $z = 0.15$  nm. The sole  $WG_1$  is fed with the fundamental mode at  $\lambda_{NH_3}$  (a) at  $g_1 = 1.56$   $\mu\text{m}$  (c)  $g_2 = 2.03$   $\mu\text{m}$  and (e) at  $g_3 = 9.8$   $\mu\text{m}$ . When  $WG_2$  is fed with the fundamental mode at (b)  $\lambda_{CH_4}$ , at  $g_1 = 1.56$   $\mu\text{m}$  (d)  $\lambda_{C_2H_6}$  at  $g_2 = 2.03$   $\mu\text{m}$  and (f)  $\lambda_{CO_2}$  at  $g_3 = 9.8$   $\mu\text{m}$ .

Figure 2.12 represents the transmission as a function of the wavelength within the spectra range between 1.450  $\mu\text{m}$  and 2.150  $\mu\text{m}$ , for the three configurations reported in Table 2.2. In particular, the blue color corresponds to the  $T_o$  for  $\lambda_{NH_3}$  injected in  $WG_1$  and red, gray, and green color for wavelengths  $\lambda_{CH_4}$ ,  $\lambda_{C_2H_6}$ , and  $\lambda_{CO_2}$  respectively injected in  $WG_2$  for corresponding duplexers. The vertical line corresponds to the  $T_o$  at target wavelengths.

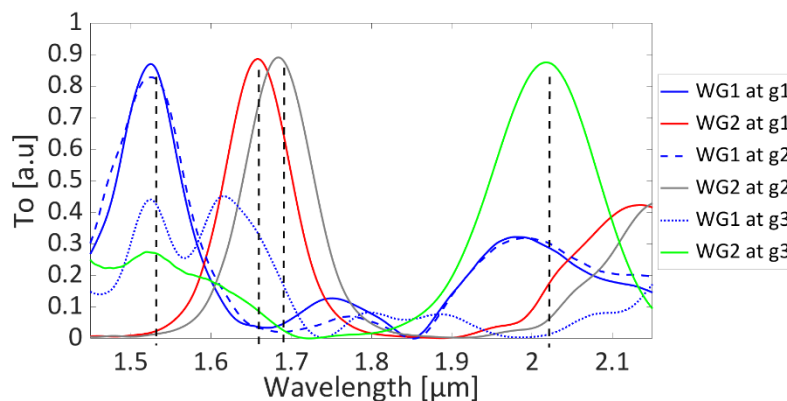


Figure 2.12: Range of wavelength launched at Port A and Port B of the angled MMI.

### 2.3.3 Optical Characterization and Experimental Results

The angled multimode interference duplexers, discussed in the previous section, have been fabricated using EBL and dry etching, discussed in section 1.2. To optimize the fabrication process and transmission capabilities, various device configurations were utilized. The details of the fabricated angled MMI duplexer samples can be seen in Figure 2.13.

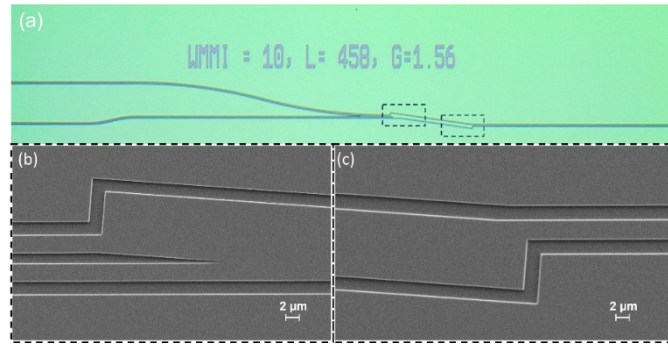


Figure 2.13: Fabricated angled MMI duplexer sample under (a) microscopic imaging. SEM image (zoom) (b) between input and multimode waveguide (c) between multimode waveguide and output.

The fabricated sample (multiplexer) underwent optical characterization using an end-fire measurement setup, explained in section 1.3. Each device port was optically measured separately. The aligned process for the optical characterization is performed using a single wavelength laser for  $WG_1$  (1530 nm) and a TLS for  $WG_2$  (1653.7 nm) - a Yenista Optics TLS and an Eblana laser diode respectively. After the alignment process, the TLS was replaced with an Amonics ALS broadband light source and single wavelength laser - with an Amonics ASLD super luminescent source. The output spectrum is collected into a Thorlabs power meter and an OSA from Yenista Optics.

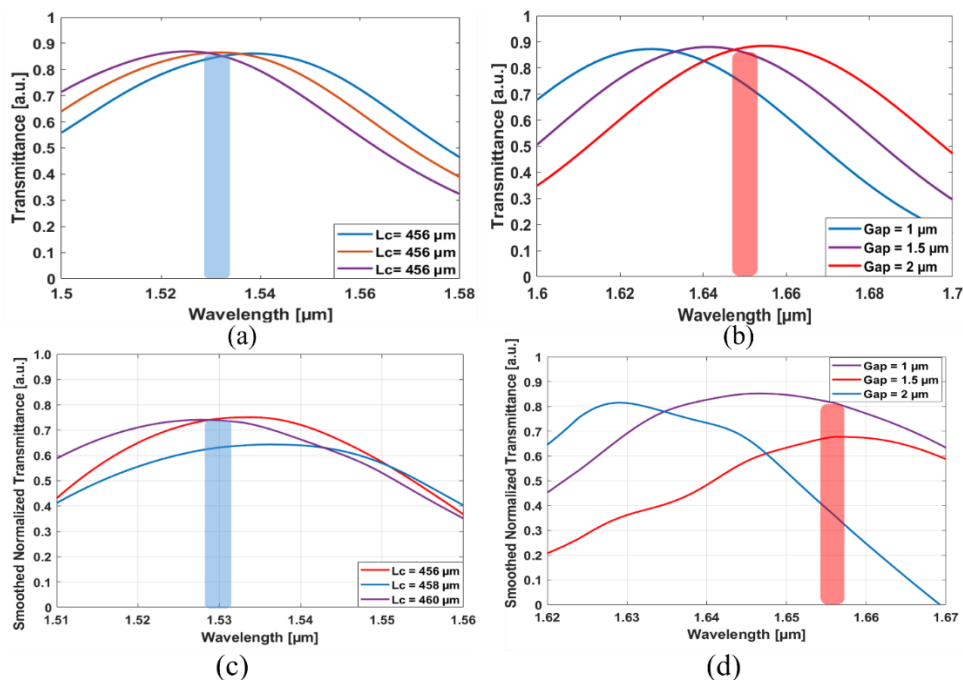


Figure 2.14: Numerical results for a range of wavelength excited at (a)  $WG_1$  for varying  $L_c$  and (b)  $WG_2$  for varying  $g$ . Smoothed normalized transmittance characterization results for a range of wavelength excited at (c)  $WG_1$  for varying  $L_c$  and (d)  $WG_2$  for varying  $g$ .

Figure 2.14 presents the simulation and characterization results of the angled MMI coupler for varying gaps between the  $L_c$  while launching at input port  $WG_1$ , as well as the gap effects when launching at  $WG_2$ . The characterization results are represented as the normalized transmission spectra of the angled MMI duplexer device, relative to a straight waveguide with a width of  $3\ \mu\text{m}$  and a height of  $300\ \text{nm}$ , matching the dimensions of the input waveguide of the duplexer. The spectra cover a broad range of wavelengths, with vertical boxes marking the target wavelengths  $\lambda_{NH_3}$  and  $\lambda_{CH_4}$ .

From the simulation results, a  $2\ \mu\text{m}$  increase in  $L_c$  causes a blue shift in the spectrum by  $8\ \text{nm}$  for the wavelength excited at  $WG_1$ . Similarly, for a gap increment of  $0.5\ \mu\text{m}$ , the spectrum shifts by  $14\ \text{nm}$ . This trend is consistently observed in the characterization results. The results demonstrate a favorable trade-off in coupling efficiency (CE) concerning variations in the geometric parameters  $L_c$  and  $g$ . The agreement between simulation and characterization results is strong. The device with a  $L_c$  of  $458\ \mu\text{m}$  and a  $g$  value of  $1.5\ \mu\text{m}$  exhibits the best performance, achieving CE values of  $74\%$  and  $80\%$  for wavelengths of  $1530\ \text{nm}$  and  $1654\ \text{nm}$ , respectively.

The wider spectrum exhibits normalization noise, attributed to the critical and fundamental alignment required in the end-fire method and the precision of the sample's facet cleaving. For further clarity in the transmittance, in Figure 2.15, the transmission spectra, obtained using a broadband ASE laser, are normalized relative to the source, covering a wide range of wavelengths. The vertical line in the figures indicates the target wavelengths  $\lambda_{NH_3}$  and  $\lambda_{CH_4}$ . This normalization process facilitates accurate and meaningful comparisons across different samples and experimental conditions.

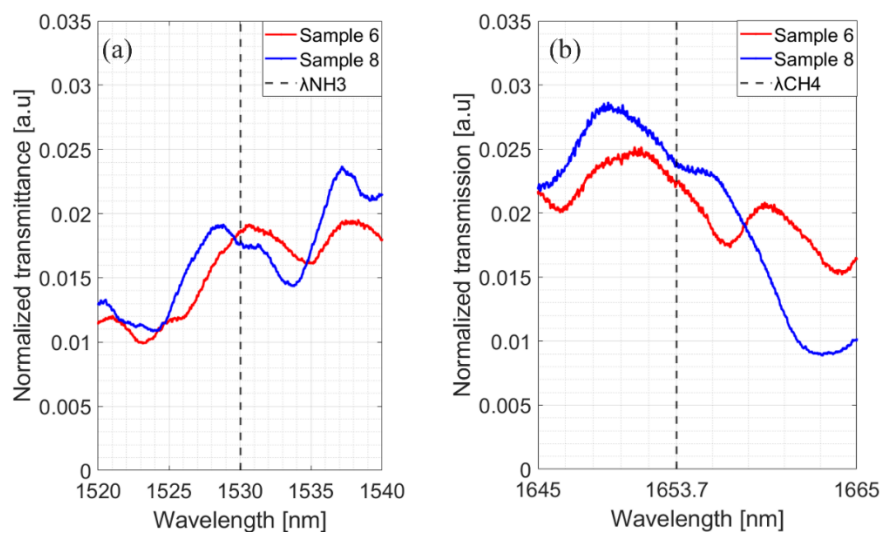


Figure 2.15: Experimental results for launching a range wavelength (a) at  $WG_1$  (b) at  $WG_2$ .

As well Table 2.3, shows CE normalized with respect to the straight waveguides. Considering the FOM in CE, Sample 6 and Sample 8 emerge as the most promising, exhibiting CE values of 74%: 80%, and 59.5%: 71.5%, respectively. The characterizations result of these selected samples is shown in Figure 2.15 (a) and (b). Sample 6 adopted the same device configuration as the optimized angled MMI duplexer designed with a  $L_c$  value of 458  $\mu\text{m}$  and  $g = 1.56 \mu\text{m}$  while Sample 8 has a  $L_c$  value of 460  $\mu\text{m}$  and  $g = 1 \mu\text{m}$  (see Table 2.3). These characterizations of the fabricated angled MMI device prove its consistent performance and selectivity. These findings indicate that the designed device exhibits an optimal performance within a spectral range of approximately 10 nm centered around these specific wavelengths.

**Table 2. 3: The normalized transmittance of the duplexer configurations.**

Sample	$L_c$ [ $\mu\text{m}$ ]	$g$ [ $\mu\text{m}$ ]	CE at $\lambda_{\text{NH}_3}$ [%]	CE at $\lambda_{\text{CH}_4}$ [%]
1		1	58	66.5
2	456	1.5	61	62
3		2	60	39.2
4		1	54.4	70
5	458	1.5	63	57
6		1.56	74	80
7		2	60	40
8		1	59.5	71.5
9	460	1.5	53.5	55
10		2	75.8	52.6

A series of devices fabricated for varying parameters of  $g$  and  $L_c$ , exhibiting a favorable trade-off in CE. Notably, these results demonstrate a satisfactory agreement with the corresponding simulations. A duplexer at 1530 nm and 1684 nm was also tested. The 1684nm wavelength is at the limit of that provided by the super luminescent diode and the signal to noise ratio was low and the estimated transmission is 63% and 32% for samples 6, respectively. The CE and the ability to achieve precise trade-offs in geometric parameters offer promising prospects for enhancing performance and adaptability. This can be utilized for customized applications in multi-gas sensing and telecommunication fields, serving as an ideal beam combiner.

## 2.4 Highly Efficient and Selective DC Duplexer

The design and fabrication of a compact, low-loss, broadband DC based duplexer operating in the near-infrared (NIR) region are demonstrated. DCs are commonly used as important passive optical devices in integrated silicon photonics devices such as power splitters, mirroring resonators, and Mach-Zehnder interferometers. The DC stands out as particularly promising due to advantages, such as a compact device footprint, high reliability, and the potential low loss coupling. Additionally, DC offers numerous benefits, including low fabrication tolerance, minimal insertion loss, the capacity to handle multiple channels, and compatibility with other multiplexing devices. A wavelength-independent directional coupler (WIDC) fabricated on a silicon-on-insulator (SOI) platform with a 220 nm device exhibited a 3-dB coupling length of approximately 5  $\mu\text{m}$  over a wavelength range of 1525 nm to 1625 nm. This WIDC design was successfully implemented in various applications, including power splitters, Mach-Zehnder interferometers, and all-pass micro ring resonators [53]. Another study demonstrated a broadband DC specifically designed for signal power tapping on a 3  $\mu\text{m}$  SOI platform. This device, operating in the wavelength range of 1470 nm to 1630 nm, achieved a CE ratio of 94% for 1550 nm into the primary waveguide and 4 % at through port (serves for monitoring purposes) [62]. The design incorporated an arc-shaped waveguide in the coupling region to enhance spectral stability and minimize transmission losses.

Researchers also explored broadband curved DCs on SOI platforms with silicon layer thicknesses of 220 nm. By combining curved and straight waveguide sections, these couplers achieved a  $\pm 1$  dB bandwidth of 88 nm centered at 1565 nm. Further, broadband operation, an ultra-broadband 2 x 2 adiabatic 3 dB coupler was realized using subwavelength-grating-assisted strip waveguides on an SOI platform. This coupler exhibited even power splitting with an imbalance of less than 0.3 dB and average excess losses below 0.11 dB over a measured wavelength range of 185 nm, limited by the available tunable laser [63]. A design employed a Mach-Zehnder directional coupler (MZDC) configuration with carefully engineered curved structures in the coupled regions to minimize polarization dependence and achieve a flattened wavelength response [64], [65]. Tapered, asymmetrical, or curved DCs can allow a mild reduction in device footprint, but at the price of a lower manufacturing error tolerance, high modal dispersion due to phase mismatch, or low coupling efficiency [66], [67], [68]. Table 2.4 displays the performance comparison with wavelength multiplexers previously reported.

**Table 2. 4: Performance comparison with previously reported wavelength multiplexers.**

Ref	Structure	Wavelength [nm]	Method	Insertion loss [dB]
[69]	DC	1310 - 1550	Simulation	0.27 and 0.08
[70]	MMI	1550 - 2000	Experimental	0.14 and 1.2
[71]	SWG DC	1550 - 2000	Simulation	0.14 and 0.80
[72]	TMI	1310 - 1550	Experimental	1
[51]	SWG MMI	1310 - 1550	Simulation	<0.24
[73]	SWG MMI	1310 - 1550	Simulation	0.09 dB and 0.08 dB
[74]	ADC	1310 - 1490 - 1550	Experimental	0.98 dB, 0.69 dB and 0.76 dB

### 2.4.1 Evanescent Field Coupling

The interaction of evanescent fields between closely spaced waveguides is a fundamental concept in integrated photonics, enabling the development of various optical components like DCs, filters, and modulators. The theory behind this interaction hinges on the understanding of electromagnetic waves, waveguides, and the nature of evanescent fields. An evanescent field is a spatially decaying electromagnetic field that exists outside the core region of a waveguide [61]. When a guided mode propagates within a waveguide, a portion of its energy is confined to the core, while another portion extends beyond the core in the form of an evanescent field. This field decays exponentially with distance from the core.

The extent of the overlap is quantified by an overlap integral, which calculates the fraction of the incident field. Coupled Mode Theory (CMT) provides a mathematical framework to analyze the interaction between modes in coupled waveguides [75]. CMT assumes that the individual waveguide mode profiles remain relatively unchanged in the presence of each other. This simplification allows us to describe the evolution of the mode amplitudes using a set of coupled first-order differential equations. For identical, phase-matched waveguides, two distinct super modes emerge, the symmetric super mode (fundamental mode of coupled waveguide) has a higher effective index compared to the individual waveguides. The antisymmetric super mode (the first mode of coupled waveguide), this mode has a lower effective index compared to the individual waveguides. The difference in propagation constants between the symmetric and antisymmetric super modes gives rise to modal dispersion.

This dispersion causes the coupled signal to spread out as it propagates, impacting the performance of devices. Figure 2.16 illustrates two single-mode waveguides with field amplitudes,  $E_1(x, y, z)$  and  $E_2(x, y, z)$ , propagating along the y-direction with propagation constants  $\beta_1$  and  $\beta_2$ . For efficient power transfer, the two interacting modes must have the same propagation constant, i.e. the phase matching condition given by:

$$\beta_1 = \beta_2 = \frac{2\pi n_{eff}}{\lambda} \quad (2.6)$$

$$n_{eff} = n_{eff1} = n_{eff2} \quad (2.7)$$

This ensures that the waves remain in phase as they propagate, allowing for constructive interference and sustained energy transfer. When the gap ( $g$ ) is small enough for the evanescent tails of the guided modes to overlap. Thus, the system supports two lowest-order super-modes (symmetric and antisymmetric), are shown in Figure 2.16 (b) and (c). These super modes arise as linear combinations of the uncoupled waveguide modes, having a propagation constant.

$$\beta_a = \frac{2\pi n_{eff}^s}{\lambda} \quad (2.8)$$

$$\beta_{as} = \frac{2\pi n_{eff}^{as}}{\lambda} \quad (2.9)$$

Since  $n_{eff}^s > n_{eff}^{as}$ , both modes travel different velocities, hence their relative phase difference is  $\varphi = (\beta_{as} - \beta_a) y$ , which defines the fraction of power coupled from one waveguide to another evanescently at a distance of  $z$ . If the coupling coefficient ( $\kappa$ ) is known,

$$\text{Ie, } \beta_a = \beta_o + k \quad \text{and} \quad \beta_{as} = \beta_o - k \quad (2.10)$$

$$\text{Thus, } \beta_{as} - \beta_a = 2k = \frac{2\pi(n_{eff}^s - n_{eff}^{as})}{\lambda} \quad (2.11)$$

$$\text{Ie, } L_c = \frac{\pi}{2k} = \frac{\lambda}{2(n_{eff}^s - n_{eff}^{as})} \quad (2.12)$$

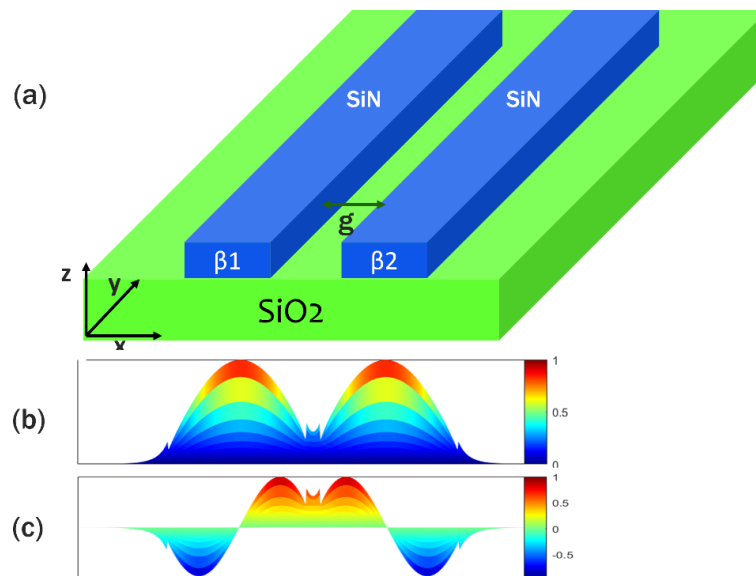


Figure 2.16: (a) Schematic of closely spaced coupled waveguide system. (b) Symmetric Super mode (fundamental mode of coupled waveguide) (c) antisymmetric Super mode (first mode of coupled waveguide).

For example, the calculated effective index of symmetric and anti-symmetric modes of waveguide based on  $\text{Si}_3\text{N}_4$ , having a thickness of 300 nm and 3  $\mu\text{m}$  width of waveguide on  $\text{SiO}_2$  platform of 2.2  $\mu\text{m}$ , at  $\lambda = 1530$  nm is  $n_{eff}^s = 1.6469$  and  $n_{eff}^{as} = 1.6448$ . The calculated

coupling length ( $L_c$ ) at which the power completely transfers to others for different wavelengths is depicted in Table 2.5. Further, the gap between the waveguides has a major role, as this parameter determines the effective index of the coupled system.

Table 2. 5: Coupling length corresponding to the wavelength for 3  $\mu\text{m}$  x 300 nm phase-matching coupled waveguides.

Wavelength ( $\lambda$ ) [nm]	Lc [ $\mu\text{m}$ ]
1530	360
1653.7	272
2003	132

## 2.4.2 Proposed Structure and Numerical Results

This section of the research focuses on the design and fabrication of a low-loss, broadband  $2 \times 1$  DC -based duplexer and explores its design flexibility and CE. The device is focused on effectively combining distinct wavelengths, namely  $\lambda_{NH_3}$  at Port A and  $\lambda_{CH_4}$  at Port B. The choice of wavelengths is selected due to their suitability for multi-gas detection of ammonia and methane, which exhibit distinctive optical absorption characteristics in the wavelengths covered by diode lasers. Figure 2.17 presents a schematic diagram of the DC -based duplexer design. The S-bend waveguide is used to guide  $\lambda_{NH_3}$ , as shorter wavelengths experience the least bend loss while a straight waveguide is employed for guiding  $\lambda_{CH_4}$ , where the optical power available is typically lower. The parameter " $L_{dc}$ " represents the coupling length, which denotes the distance along which two waveguides interact or couple with each other, and " $g$ " represents the distance between the waveguides, indicating the spatial interval between them. The input waveguide ports are positioned  $D = 100 \mu\text{m}$  apart, and the bend radius in the design is set to  $R_{arc} = 5000 \mu\text{m}$ , with an angle  $\alpha = 8.1$  degrees. This configuration ensures efficient space for integrating the micro on-chip lasers and lower bend loss light propagation.

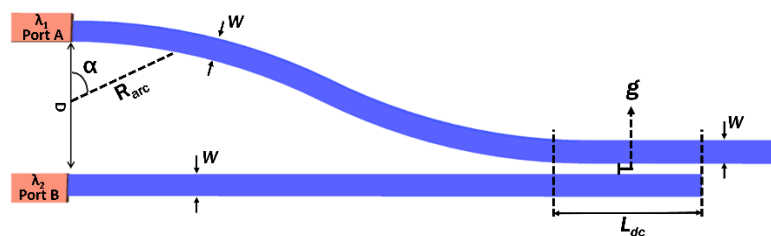


Figure 2.17: Schematic diagram of design parameters of DC based wavelength duplexer. Port A refers to the bent waveguide (top) and Port B refers to the straight waveguide (bottom).

The simulations were performed using the Beam PROP simulation tool from RSoft. This platform is commonly used for parameterizing and estimating the optimum results using the FD-BPM. The computational mesh grid resolution of the simulation domain was optimized

along the three spatial axes of  $X = 100$  nm,  $Y = 100$  nm, and  $Z = 50$  nm. The coupler's input waveguide ( $W$ ) dimension has been meticulously optimized to maximize the transmittance with the intended lasers' mode profiles.

The relation between the coupling length and optical transmittance was found using coupled mode theory if the mode of each waveguide in the absence of the other remains approximately the same and that coupling modifies the amplitude of these modes without affecting their transverse spatial distribution and their propagation constant ( $\beta$ ) [75], [76]. Here the waveguides are identical, and the phase mismatch  $\Delta\beta_{\lambda_1} = \Delta\beta_{\lambda_2} = 0$ . The length of evanescent mode coupling can be estimated as follows:

$$L_c = \frac{\pi}{2K} (2n + 1) \quad (2.13)$$

where  $L_c$  is the coupling length, at a distance the power is completely coupled to the other waveguide,  $\lambda$  is the wavelength of light in vacuum,  $K$  is the coupling coefficient, and  $n$  ( $= 0, 1, 2, \dots$ ) is the number of beat length. The coupling coefficient depends on the gap between the waveguides and the  $n_{eff}$  of the waveguide. The power coupled in each waveguide as a function of propagation distance is given by:

$$P_{a,a} = P_a(0) \cos^2\left(\frac{\pi z}{2 L_{dc}}\right) \quad (2.14)$$

and

$$P_{a,b} = P_b(0) \sin^2\left(\frac{\pi z}{2 L_{dc}}\right) \quad (2.15)$$

where  $P_{a,a}$  represents the power at Port A, when power is launched at port A, and similarly,  $P_{a,b}$  represents the power at Port A, when power is launched at Port B, for respective  $L_{dc}$ . The calculated coupling coefficient for wavelength equal to  $\lambda_{NH_3}$  and  $\lambda_{CH_4}$  nm are  $K_a = 4.245 \times 10^{-3}$  and  $K_b = 5.817 \times 10^{-3}$  [77].  $P_a(0)$  and  $P_b(0)$  are the input power, on considering normalized output power, the  $P_a(0) = P_b(0) = 1$ .

A constant  $L_{dc}$  is computed for both wavelengths  $\lambda_{NH_3}$  and  $\lambda_{CH_4}$  launching at respective waveguides. The optical output power transmittance with respect to the gap between the waveguides and  $L_{dc}$  is depicted in Figure 2.18 (a) and (b), respectively. The design is very sensitive to the value of the gap, with changes on the order of a few tens of nanometers significantly impacting the transmittance. On the other hand, the  $L_{dc}$  shows a relatively flat response to transmittance variations in the range of tens of microns. From Figure 2.18 (a) and (b), the device achieves its

highest CE at  $g$  values of  $0.15 \mu\text{m}$  and  $0.3 \mu\text{m}$ . Considering the limitations posed by the fabrication process, a  $g$  value of  $0.3 \mu\text{m}$  is deemed most suitable. In addition, a  $L_{dc}$  equal to  $810 \mu\text{m}$  is selected for the coupler.

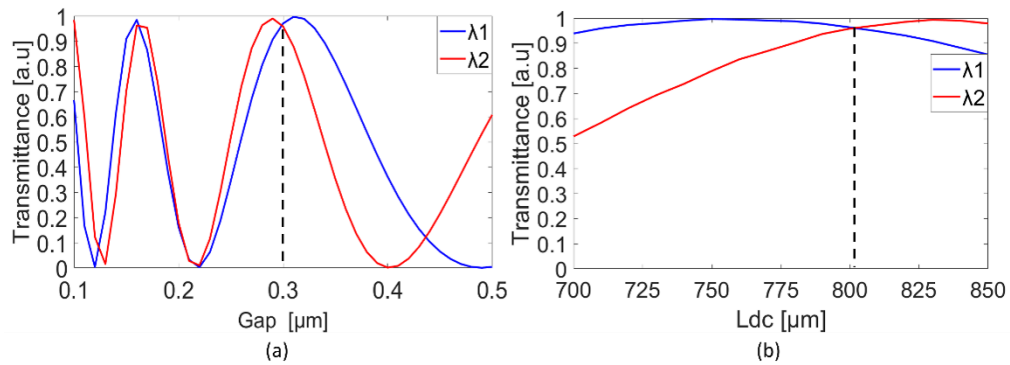


Figure 2.18: Transmittance of wavelength launched at Port A and Port B (a) with respect to the gap between the input waveguides and (b) with respect to changing length of port B.

While considering the complete duplexer device, the device introduces evanescent mode coupling due to the bend structure, resulting in a reduced  $L_{dc}$  equal to  $740 \mu\text{m}$ . With these optimized parameters, the design of the duplexer exhibits optical output power transmittance of 96% for both wavelengths  $\lambda_{NH_3}$  and  $\lambda_{CH_4}$ . These results underscore the excellent performance of the duplexer in efficiently transmitting optical power at the specified wavelengths. The electric field profile of the propagating light in the DC is depicted in Figure 2.19 (a) and (b). In this configuration, the corresponding fundamental mode profile is injected at the respective input ports for  $\lambda_{NH_3}$  and  $\lambda_{CH_4}$ . The resulting power is coupled to a single output waveguide, which is an extension of Port A.

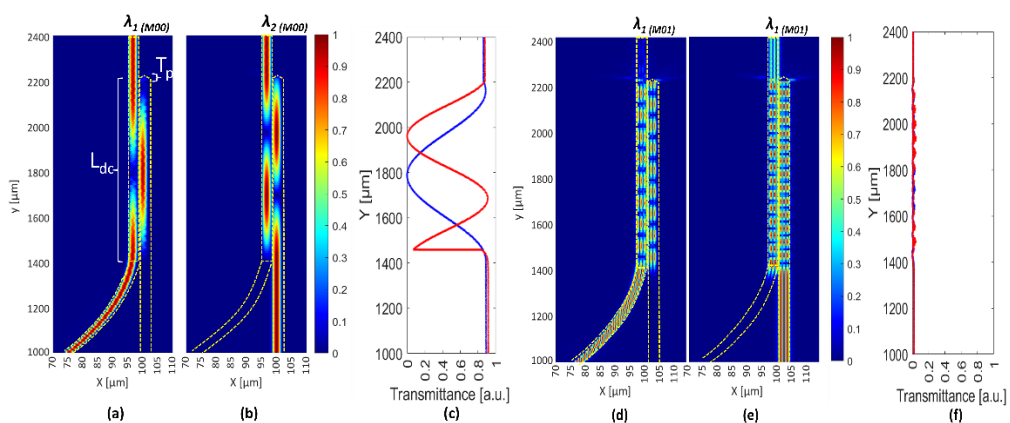


Figure 2.19: The electric field distributions of the DC coupler, when (a, d) Port A at  $1530 \text{ nm}$  and (b, e) Port B at  $1653.7 \text{ nm}$  are excited with the sole (a, b) fundamental mode or with the sole (d, e) higher-order mode. (c, d) Transmittance fraction of the (c) sole fundamental mode and of the (f) sole higher order mode as a function of the  $y$ -coordinate, when the two ports are separately excited by launching the laser mode profile.

Higher-order modes can significantly impact waveguide transmittance by causing modal interference, and crosstalk [44]. To account for the distribution of modes within the waveguide, both behaviors of fundamental mode and of higher order mode are investigated. In Figure 2.19, the field distribution of both the fundamental mode and higher order mode launched at respective input ports are shown. Figure 2.19 (c) illustrates the transmittance due to the sole fundamental mode launching the laser mode profile, showing transmittance values of 86% at 1530 nm and 87% at 1653.7 nm. Similarly, Figure 2.19 (d) and (e) pertain to higher order modes launched at their respective ports, while Figure 2.19 (f) represents the transmittance of the sole higher order modes when launching the laser mode profile. Notably, the transmittance of higher order modes is 0.1% and 0.15% for wavelengths of 1530 nm and 1653.7 nm, respectively.

The total transmittance ( $T_o$ ) achieved by effective tapering at the terminal point of Port B is considered. The waveguide tapering is implemented to minimize back reflections, particularly at the  $\text{Si}_3\text{N}_4$ – $\text{SiO}_2$  interface at the end of each waveguide. Additionally, this tapering helps canceling higher-order modes, as demonstrated in Ref. [78], [79], [80], [81]. The level of reflection depends on the trench width and tapering length, with the schematic parameters shown in Figure 2.20 (a). In the design, a fixed trench width of 2  $\mu\text{m}$  while varying the tapering length is used. Figure 2.20 (b) illustrates the FDTD simulation performed using RSoft FullWAVE, which shows that a tapering length ( $t_p$ ) of 10  $\mu\text{m}$  significantly reduces reflections. Increasing the tapering length beyond 10  $\mu\text{m}$  may lead to coupling losses in the duplexer and triplexer, depending on the design. This reflection can be further minimized by increasing trench width.

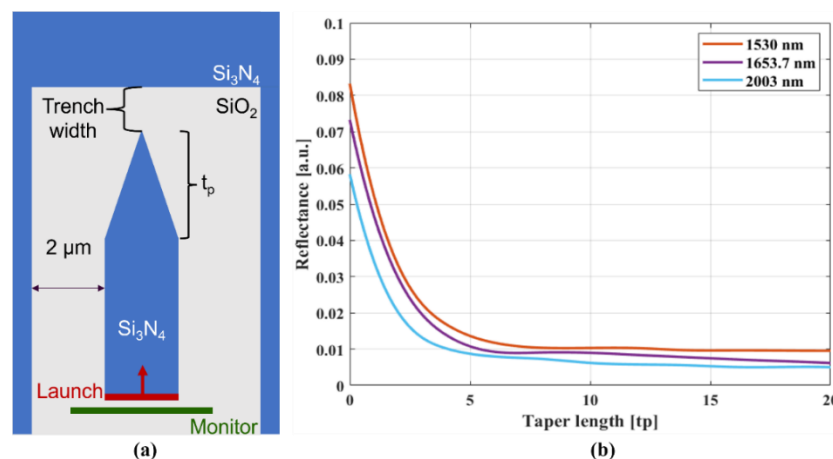


Figure 2.20: Schematic of the waveguide tapering at the  $\text{Si}_3\text{N}_4$ – $\text{SiO}_2$  interface. (b) FDTD simulation results showing the reflectance of light at the monitor for various wavelengths.

The tapering length ( $T_p$ ) is optimized to 10  $\mu\text{m}$ , considering the overall  $T_o$  of  $\lambda_{\text{NH}_3}$  and  $\lambda_{\text{CH}_4}$  using the laser mode profile, and with higher-order modes. Minimizing the effect of higher-order modes can lead to a higher signal-to-noise ratio in spectroscopic systems, showcasing the

design's efficiency in transmitting optical power for specified wavelengths. Furthermore, the waveguide tapering also serves the purpose of reducing reflections from propagating back to the input source when interacting with slab SiO<sub>2</sub> waveguides.

The transmittance characteristics for a wavelength range of 1450 nm to 1750 nm launched at Port A (blue lines) and Port B (red lines) are presented in Figure 2.21. Also, the designed duplexer exhibits an optimal performance within the spectral range of 50 nm centered around the target wavelength (dashed vertical lines).

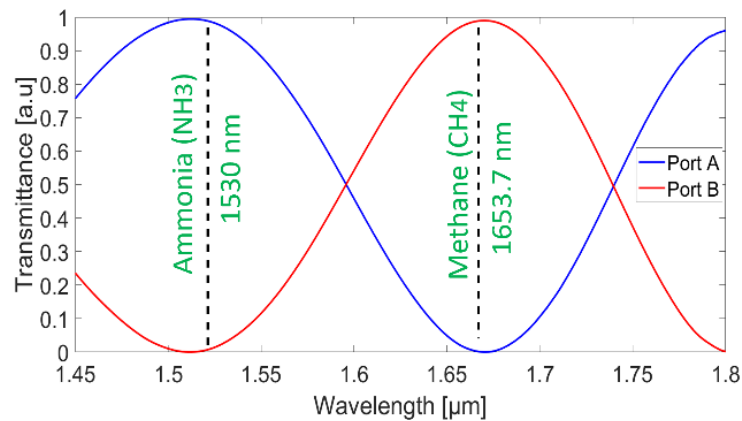


Figure 2.21: Range of wavelength launched at Port A and Port B.

When considering launching into the designed duplexer device using realistic diode laser mode profiles at wavelengths  $\lambda_{NH_3}$  and  $\lambda_{CH_4}$ , the transmittance is equal to 78% and 81%, respectively. The dimension of the waveguide is unchanged throughout the propagation and coupling of the device, which helps to preserve the purity of the guiding mode and modal dispersion effects. Higher-order modes can have a significant impact on waveguide transmission, as they can cause mode dispersion, modal interference, and crosstalk [44]. This effect can lead to a lower signal-to-noise ratio of spectroscopic systems. Additionally, launching higher-order modes exhibit transmittance values of 91% and 14%, respectively. These results demonstrate the effectiveness of the design in efficiently transmitting optical power for the specified wavelengths, considering the desired laser mode profiles as well as the negative impact of higher-order modes.

### 2.4.3 Optical Characterization and Experimental Results

DC-based duplexers, discussed in the previous section, have been fabricated. To optimize fabrication tolerance and transmission, various device configurations are employed using the standard method EBL [25], [82]. Figure 2.22 shows the details of fabricated DC duplexer samples. The tapered tips of the waveguide corresponding to Port B are employed to reduce any kind of reflections that could de-stabilize the laser.

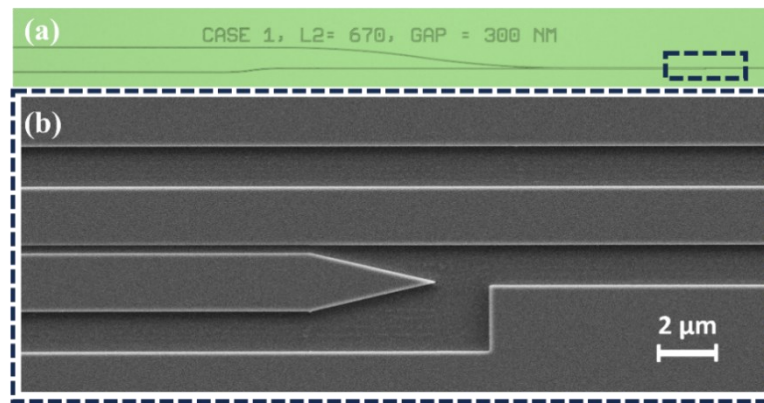


Figure 2.22: (a) Microscopic image of fabricated duplexer. (b) Details SEM imaging showing the tapered tip of the waveguide (dashed rectangle box in zoom).

The optical characterization of the fabricated sample was performed using an end-fire measurement set up, similar to the setup shown [82]. The aligned process for the optical characterization is performed using a single wavelength laser for Port A (1530 nm) and a TLS for Port B (1653.7 nm) - a Yenista Optics TLS and an Eblana laser diode respectively. After the alignment process, the TLS was replaced with an Amonics ALS broadband light source and single wavelength laser - with an Amonics ASLD super luminescent source. The output spectrum is collected into a Thorlabs power meter and an OSA from Yenista Optics.

The wider spectrum exhibits normalization noise, attributed to the critical alignment required in the end-fire method and the precision of the sample's facet cleaving. The measurement results of the best devices are shown in Figure 2.23. The obtained transmission spectrum is normalized relative to a broadband ASE source spectrum. The vertical line in the figures indicates the target wavelengths. This normalization process facilitates accurate and meaningful comparisons across different samples and experimental conditions, as well as enables correlations with straight waveguides. These findings indicate that the designed device exhibits an optimal performance within a spectral range of approximately 10 nm centered around these specific wavelengths. The on-chip transmission through the duplexer is determined by a correlation with straight waveguides, giving the efficiencies listed in Table 2.6.

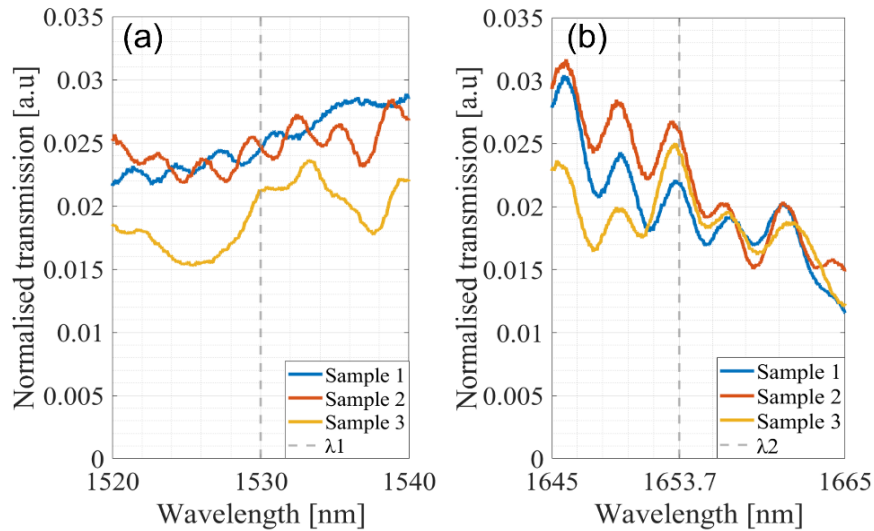


Figure 2.23: Experimental results for launching a range wavelength at waveguide corresponds to (a)  $\lambda_{NH_3}$  and (b)  $\lambda_{CH_4}$ .

The presented characterization results of the fabricated DC device prove its consistent performance and reliability. The highest CE equal to 73 % and 77 % is achieved for sample 2, having design configuration  $L_{dc} = 670 \mu\text{m}$  and  $g = 300 \text{ nm}$ .

**Table 2. 6: The coupling efficiency of the duplexer configurations.**

Sample	$L_{dc}$ [ $\mu\text{m}$ ]	$g$ [nm]	CE at $\lambda_{NH_3}$ [%]	CE at $\lambda_{CH_4}$ [%]
1	670	250	72.5	64.6
2	670	300	73	77
3	770	150	71.8	62

The initially presented results were based on a fabrication process from the silicon fab at the Tyndall National Institute. Subsequently, an optimized fabrication process was implemented using silicon nitride wafers purchased from LIONIX International BV, leading to improved results and parameters as detailed below. The design is modified to include a  $300 \mu\text{m}$  spacing between the input waveguides to accommodate laser integration. The output spectrum of the duplexer, along with the simulation results for varying  $L_{dc}$  at Port A, is illustrated in the Figure 2.24, at a constant gap =  $275 \text{ nm}$ . The duplexer spectrum is presented while excited by the broadband source at Port A is normalized to blank waveguides. Blank waveguides refer to waveguides with an S-bend that mimic the same dimensions as the duplexer input waveguides. The spectra exhibit a blue shift, where a change in  $L_{dc}$  corresponds to a  $30 \text{ nm}$  shift for every  $20 \mu\text{m}$  increase in length.

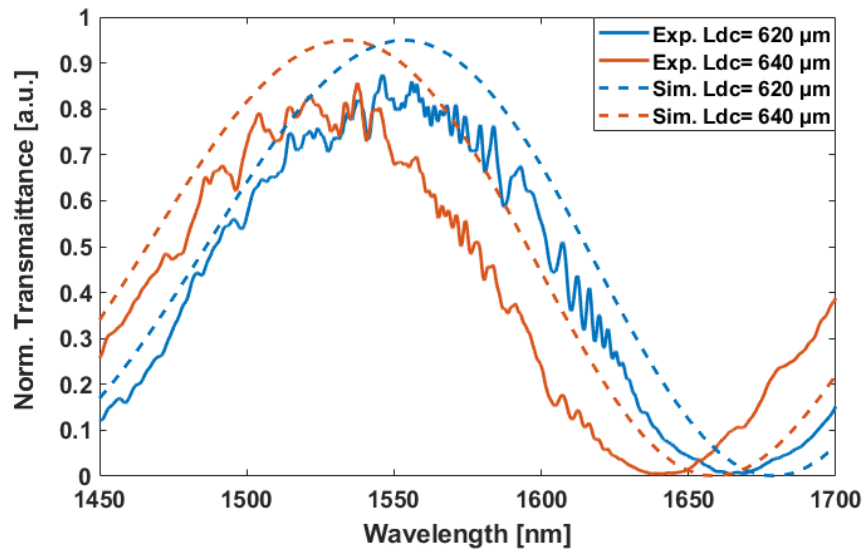


Figure 2.24: Normalized transmittance spectra of the DC duplexer for wavelengths released at Port 1 for varying  $L_{dc}$ .

The combined spectrum for the optimized device at both Port A and Port B is presented in Figure 2.25 for both simulation and characterization. The target wavelengths are marked with blue and red vertical boxes.

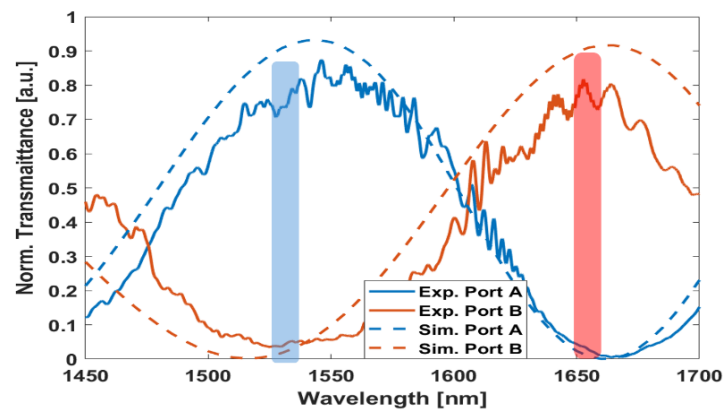


Figure 2.25: Combined spectrum of the optimized device at Port A and Port B, shown for both simulation and characterization.

The optimized parameter for designing the duplexer is  $L_{dc} = 640 \mu\text{m}$  (including  $20 \mu\text{m}$  tapered region) with a gap of  $275 \text{ nm}$ . This duplexer configuration reached an improved CE of  $85 \%$  and  $88 \%$  for wavelength  $\lambda_{NH_3}$  and  $\lambda_{CHA}$ , respectively. Diode laser integration on the chip will be discussed further in the Future Work section. These results pave as a crucial optical component in on-chip devices, functioning as low loss combiner with a lower footprint of  $2000 \times 300 \mu\text{m}$ , attributing various applications such as in PICs and as a scalable input for multi-gas detection devices. The integration of these devices attracts appeal to the compact, real-time and portable sensors.

## 2.5 Cascaded DC-based Triplexer

### 2.5.1 Proposed Structure and Numerical Results

This section presents experimental and simulation results of a novel high-performance cascaded DC based triplexer. The duplexers were designed to coupled  $\lambda_{NH_3}$  and  $\lambda_{CH_4}$ , where triplexer device is designed to add the third wavelength 2003 nm corresponding to carbon dioxide ( $\lambda_{CO_2}$ ). The triplexer's functions focus on enhancing the coupling efficiency (CE) and selectivity while facilitating room for the on-chip integration of diode lasers. The structures are designed using a 300 nm thick  $Si_3N_4$  layer on an 8  $\mu m$  buried oxide (BOX) platform with a 1  $\mu m$  thick ( $SiO_2$ ) upper cladding layer. Figure 2.26 (a) shows a schematic diagram of the triplexer design, outlining the arrangement of the positioning of the diode lasers, S-bends, the coupling region, and the output waveguide with a width of  $W_o$ . The triplexer configurations are introduced by considering CE and bending loss. As the wavelength becomes longer, the loss due to bending diminishes [35]. The bend radius in the design is set to  $R_{arc} = 5000 \mu m$ , with an angle  $\alpha = 14^\circ$ , ensuring sufficient space for integration of the micro-on-chip lasers and lower bend loss light propagation. The input and output waveguides have a width of  $W = W_o = 3 \mu m$ , maintained across the S-bend, coupling section, and output waveguide. The coupling lengths  $L_{c1}$ ,  $L_{c31}$ , and  $L_{1-3}$  are defined at the coupling region, where the gap between all the waveguides is constant and denoted as  $g$ .

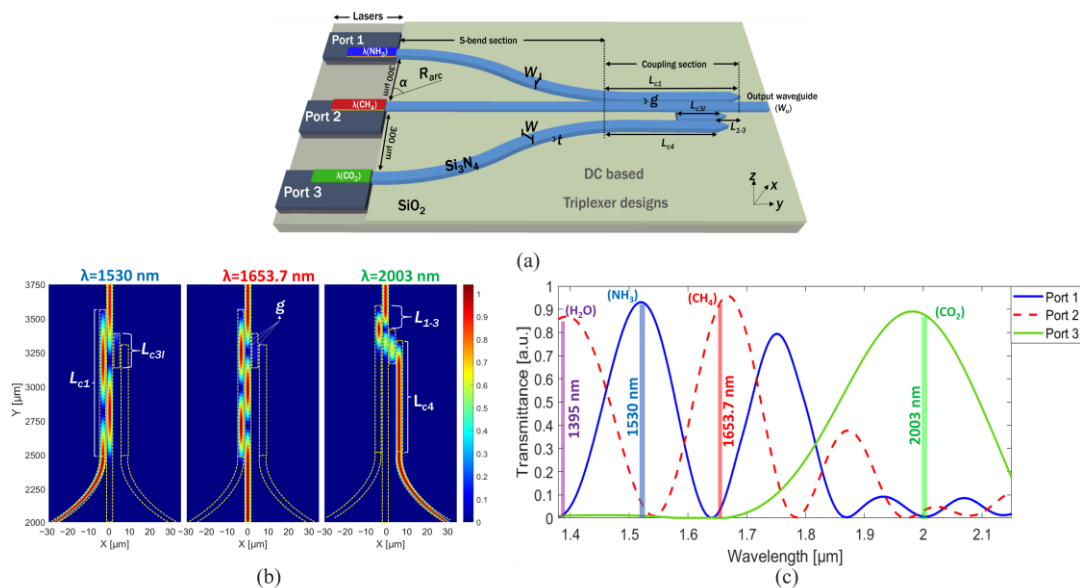


Figure 2.26: (a) Schematic diagram of design parameters of DC-based wavelength triplexer. (b) The electric field distributions of the optimized triplexer configurations. (c) The range of wavelength emitted at  $W_o$  while injecting the source at Ports 1, 2, and 3.

The triplexer design was performed using the 3D FD-BPM [36,37]. The computational mesh grid resolution of the simulation domain was optimized along the three spatial axes of  $X = 100$  nm,  $Y = 100$  nm, and  $Z = 50$  nm. The dispersion formula was used to determine the refractive indices of  $\text{Si}_3\text{N}_4$  and  $\text{SiO}_2$  [38,39]. The tapering of the end of the waveguide is introduced for two reasons: firstly, to avoid potential excitation of higher-order modes, and secondly, to prevent the reflection of light back to the source due to the  $\text{Si}_3\text{N}_4$ - $\text{SiO}_2$  interface at the end of each waveguide. This reflection can lead to undesirable losses and impacts on the overall performance of the triplexer system [40]. The tapering length was optimized to  $t_p = 10$   $\mu\text{m}$ , which reduces the reflection to 1%. The design for Port 1 is modeled to guide the wavelength  $\lambda_{\text{NH}_3}$ , with Port 2 serving as the pathway for the wavelength  $\lambda_{\text{CH}_4}$ . The electric field profile of each wavelength at the respective ports is depicted in Figure 2.26 (b). Figure 2.26 (c) shows the transmittance spectra for the optimized triplexer, with distinct peaks Port 1 and Port 2, while also giving a broad spectral range via Port 3. Port 1 exhibits a primary peak at 1530 nm, followed by a transmittance peak at 1750 nm. Similarly, Port 2 has a primary transmittance peak at 1670 nm and another 82% transmittance peak at 1395 nm, which aligns with the water vapor ( $\text{H}_2\text{O}$ ) absorption line. The bandwidth and free spectral range are both measured at 100 nm for Port 1 and Port 2. The device achieves a maximum transmittance of 90%, 91%, and 88% for wavelengths  $\lambda_{\text{NH}_3}$ ,  $\lambda_{\text{CH}_4}$ , and  $\lambda_{\text{CO}_2}$ , respectively.

A 300 nm thick layer of  $\text{Si}_3\text{N}_4$  on an 8  $\mu\text{m}$  BOX on a Bulk silicon wafer was purchased from LIONIX International BV. The device was patterned using the processes of EBL and dry etching, involving several steps (the detailed fabrication process is discussed in section 1.2). The fabrication process exhibits a tolerance of  $\pm 25$  nm of the gap ( $g$ ) from the designed mask file to the final sample. In this study, the actual sample dimensions after fabrication used as experimental parameters. Following inspection with a scanning electron microscope (SEM), a 1  $\mu\text{m}$  thick  $\text{SiO}_2$  layer was deposited using PECVD [83]. Various configurations of the device were investigated and implemented to enhance both the fabrication process and transmission performance. The fabrication specifics of the triplexer samples are illustrated in Figure 2.27, which includes details of the fabricated DC triplexer, featuring a tapered tip of the waveguide corresponding to  $L_{c1}$ ,  $L_{c3l}$ , and  $L_{c4}$ , designed to minimize reflections that could potentially destabilize the laser. A straight waveguide with dimensions equal to that of the input/output waveguides of the triplexer (i.e., 3  $\mu\text{m}$  wide and 0.3  $\mu\text{m}$  thick) was fabricated on the same wafer.

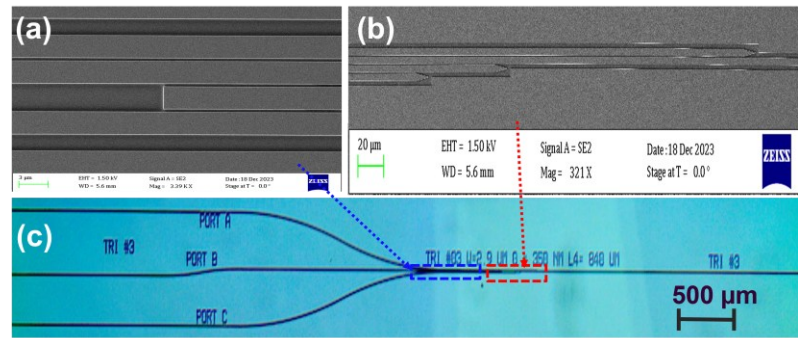


Figure 2.27: Fabricated triplexer sample under (a) SEM image (zoom) between S-bend and output section waveguide (b) Coupling waveguides at the output section (c) microscopic imaging of complete device.

## 2.5.2 Optical Characterization and Experimental Results

The optical characterization of the fabricated samples was performed using a free-space optics measurement setup described in section 1.3. Each device port was measured separately. The light source was focused on input ports and the output (at  $W_o$ ) was collected using lensed fibers. Two different lensed fibers were used during characterization: the first, made from SMF-28, for input wavelengths of 1530 nm and 1653.7 nm, while the second covered the wavelength of 2003 nm. For characterizing Port 1 and Port 2, which correspond to  $\lambda_{NH_3}$  and  $\lambda_{CH_4}$ , respectively, a single-wavelength (Yenista Optics) TLS was employed. Once the alignment was completed, the TLS was replaced with a broadband light source (Amonics ALSD) (1500 nm–1660 nm). The resulting output spectra was analyzed with a power meter and an OSA.

In the second configuration, described in section 1.3 is utilized for the characterization of  $\lambda_{NH_3}$ . The sample was tested using a lensed fiber suitable for the 2 μm range and the output beam was collected at  $W_o$  using another 2 μm compatible lensed fiber. The output was measured using a photodiode connected to an oscilloscope.

## 2.5.3 Optimization of coupling length ( $L_{c1}$ ) for: $\lambda_{NH_3}$ and $\lambda_{CH_4}$

The primary focus of the design optimization is to achieve high coupling efficiency for  $\lambda_{NH_3}$  and  $\lambda_{CH_4}$ , ensuring maximum transmittance at the output for both wavelengths. The critical parameters influencing this process are  $g$  and  $L_{c1}$ . As the propagating electric field profile shown in Figure 2.28 (b) indicates, light introduced at Port 1 propagates through an S-bend waveguide and couples into the Port 2 waveguide at every 330 μm of coupling length. Similarly, light launched at Port 2, corresponding to  $\lambda_{CH_4}$ , transfers its energy completely at every 250 μm of coupling length, (see Equation (2.13)). After reaching three coupling lengths for

$\lambda_{NH_3}$  and four coupling lengths for  $\lambda_{CH_4}$ , both wavelengths converge at a common length, forming a devoid-of-light region. This region can be strategically used to efficiently couple  $\lambda_{CO_2}$  and further prevent the interaction of  $\lambda_{NH_3}$  and  $\lambda_{CH_4}$  at the  $L_{1-3}$ .

### 2.5.3.1 Simulation results

A computed fundamental mode corresponding to each wavelength ( $\lambda_{NH_3}$  and  $\lambda_{CH_4}$ ) was launched at the input Ports 1 and 2, respectively. A pathway monitor was placed at the  $W_0$  and was normalized to the launch power. The analysis primarily examines the effect of changing  $g$  by adjusting the distance between Port 1 and Port 2, evaluated as a function of the wavelength launched at Port 1. The transmittance spectra corresponding to the  $g$  variations, with a fixed length of  $L_{c1} = 1030 \mu\text{m}$ ,  $L_{c3l} = 200 \mu\text{m}$ , and  $L_{1-3} = 160 \mu\text{m}$ , are illustrated in Figure 2.28 (a). The solid line indicates the transmittance for the wavelength emitted from Port 1, while the dotted line represents the transmittance for the wavelength emitted from Port 2. The spectator demonstrates a redshift of 35 nm per increment of 25 nm in the  $g$  dimensions for the wavelength emitted from Port 1. Likewise, a 25 nm  $g$  alteration results in a similar 35 nm shift in the spectra for the wavelength emitted from Port 2. Conversely, the transmittance spectra for changes in length  $L_{c1}$  for both laser Ports 1 and 2 were analyzed with a fixed  $g = 300 \text{ nm}$ ,  $L_{c3l} = 200 \mu\text{m}$ , and  $L_{1-3} = 160 \mu\text{m}$ , as illustrated in Figure 2.28 (b). The spectra show a blueshift as  $L_{c1}$  increases, shifting by 15 nm for every 30  $\mu\text{m}$  change in length.

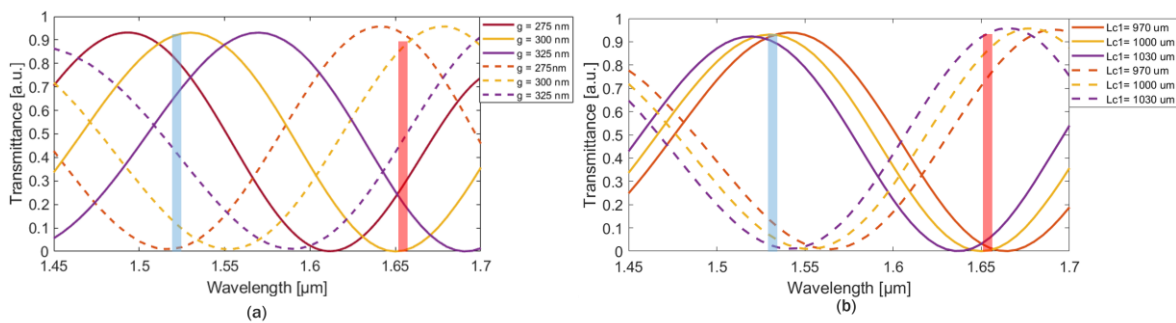


Figure 2.28: Transmittance curves as a function of the wavelength when launching from Port 1 (solid) and Port 2 (dashed) and by varying (a)  $g$  and (b)  $L_{c1}$ . The blue and the red bars indicate the region of ammonia ( $NH_3$ ) and methane ( $CH_4$ ) absorption, respectively.

The design is highly sensitive to the value of the gap, with changes in the order of tens of nanometers having a significant effect on transmission, potentially resulting in losses exceeding 25%. The optimal  $g$ -value is determined to be 300 nm by considering the high transmittance for both wavelengths, the region is highlighted with vertical blue and red boxes in Figure 2.28 (a). On the other hand, changes in  $L_{c1}$  for the waveguide exhibit a relatively flat response to

variations in transmittance within the range of tens of micrometers. In simulations,  $L_{c1}$  is optimized to 1030  $\mu\text{m}$  at a fixed  $g$ -value of 300 nm. After optimization, numerical simulations achieve a transmittance of 90% for a wavelength of 1530 nm and 91% for a wavelength of 1653.7 nm.

### 2.5.3.2 Experimental results

The fabricated sample collection includes samples with varying values of  $g$  while keeping constant  $L_{c1} = 1030 \mu\text{m}$  and  $L_{c3l} = 240 \mu\text{m}$ . Additionally, the collection includes samples with varying  $L_{c1}$  values, with a fixed  $g = 275 \text{ nm}$  and  $L_{c3l} = 180 \mu\text{m}$ . The measured values were normalized relative to straight waveguides (mentioned in Section 2.5.2). The normalized data were further refined using a smoothing spline with a smoothing parameter of 0.82. This process was employed to extract the underlying trend in the spectra while minimizing the impact of noise introduced during normalization, alignment, and Fabry Perot effects due to parasitic reflections in super luminescent sources. The spectral shift for  $g = 275 \text{ nm}$  and  $g = 300 \text{ nm}$  at a fixed  $L_{c1} = 1030 \mu\text{m}$  was analyzed by considering a broadband excitation at the input ports of the triplexer, as depicted in Figure 2.29 (a), showing normalized transmittance. Modifications to the  $g$ -value result in a redshift of 60 nm (65 nm) when exciting Port 1 (Port 2). For a 300 nm gap at Port 2, the output wavelengths exceed the operational range of the Amonics ALS D. The target wavelengths are marked with blue and red vertical boxes. The normalized transmittance obtained for these gap values was 45% and 31%, respectively. As shown in Figure 2.29 (b), Port 1's spectrum exhibited a blueshift with increasing length  $L_{c1}$ , with peak shifts of 25 nm for every 30  $\mu\text{m}$  increment, consistently with simulation results. For Port 2, the selected spectra were obtained for  $L_{c1}$  values of 1000  $\mu\text{m}$  and 1030  $\mu\text{m}$ . Further decreasing  $L_{c1}$  would result in output wavelengths exceeding the operational range of the Amonics ALS D, which is typically around 1660 nm. The distance between the transmittance peaks was measured at 100 nm. Similarly, the wavelength emitted from Port 2 also demonstrated a blueshift of 25 nm for every 30  $\mu\text{m}$  change in length, maintaining a peak-to-peak separation of 100 nm.

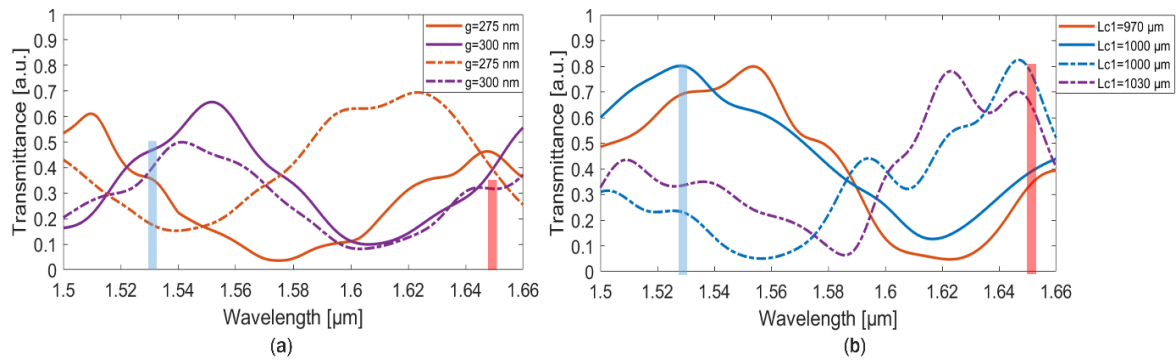


Figure 2.29: Normalized transmittance spectra of the triplexer for wavelengths released at Port 1 and Port 2 for varying: (a)  $g$  and (b)  $L_{c1}$ . The blue bar indicates the region of ammonia ( $\text{NH}_3$ ) absorption, and the red bar signifies the region of methane ( $\text{CH}_4$ ) absorption.

The change in  $L_{c3l}$  is linearly affected with the transmittance of  $\lambda_{\text{NH}_3}$  and  $\lambda_{\text{CH}_4}$ . As illustrated in Figure 2.26 (b), an optimal configuration was identified with  $L_{c1}$  set at 1000 μm and  $g$  of 275 nm and reduced  $L_{c3l}$  to 180 μm. The influence of cascaded coupling length  $L_{c3l}$  is an important parameter, as it also serves as the path for  $\lambda_{\text{CO}_2}$ . The transmittances obtained for  $\lambda_{\text{NH}_3}$  and  $\lambda_{\text{CH}_4}$  were 82% and 73%, respectively.

#### 2.5.4 Optimization of coupling length ( $L_{c3l}$ ) for: $\lambda_{\text{CO}_2}$

The triplexer design is optimized for the coupling length  $L_{c3l}$  to ensure high coupling efficiency across all three wavelengths. The wavelength  $\lambda_{\text{CO}_2}$  is injected at Port 3. To prevent interactions with the S-bend in the pathway following Port 3, a cascaded waveguide section with length  $L_{c3l}$  is introduced. This length is carefully selected not only to maintain efficient coupling for  $\lambda_{\text{CO}_2}$  but also to avoid crosstalk with the other wavelengths,  $\lambda_{\text{NH}_3}$ , and  $\lambda_{\text{CH}_4}$ , which effectively minimizes the coupling to the  $L_{c3l}$  and  $L_{c4}$  waveguides. The value of  $L_{c3l}$  corresponds to the coupling length for  $\lambda_{\text{CO}_2}$ . The coupling length of the waveguide for  $L_{c3l}$  is determined by calculating the coupling length within a four-waveguide coupled system. The pathway for this wavelength is structured to extend from  $L_{c4}$  through Port 3, proceed to  $L_{c3l}$ , traverse the  $L_{c1}$  waveguide, and finally return to  $W_o$ , as shown in Figure 2.26 (b). Simulation and characterization results for varying coupling lengths  $L_{c3l}$  with  $\lambda_{\text{CO}_2} = 2003$  nm launched at Port 3 are shown in Figure 2.30. The plot exhibits a bell-shaped trend as  $L_{c3l}$  varies from 30 μm to 400 μm.

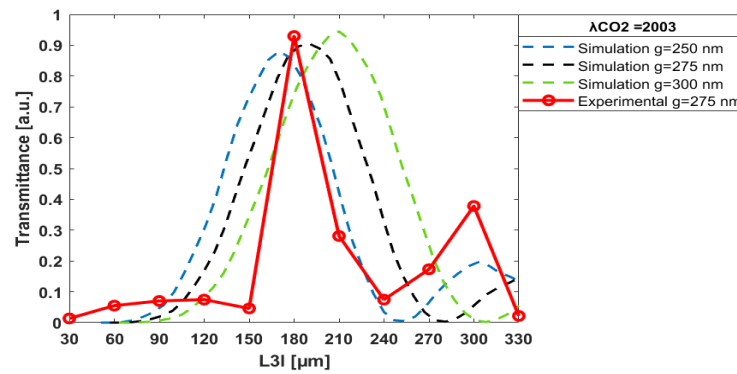


Figure 2.30: Transmittance calculated for varying coupling lengths  $L_{c3l}$  for wavelengths released at Port 3. The plot compares simulation results (dash-dot line) and experimental data (solid line with 'o' markers) for normalized transmittance across a range of  $L_{c3l}$  with different  $g$ -values.

The dashed lines show the simulation results for changes in the  $g$ -value with respect to the coupling length  $L_{c3l}$ . As the  $g$ -value increases in increments of 25 nm, the maximum transmittance shifts by a length of 20  $\mu\text{m}$  in  $L_{c3l}$ . This effect is attributed to the changes in the  $n_{\text{eff}}$  of the coupled device. Transmittance improves with increasing  $g$ -values since the fixed ( $L_{c1} = 1000$   $\mu\text{m}$ ) is not optimal at lower  $g$ -values. The device achieves its highest transmittance from simulation of 88% at the optimized coupling parameters of  $L_{c3l} = 200$   $\mu\text{m}$ ,  $L_{1-3} = 180$   $\mu\text{m}$ , and  $g = 300$  nm.

The normalized characterization results, relative to the straight waveguides (mentioned in Section 2.5.2), are presented for a set of triplexer devices in Figure 2.30, with a red curved solid line “o” marker. These results correspond to a range of  $L_{c3l}$  values, from  $L_{c3l} = 30$   $\mu\text{m}$  to  $L_{c3l} = 400$   $\mu\text{m}$ , with fixed values of  $g = 275$  nm and  $L_{c1} = 1000$   $\mu\text{m}$ , optimized for Port 3 to target  $\lambda_{\text{CO}_2}$ . The configuration of the 2003 nm diode laser characterization approach from Figure 2.26 (b) is used here. The device exhibits a greater sensitivity to  $L_{c3l}$  in experimental conditions than in simulations, with a tolerance of 25  $\mu\text{m}$  in the full width at half maximum of  $L_{c3l}$ . The optimal transmittance is achieved at  $L_{c3l}$  equal to 180  $\mu\text{m}$ , yielding a measured transmittance of 91% at a gap of 275 nm, in good agreement with the simulated maximum transmittance.

The core of the design focuses on maintaining the critical parameter, the gap between the waveguides and optimizing the coupling length. To achieve this, the waveguides are fixed at a width of 3  $\mu\text{m}$ , ensuring the phase-matching condition necessary for efficient evanescent field coupling. The transmittance obtained from all characterizations determines the overall coupling efficiency of the triplexer. Furthermore, the simulation results align well with the characterization trends, validating the design approach. The development of high-resolution EBL

has significantly enhanced the device's repeatability and reliability by ensuring precise nanoscale patterning and minimizing fabrication-induced variations. The estimated propagation loss is 4 dB/cm at 1550 nm and further decreases with an increase in  $n_{eff}$ . Optical losses observed during measurements can be attributed to several practical reasons. These include the difficulties associated with effectively coupling light into the chip's input port, using a free-space end-fire setup with lenses to align the optical fiber mode with the waveguide mode. Additionally, fabrication defects, unwanted reflections within the waveguide structure resulting from cleaved facets, and the attenuation of higher-order modes in the tapering region further exacerbate these losses. Collectively, these elements account for the losses documented in the measurements. The emerging challenge is the precise integration of the chip-scale diode laser into the specified ports on the chip.

# Chapter 3 - Integrated Sensing Architecture

In this chapter, various integration architectures and sensing methods are examined to enable compact, robust and automated spectroscopic device assembly. In free-space optics-based spectroscopy, using lenses, polarizers, and mirrors, for example in QEPAS and LITES methods, lies their lack of compactness, limited compatibility with sensor, susceptibility to interference artifacts, and risks of misalignment [33], [84]. For improved portability and compactness, an alternative light-guiding approach to QTF is utilized. Additionally, a new class of PIC integration with QTF has been introduced for gas sensing applications.

## 3.1 SPF Integrated Sensing System

In the last few decades, optical fiber technology has attracted significant interest across various fields, including medical, industrial engineering, and environmental monitoring [85]. Fiber sensor technology has undergone extensive research for its capacity to measure a wide range of parameters, including refractive index (RI), temperature, magnetic field, stress, strain, and liquid properties. This widespread interest can be attributed to its exceptional advantages, such as high sensitivity, flexibility, immunity to electromagnetic interference, resistance to corrosion, compact size, and cost-effectiveness compared to conventional sensors [86], [87], [88], [89].

Among various fiber technologies, filling gas or liquid into the core or cladding of optical micro structured fibers becomes challenging due to complexity and the difficulty of achieving long interaction lengths [90], [91]. Other methods, such as using hollow-core fibers, also face challenges, particularly with the concurrent injection of light and gas [92]. Additionally, hollow-core fibers are mostly designed to operate within a narrow bandwidth. In contrast, D-shaped Side Polished Single Mode Fiber (SP-SMF) have been successfully demonstrated as temperature sensors, humidity sensors, and magnetic fluid sensors [90], [93], [94], [95], [96]. The wheel-side polishing fabrication methods and wide bandwidth range make SPFs more attractive for low-cost, large volume production and multiple trace gas detection applications. Most standard silica fibers can be polished to varying depths and exposed to core lengths. With a good surface finish and precise etch depth, SPFs achieve low loss in air [34], [97]. Additionally, SP-SMF are inherently resistant to electromagnetic interference, corrosion, and environmental factors, making them an ideal sensing tool in challenging environments [35].

D-shaped fiber structures have been reported in which half of the cladding section is polished, allowing a stronger interaction between the optical mode and the target analytes [98]. Wang et al. demonstrated the temperature sensor based on helical core fiber, which is polished as a D-type fiber coated with a layer of gold [99]. Studies of Ag/TiO<sub>2</sub> plasmonic formation combined with SPF have been described by Yousuf et al. to build the humidity sensor [100]. Further, Xu et al. designed the magnetic field sensor based on the magnetic fluid and side-polished hollow-core optical fiber [101]. A film of cholesteric liquid quartz is employed to the SPF to give the capability of measurement of volatile organic compound (VOC) gases [102]. A recent work reports measuring the liquid level and refractive index by using the side polished plastic optical fiber [103]. Moreover, a humidity sensor with tremendous sensitivity employs a side-polished in-fiber DC coated with gelatin [104].

### 3.1.1 Refractive Index Sensing

Evanescent field sensing is a near-field phenomenon that exploits the characteristics of light waves confined within optical structures, such as fibers and photonic integrated circuits. Wherein the light nears the critical angle for total internal reflection (TIR), a fraction of the wave energy exponentially decays from the core to cladding with increasing distance from the interface [105], [106], [107], [108]. The SPF consists of a cladding with a refractive index of 1.44399 and a core that is 0.08% higher in refractive index than the cladding, manufactured by Phoenix Photonics Ltd at 1550 nm. The cladding etch depth and evanescent field interaction length of the SPF are shown in Figure 3.1 (a).

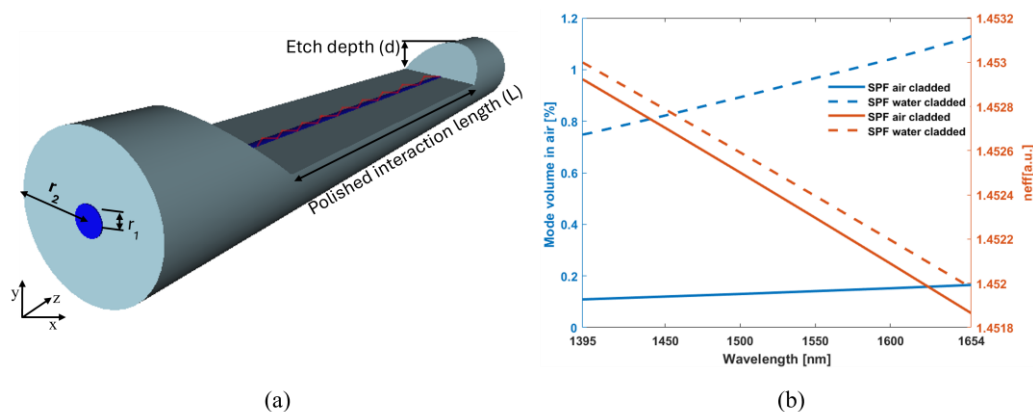


Figure 3.1: (a) Geometrical structure of SP SMF. (b) The mode volume in air and water-cladded (RI = 1.3) fibers in left y axis, along with the respective  $n_{eff}$  values in right y axis for a range of wavelengths.

The mode volume in air of the SPF for a range of wavelengths targeting 1395 nm and 1654 nm, specifically for water vapor and methane, is depicted in Figure 3.1 (b). As the wavelength

increases, the mode volume in air-cladded SPF increases slightly (0.1% to 0.16%). When the cladding refractive index is changed from air to water (RI = 1.3), the mode volume in the cladding increases from 0.1% to 0.76% at 1395 nm. Similarly, the left y-axis demonstrates the variation in  $n_{eff}$  for a range of wavelengths, demonstrating that the higher  $n_{eff}$  at 1395 nm, compared to 1654 nm, shows the effectiveness of mode confinement, which is higher for water. The core has a diameter ( $2 r_1$ ) of 8.2  $\mu\text{m}$ , and the cladding has a diameter ( $2 r_2$ ) of 126  $\mu\text{m}$ . The polished interaction length ( $L$ ) is 17 mm, which acts as the active region where analytes can interact with the evanescent field. The etch depth, which is the depth at which the cladding is removed during fabrication, is approximately equal to  $r_2 - r_1$ . The dispersion relation of the SPF is calculated using the Sellmeier equation for pure silica, with the simulation carried out using the FD-BPM.

In the BPM, the light transmission of the SP-SMF has been examined, which is employed to evaluate and calculate the propagating modes profile of the proposed structure. An external boundary covers a PML condition during the simulation assessment. The refractive index of analytes like air, water, and isopropanol have been assumed at the polished region of the fiber. The chosen analytes have lower refractive indexes than 1.45 (silica) in which most of the light confines to the core region. From Figure 3.2 a small portion of the light is gradually getting confined to the core when analyte's refractive index increases from  $n = 1$  to  $n = 1.3$  in the tapered region. This depends on the increase in  $n_{eff}$  tending to the increased confinement factor. The propagation of light depends on the refractive index of the materials. When the signals pass through the polished region, the light spectrum are evanescently available at the polished surface due to the effect of the analytes' refractive index. Thus, the transient impulse is created, and light modes travel through the section of the analyte. In this way, the impacts of the SP-SMF arrangements converted the optical signals into physical parameters involving the silica refractive index.

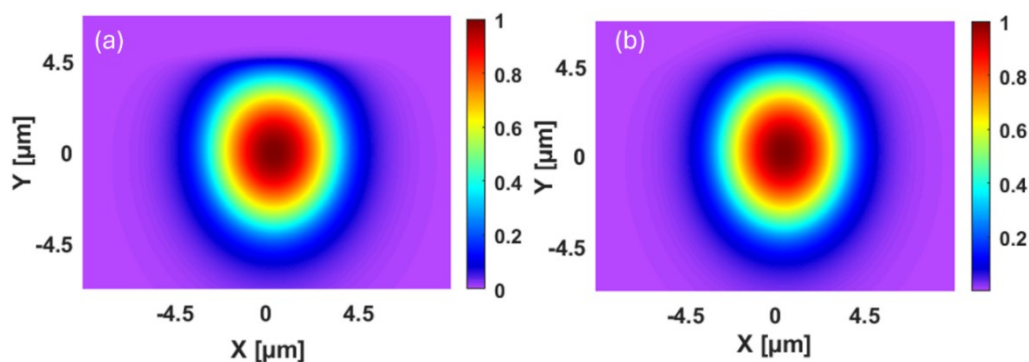


Figure 3.2: Fundamental mode profile when the cladding of the SP-SMF is (a) air and (b) water.

Moreover, the transmittance when air, water, and isopropanol are set in the polished region has been studied as shown in Figure 3.3. At the wavelength of 1530 nm, the transmittance of isopropanol ( $T=0.869$ ) is higher than water ( $T=0.859$ ) and air ( $T=0.842$ ), respectively. The transmittance also depends on the wavelength, which is going to increase as the wavelength increases.

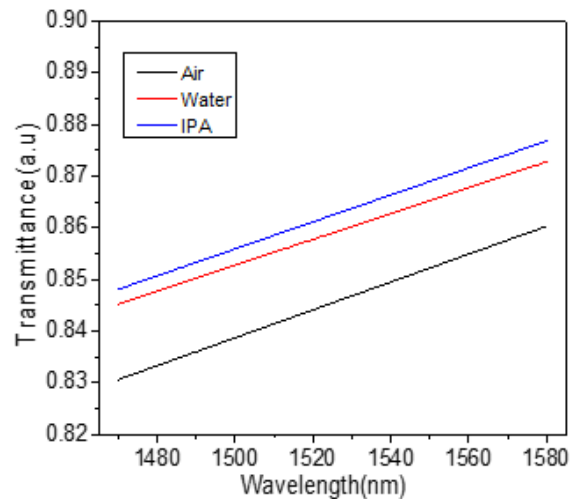


Figure 3.3: The transmittance of SPF as a function of wavelength for different analytes.

The experimental schematic diagram is shown in Figure 3.4 which comprises the necessary instruments for optical characterization. A tunable laser (TL) with a wavelength range of 1460 nm to 1580 nm has been used and connected to the fiber. The output signal was sent to a photo detector (New Focus-2033, USA) that connected to an oscilloscope to detect the transmitted signal. Both ends of the sensing structure have been connected between the input (light source) and output (photodetector). The whole experimental process is taken at the room temperature ( $25^{\circ}\text{C}$ ).

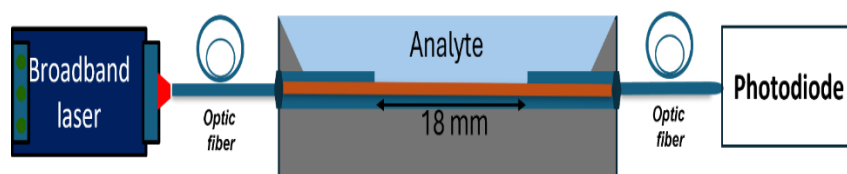


Figure 3.4: The schematic diagram of SP-SMF refractive index sensing scheme.

The microscopic view of the polished region has been shown in Figure 3.5 (a). Here, the sensing and polished section of the SPF is shown along with the polished regions (on the left and right sides). Both ends of the SPF are connected by FC/PC connectors to lead in (light source) and out (photodetector) the light. A substrate was designed on the FreeCAD Multiphysics; after that, it was fabricated by using the 3D printer (Photon Mono Se Anycubic). A valuable attribute of a sensor is its stability. To achieve stability and minimize the signal noise, SPF has

been kept inside a 3D printed reservoir, which is fixed with an optical table to avoid any movement. The shape of the reservoir is shallow, deep in the middle, where the analytes or liquids have been filled at the upper part of the tapered region. Figure 3.5 (b) highlights the installed experimental setup with lead in SP-SMF to lead out SP-SMF.

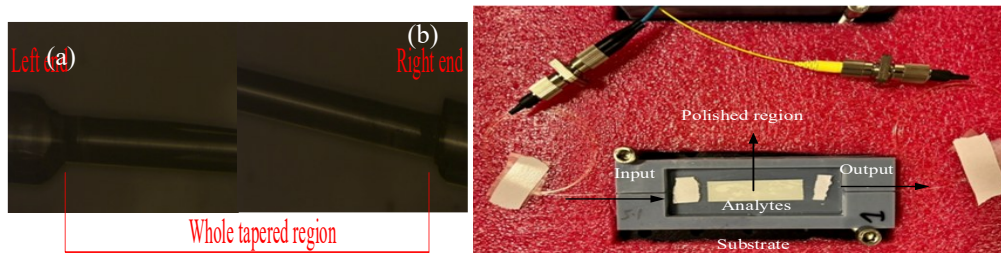


Figure 3.5: a) microscopic view of the tapered region, and b) the sensing setup with the reservoir.

In the wavelength range of interest (1460 nm to 1580 nm), the photodetector sensitivity was set to low (produces a smaller electrical signal for a given amount of optical power), and the input power was set to 4mW. Figure 3.6 (a) indicates the experimental results with respect to wavelength and normalized transmittance with respect to source by analyzing the analytes air, water and isopropanol, respectively. The photodiode gives a higher voltage in the case of isopropanol (blue curve) as it has higher RI than air and water. The black and red curve shows the voltage value of air and water, respectively. The maximum voltage curve is achieved at the wavelength of 1530nm. After that, there is a decline in the voltage with the increase of wavelength. Here, the effect of some natural noise can be seen, which depends on the optical setup and instruments (photodetector and oscilloscope). Furthermore, the plotted graph indicates the highest voltage at the wavelength of 1530 nm, at which the maximum voltages of air, water, and IPA are 4.350 V, 4.708 V, and 4.797 V, respectively. The voltage differences between air, water, and isopropanol are 0.44 V, 0.35 V, and 0.089 V, as the refractive index of air, water, and isopropanol are 1.0, 1.33, and 1.37, respectively. However, there is not much difference in voltage between the isopropanol and water due to the close refractive indexes. On the comparison with the simulation study, the experimental results are normalized and fitted for air, water, and IPA as surrounding media. Notably, Figure 3.6 (a), shows a difference in transmittance, with a relative change of 6 % between air and water and 2 % between water and IPA at the wavelength of 1530 nm where the maximum curve is achieved.

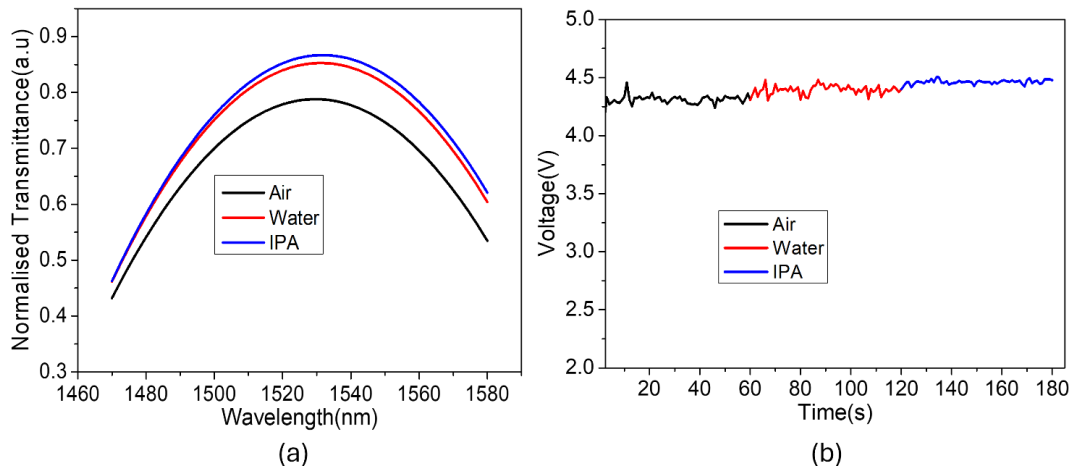


Figure 3.6: Experimental results of different analytes with respect to, a) wavelength and b) voltage v/s time.

On the other hand, the analysis of air, water, and isopropanol has been explored with respect to time variation. The wavelength has been fixed at 1530 nm, where the maximum power is achieved. The same parameters as the input power equal to 4 mW and low sensitivity were used for the photodetector. The overall time duration was set to 0 to 180s, equally distributed for the whole analytes (air, water, IPA). Each analyte has been investigated for the 60s. The experimental graph with respect to voltage and time variation has been outlined in Figure 3.6 (b). This graph indicates the evaluation of air, water, and isopropanol with real-time measurement. It has been seen that with the variation of time and change in the analytes, the voltage is changing accordingly, and the average voltage for each liquid is relatively constant. IPA gained the maximum voltage due to the higher refractive index rather than air and water. This accounts for the repeatability and validation of the SP-SMF fiber effect with various liquids and air. Hence, from the experimental results, it is observed that the measured voltage with respect to wavelength and time variations of analytes (air, water, and isopropanol) have the same qualitative behavior. The proposed sensor's effective optical parameters have been tuned several times to observe the results. The simulation results for transmittance variation with changes in refractive index indicate a transmittance change of 0.05 for every 0.1-unit increment in refractive index. Similarly, the experimental findings show a voltage difference of 0.33 for every 0.1-unit change in refractive index. Notably, refractive indices exceeding the core of the SPF result in the formation of non-guided modes.

### 3.1.2 Water Vapor Detection through LITES

SPFs is proposed as an interaction path length for water vapor measurement tool based on LITES methods. Compared to QEPAS, where the QTF must directly contact the gas sample

limiting its use with corrosive gases and introducing vulnerabilities to contamination, humidity, and temperature fluctuation [109], [110]. This non-contact approach not only eliminates such issues but also enables remote sensing of corrosive and hard-to-access gas samples. The details of the LITES acquisition technique and the evanescent field interaction method of the SPF are presented before. For the measurements, QTF<sub>2</sub> with a resonance frequency of 12.4527 kHz and a Q-Factor of 14823 are detailed in section 1.3.1.

The experimental setup is illustrated in Figure 3.7. The experimental setup employs a 1395 nm laser from Eblana laser, which is modulated using a waveform generator. The modulated laser beam is directed into a vacuum-compatible fiber adapter connected to a vacuum chamber. Within the chamber, the vacuum level is carefully maintained and monitored using a vacuum gauge, while a vacuum pump ensures appropriate pressure levels. The laser output exits the chamber and is directed into an externally sealed chamber via lensed fiber. The lensed fiber, mounted on a three-axis stage for precise alignment, focuses the beam onto the base of the QTF. This focused beam excites the QTF, enabling it to detect localized thermal changes induced by the evanescent field interaction within the chamber. The detected signal from the QTF is subsequently processed using a preamplifier and then analyzed by a lock-in amplifier to enhance the signal-to-noise ratio. The measurements are initially conducted in a non-vacuum or open configuration, where the external chamber is sealed, and contains constant air. The purpose of this sealed external chamber is to ensure that the concentration of gas inside remains stable, isolating the effects of the side-polished fiber within the vacuum chamber. Importantly, the distance between the lensed fiber and the QTF also plays a significant role in signal generation. This relationship is discussed in detail in Section 3.2.1.

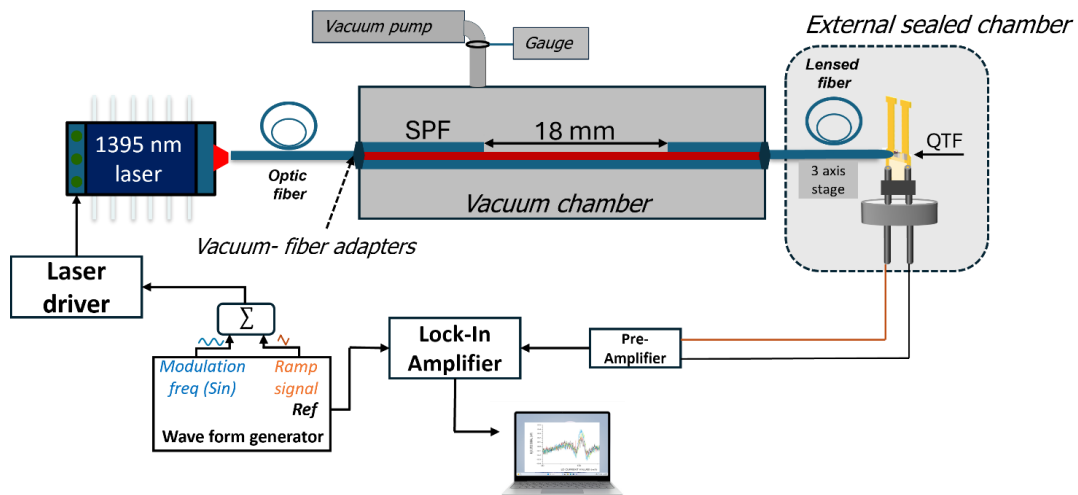


Figure 3.7: Schematic of the experimental setup for SPF-based LITES for water vapor sensing.

A second harmonic ( $2f$ ) detection scheme is utilized, i.e. the laser is modulated with the  $f/2 = 6.226350$  kHz, with an optimized AM of 140 mV peak to peak. The laser temperature is kept constant (22.5 degrees), and the laser current is scanned using a ramp period of 200 sec and AM 100 mV peak to peak. The LITES signal is acquired for a laser current centered at 109.2 mA, which is 1395 nm, i.e. the absorption wavelength of water vapor molecules. The characterization results are shown in Figure 3.8, where the light signal in mV is plotted as a function of wavelength. The plot displays with lower LITES signals of  $2.4 \times 10^{-4}$  mV for the vacuum configuration, with pressures up to 18 mBar, i.e. no interaction of the side-polished region with atmospheric gases or water vapor. In this case, the signal is solely influenced by the path length between the lensed fiber and the QTF.

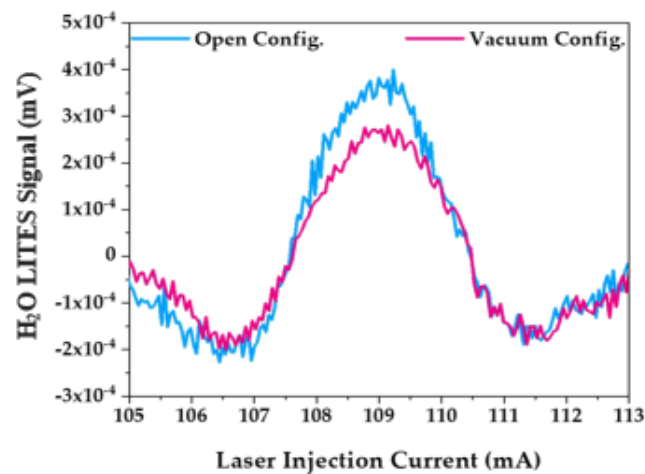


Figure 3.8: LITES signal at the vacuum configuration(blue) and at the configuration where the water vapor can interact with SPF (Magenta).

The chamber is opened and the air in the atmosphere has direct contact with the side polished region of the fiber, the increased signal value reaches  $3.95 \times 10^{-4}$ , plot represents the open configuration of the vacuum chamber, where the increase in signal is attributed to the evanescent field interaction of the side-polished region. This difference in signal is significant and repeatable, with a variation of  $1.5 \text{ mV} \times 10^{-4}$  for an SPF region of 17 mm. The calculated MDL values differ from 326 ppm to 202 ppm, at the room concentration 1.6 % water vapor.

### 3.1.3 Methane Detection through LITES

Methane gas detection is a critical area of research due to its significant environmental and safety implications [111]. Methane is a potent greenhouse gas with a global warming potential many times greater than carbon dioxide, and its detection is essential for monitoring emissions, ensuring industrial safety, and studying environmental processes and agricultural sector [112], [113]. A critical enhancement in this research is the use of SPF as the interaction path for

methane detection. The evanescent field interactions within the SPF significantly enhance the sensitivity of the system. This section explores the integration of LITES with SPF for methane sensing, providing a detailed description of the experimental setup and measurement methodologies.

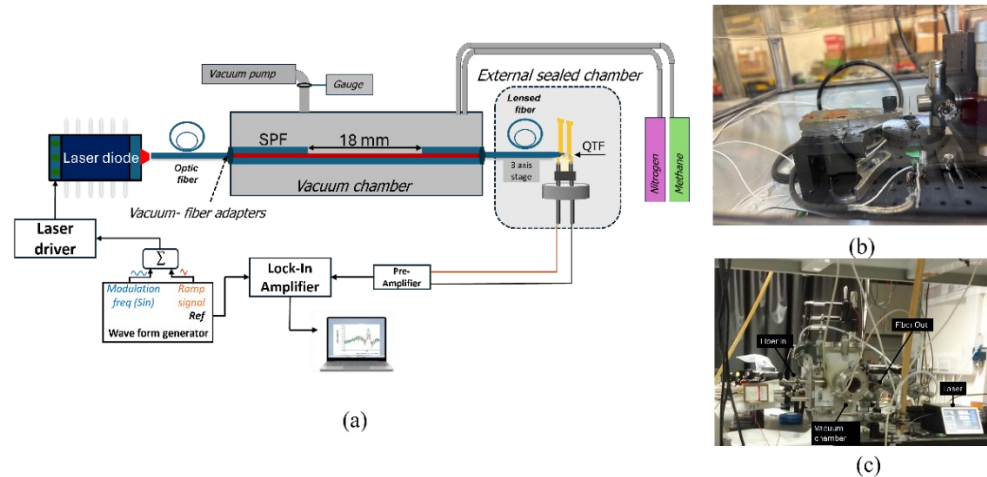


Figure 3.9: Schematic of the experimental setup for SPF-based LITES for methane gas sensing.

The experimental setup for methane detection is depicted in Figure 3.9. A 1653 nm laser, optimal for methane absorption, is modulated using a waveform generator to produce a wavelength-specific signal. The modulated laser beam is directed into a vacuum-compatible fiber adapter connected to a vacuum chamber. The chamber's vacuum level is carefully maintained and monitored using a vacuum gauge, with a vacuum pump ensuring precise pressure control. Inside the chamber, the laser light interacts with the SPF, where methane detection occurs through evanescent field interactions. The laser beam is subsequently directed via a lensed fiber to the base of the QTF, mounted on a three-axis stage for precise alignment. The QTF detects localized thermal changes caused by methane absorption, generating a measurable signal. This signal is amplified using a preamplifier and analyzed by a lock-in amplifier to maximize the signal-to-noise ratio.

Measurements are conducted in two environments within the chamber: vacuum configuration and methane environment. In the vacuum configuration, the chamber is sealed and maintained at a pressure below 18 mBar. Under these conditions, no signal is recorded, and only baseline noise is detected by the lock-in amplifier, as shown in Figure 3.10. This setup ensures no interaction between the side-polished fiber (SPF) and external gases, isolating the contributions from the optical path length between the lensed fiber and the QTF. Further, the chamber is filled with 1% methane at 1000mBar, and the methane gas begins to interact with the SPF

through evanescent field interactions, increasing the signal. The signal is recorded at different chamber pressures and reaches a maximum of  $1.5 \times 10^{-4}$  mV. This is repeated for different concentrations of gas; signal variation highlights the system's sensitivity and reliability for detecting trace methane levels.

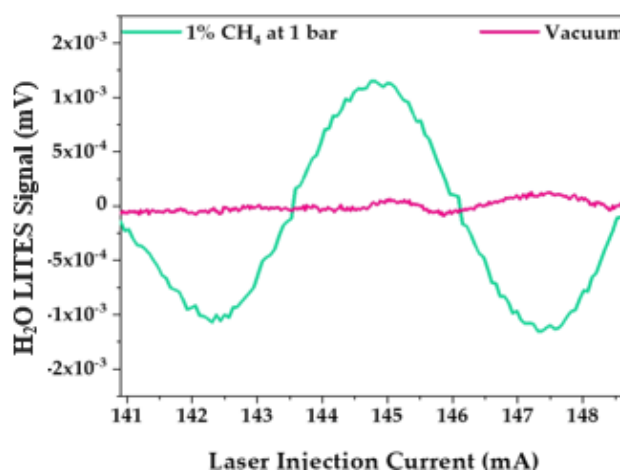


Figure 3.10: LITES signal using SPF for (Brown) Methane and (blue)the signal noise when the gas chamber is vacuumed.

This setup is particularly suited for remote and harsh environments where methane monitoring is critical. By transmitting light through fiber to a distant location, the system enables sensing in areas that are otherwise inaccessible or hazardous. Its robust construction and environmental resistance ensure precise measurements over extended periods, making it ideal for industrial, environmental, and safety-critical applications.

### 3.2 TLF Integrated Sensing System

This section introduces the use of Tapered lensed fiber (TLF) as a light delivery method that enables a compact, fast, and easily aligned integration approach for QEPAS and LITES spectroscopic techniques, with water vapor detection demonstrated as a proof of concept. TLF integration method offers significant advancements over conventional free-space optical configurations. Traditional setups rely on intricate optical components like lasers and converging lenses, which require precise alignment and are prone to misalignment challenges, making them unsuitable for harsh environments [114], [115], [116]. Lensed fibers, in contrast, provide a robust and compact alternative by also utilizing evanescent field interactions for gas detection, eliminating the complexity of free-space optics and enhancing mechanical stability. The adoption of a single, compact, and easily alignable lensed fiber offers a transformative alternative to traditional alignment-intensive methods for guiding laser light onto the QTF surface. With its built-in focusing capability, the lensed fiber produces a precisely confined beam with

a spot size  $< 300 \mu\text{m}$ . Its compact form factor and integrated design ensure straightforward positioning within the high-strain regions of the QTF prongs, without the need for extensive angular adjustments or additional focusing optics. This streamlined approach reduces the setup complexity and improves reproducibility, making it more suitable for real-world applications requiring robustness and portability, ensuring efficient photo-induced thermoelastic effects with minimal effort.

### 3.2.1 TLF Coupled LITES Measurements

The experimental setup utilizes a lensed fiber specifically designed for beam focusing to PICs, fabricated from standard SMF-28 optical fiber, the lensed fiber features a cone angle of  $95^\circ$ , a spot size of approximately  $2.5 \mu\text{m}$ , a stripped length of 2–5 mm, and an overall length of 100 cm, terminating with an FC/PC connector. The stripped part of the lensed fiber is shown on Figure 3.11. The fiber is tailored for operation in the wavelength range of 1525–1625 nm, ensuring compatibility with the laser source and enhancing interaction with the sample. The etch depth of stripped part further refines the evanescent field interaction strength. From High Pack manufacturer, TLF fabricated with core and cladding diameters of  $8.2 \mu\text{m}$  and  $128 \mu\text{m}$ , respectively, is used. Its compact design eliminates the need for bulky free-space optics, making it ideal for practical applications. A schematic representation of the lensed fiber and its alignment with QTF is shown in Figure 3.11 (c). For measurements, a QTF<sub>1</sub> with a resonance frequency of 8.12462 kHz and a Q-Factor of 11390 is employed.

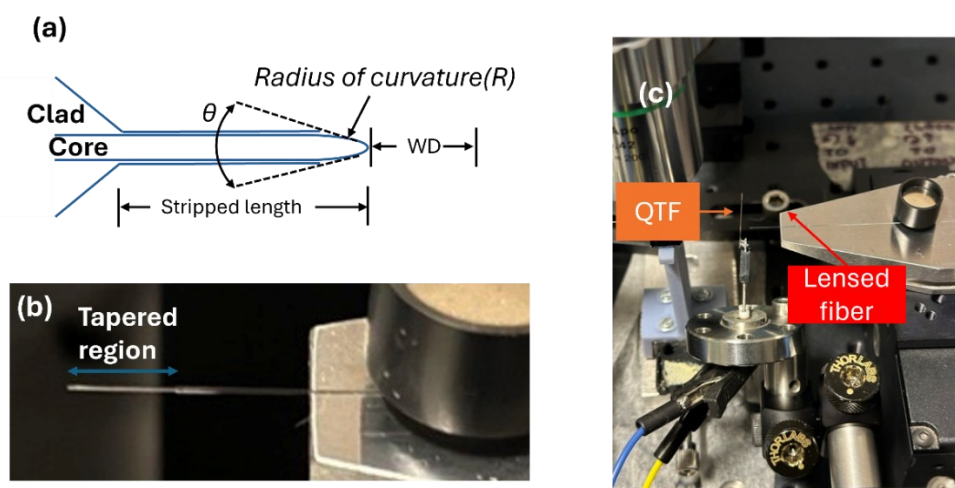


Figure 3.11: (a) drawing of the lensed fiber (b) The tapered region of lensed fiber in zoom and (c) Experimental setup of SPF to QTF in LITES configuration.

A 1395 nm diode laser, targeting a strong near-IR water vapor absorption feature identified in the HITRAN database, was used as the light source [117]. The laser was modulated using a ramp waveform to scan across the absorption peak and optimize the LITES signal. The QTF<sub>1</sub>,

characterized for resonance frequency and Q-Factor, was tuned to ensure sharp resonance and minimal energy loss, critical for high sensitivity. The experimental schematic is shown on Figure 3.12. The detection scheme of QTF<sub>1</sub> is detailed in section 1.3. Here the 1395 nm laser is focused to the base of QTF utilizing the lensed fiber. The path length for water vapor detection is the distance between the lensed fiber and the QTF.

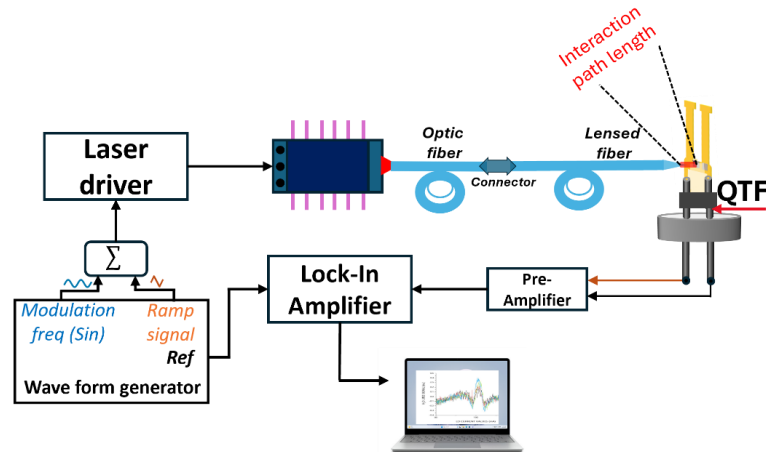


Figure 3.12: Schematic of the experimental setup for evanescent field and integration method of Lensed fiber using LITES.

Measurements were performed by positioning the lensed fiber at various distances relative to the QTF prongs. The distances ranged from 0 mm to 3 mm, with a position of 0 mm corresponding to the fiber being aligned maximum close to QTF. This arrangement enabled the detection of water vapor through the combination of the evanescent field emitted from the tapered region of the fiber and water vapor in the interaction path ( $L$ ). A ramp signal generated by the AWG was used to scan the laser current within its tuning range, thus sweeping the wavelength across the water vapor absorption feature.

The measured LITES signal relative to the water vapor detection is shown in Figure 3.13, demonstrating the ppm-range sensitivity of the developed sensing architecture [117]. An increase in the optical path length initially leads to an enhancement in the LITES signal, as the interaction between the evanescent field and the target analyte is maximized. However, as the QTF is moved farther away from the TLF, the signal begins to decrease. This reduction occurs because the focal point of the laser beam shifts and diverges, reducing the efficiency of the energy transfer to the QTF and thereby reducing the signal strength.

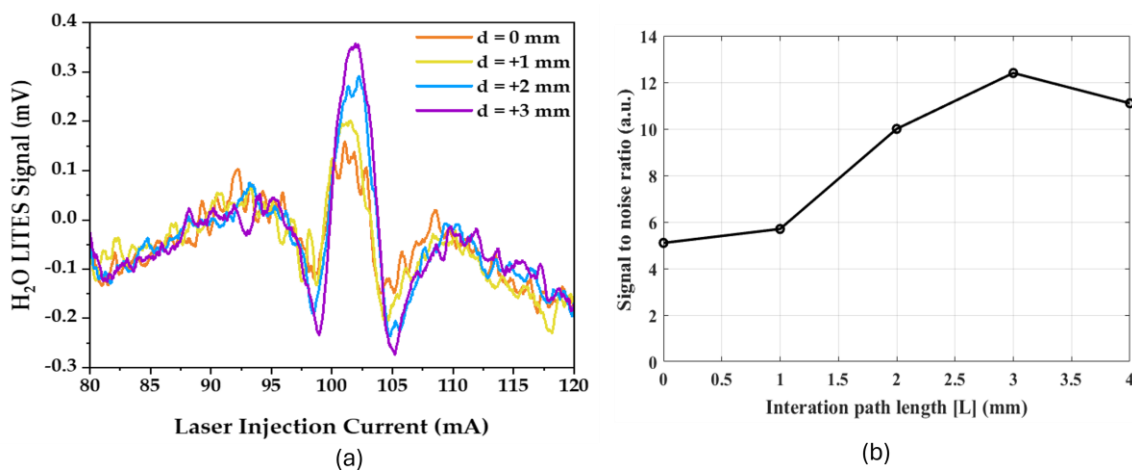


Figure 3.13: LITES experimental result regarding varying the distance between the QTF and lensed fiber.

### 3.2.2 TLF Coupled QEPAS Measurements

This section introduces the integration of TLF for enhanced stability and increased sensitivity in QEPAS-based sensing systems, addressing limitations in conventional setups such as free-space precise alignment of the laser beam between the QTF prongs. SPFs are recognized for their robustness and reproducibility but are constrained by their limited interaction length, which is dictated by the polished section of the fiber [97]. Achieving consistent polishing depths across multiple fibers can be challenging, leading to performance inconsistencies. The reported on a Minimum Detection Limit (MDL) of 34 ppmv for methane using an SPF in a QEPAS setup. In contrast, tapered fibers are capable of higher sensitivity due to their smaller diameters and stronger evanescent field intensity [118]. However, they are inherently fragile, making them less suitable for harsh environments where mechanical durability is crucial. The reported varying sensitivities for three different tapered fibers used in a long-distance QEPAS system for acetylene detection. The MDLs achieved were 30 ppmv, 51 ppmv, and 13 ppmv for the three different taper parameters.

This system utilizes the wavelength modulation technique and the 2f detection scheme, which are widely employed in QEPAS-based sensing. It is important to note that the sensitivity of the QEPAS signal is directly proportional to the incident laser power, highlighting the necessity of optimizing the optical components in the system. TLF is designed to enhance interaction between gas molecules using the evanescent field, with control over the interaction strength. The experimental setup of TLF aligned to QTF is shown on Figure 3.14.

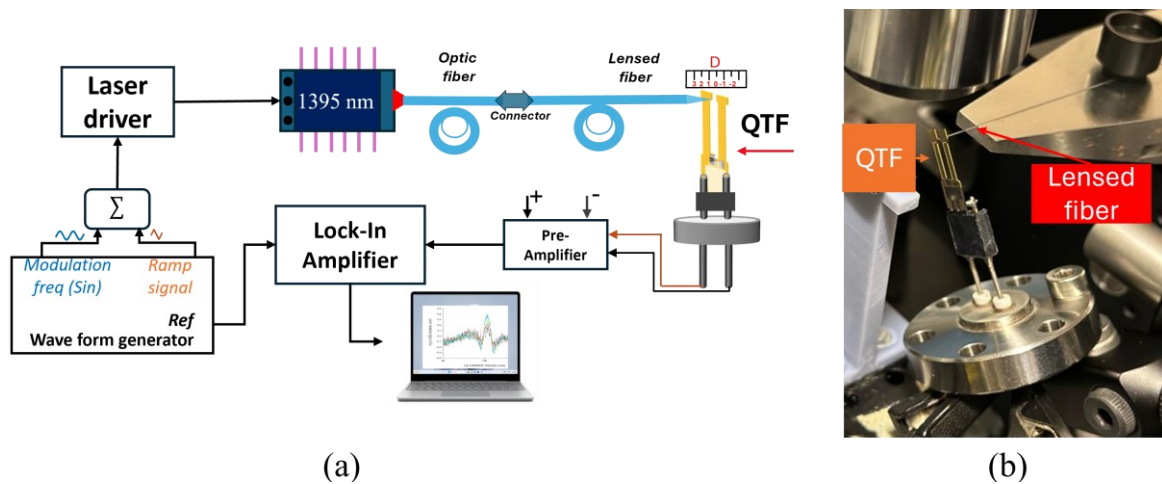


Figure 3.14: Schematic of the experimental setup for TLF to QTF in the QEPAS detection scheme. (b) Experimental alignment setup of TLF to QTF.

For this experiment, the same custom QTF<sub>1</sub> and the similar experimental setup were employed. During the experiment, the TLF is positioned inside the two prongs of the QTF at various distances from the QTF plane, including positions both outside and inside the QTF prongs. The lensed fiber is connected to the 1395 nm-emitting laser diode, and it is positioned on a three-axis stage for precise alignment. The zoomed image of the core of the experimental setup is shown in Figure 3.14 (b). Concurrently, the QTF is also mounted on a three-axis stage, in addition to a pitch and yaw angle stage. A pre-amplifier is used to collect the weak piezoelectric current signal, which is further enhanced filtered, and functioned by the lock-in amplifier. Also, in this case, the wavelength modulation and the 2f detection scheme were employed. Measurements were performed at different distance (namely D) positions (from -4 mm to 9 mm) and repeated under identical conditions to ensure reproducibility. The laser injection current is modulated using a ramp wave signal, generated by the AWG, to scan the laser wavelength across the H<sub>2</sub>O absorption feature peak within the laser tuning range. The amplitude of the ramp was optimized to successfully sweep the laser wavelength across the entire water absorption feature. In addition, the AWG also generated a sine wave having an amplitude maximizing the H<sub>2</sub>O QEPAS signal and a frequency of  $f_0/2$ .

Figure 3.15 illustrates the QEPAS signals obtained from various positions of lensed fiber, both inside and outside the prongs of the QTF. This positioning allows for effective gas sensing through the evanescent light emitted from the tapered region of the fiber. The experimental results show a broad working range, with positions ranging from -4 mm inside the QTF to 9 mm outside the QTF. The measurements are able to generate QEPAS signal with QTF positions from 0 to -4 mm, exploiting the evanescent field interaction of tapered region. The calculated sensitivities allow the H<sub>2</sub>O atmosphere levels monitoring, with tens of ppm range [117].

Finally, the focused beam produced by the TLF at  $d = 4$  mm is ideal for ensuring high sensitivity in measurements.

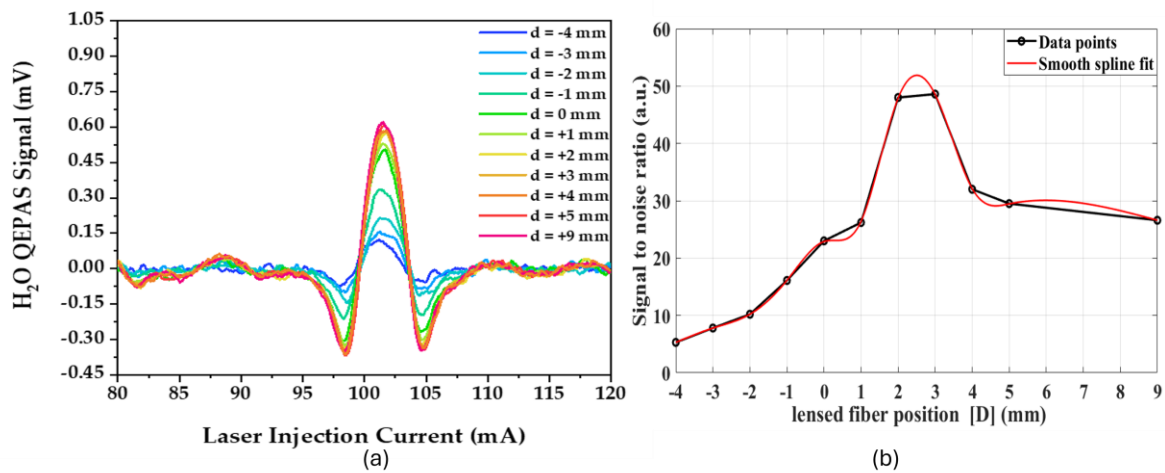


Figure 3.15: a) QEPAS signals for water vapor sensing at different values of  $d$ . (b) Signal-to-noise ratio as a function of  $d$ .

The TLF integration setup enables efficient and closest light delivery to the QTF in QEPAS, which particularly advantageous in high gas concentration environments, as it reduces undesired gas interactions along the optical path. The primary factor contributing to the reduced sensitivity, compared to free-space LITES and QEPAS, is the lower excitation optical power. Interband and quantum cascade lasers, commonly used for gas sensing in the mid-infrared region, typically provide higher power than the laser diodes available in the shortwave range with optical fiber coupling. Additional optical losses arise from factors such as fiber connector interfaces, the positioning of the QTF. Initial alignment is typically performed using an IR camera to optimize the optical path. By rapidly switching the input laser wavelength using spectroscopically relevant multiplexers, the system can match the absorption features of various trace gases, enabling multi-gas sensing applications. The integration of a fiber coupled laser output with a lensed fiber system offers significant potential for compact and integrated designs in both LITES and QEPAS techniques.

### 3.3 PIC Enabled Semi-Integrated Sensing Architecture

The increasing demand for compact, efficient, and highly sensitive spectroscopy systems has increased research efforts aimed at integrating advanced photonic devices with gas sensing technologies. Conventional spectroscopic configurations typically depend on critical setups that utilize free-space optics with bulky optical components, rendering them impractical for applications that necessitate portability, durability, and reduced alignment complexities. Fiber integration still has limitations due to its fragile nature and the complexity of extensive optical operations. Integrated photonic devices present a promising platform to address these challenges. Moreover, advancements in integrated optical sources significantly contribute to the realization of a fully laser integrated system. These developments focus on integrated lasers and multiplexers discussed in section 2.2, in a single photonic chip integrated into QTF. Integration ensures that the photonic chip's waveguides or optical elements are precisely aligned with the QTF, facilitating maximum energy transfer and optimizing the signal-to-noise ratio. In this context, the optical coupling efficiency still represents the most critical parameter, often limiting overall system sensitivity [119], [120].

To the best of our knowledge, there are no previous attempts to develop a full- or semi-integrated photonic sensing system exploiting on-chip waveguides with this type of piezoelectric resonator. The only closely related work was presented by De Carlo *et al.*, reporting the modeling and the design of a QEPAS sensor with the laser source and optical components for laser beam delivery bonded together and semi-integrated with the quartz tuning fork [121]. In their proposed configuration, an integrated waveguide directly couples the laser output with an optical ring resonator placed between the prongs of the QTF, with a pair of mechanical resonators confining and enhancing the standing sound waves produced by the modulated evanescent electric field. This configuration provided a pressure of the acoustic wavefront comparable with the free space on-beam QEPAS. However, the full integration of photonic components with QTFs still needs to be experimentally verified.

This work demonstrates a novel semi-integrated sensing architecture for QEPAS and LITES sensing that combines a  $\text{Si}_3\text{N}_4$  optical waveguide with a low-frequency, T-shaped, and custom-designed QTF as detector. The designed 3.8 mm-wide S-shaped  $\text{Si}_3\text{N}_4$  waveguide path effectively prevents interference due to scattered light, a common issue in integrated sensing platforms [122]. For this proof-of-concept, water vapor was detected targeting the absorption line at  $7,181.16 \text{ cm}^{-1}$  [123].

### 3.3.1 Si<sub>3</sub>N<sub>4</sub> Chip Coupling with QTF for QEPAS Applications

The initial integration step involves employing a straight waveguide on the chip, which acts as a foundational optical element. The light emitted from the waveguide is precisely guided to the region between the prongs of the QTF, ensuring optimal interaction with the acoustic resonance for signal generation. By demonstrating the capability to accurately direct light and generate measurable signals, this initial step lays the groundwork for advanced multi-gas detection systems integrated with photonic chips. The schematic of the system is shown on the Figure 3.16.

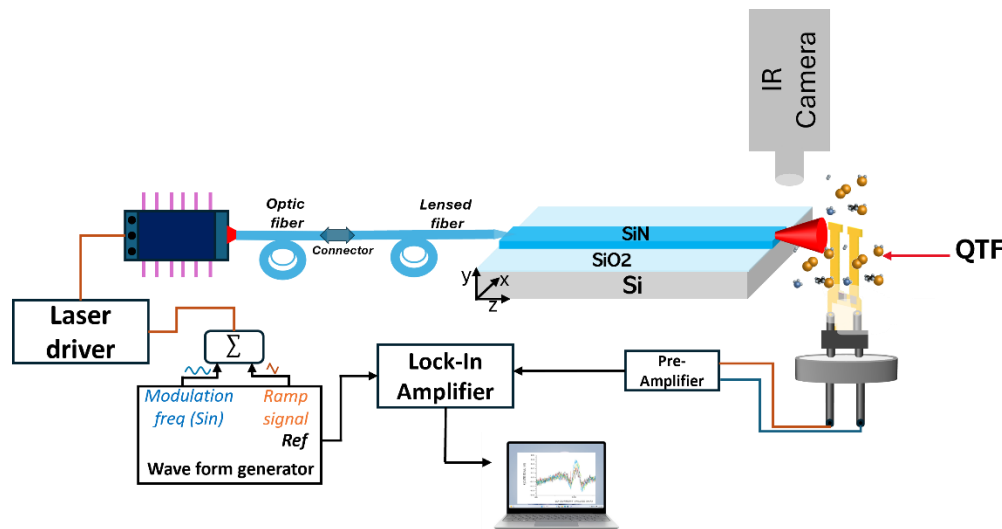


Figure 3.16: Schematic of the experimental setup for Si<sub>3</sub>N<sub>4</sub> waveguide-based Chip to QTF with QEPAS detection scheme

The QEPAS detection scheme and the laser modulation techniques are discussed in section 1.3. In this experiment, a Si<sub>3</sub>N<sub>4</sub> sample is used to guide the light into QTF. The Si<sub>3</sub>N<sub>4</sub> fabrication steps are explained in section 1.2. The Si<sub>3</sub>N<sub>4</sub> waveguide has a width of 3 μm and 300 nm thickness, which is compatible with the integrated laser mode profile. The device is non-clad-ded. The QTF is mounted on a three-axis stage, allowing precise adjustments for optimal alignment. The proximity of the QTF to the Si<sub>3</sub>N<sub>4</sub> chip and the output beam spot are carefully aligned using an IR camera to ensure proper light coupling and efficient interaction. A schematic of the experimental setup is shown in Figure 3.17, illustrating the alignment process and the experimental configuration.

The QTF and the chip must be placed close together, to avoid high divergence of the beam at the output of the waveguide that could hit the gold electrodes on the QTF surface, leading to high noise in the detection [124]. Since the resonance properties could be affected by the presence of the chip in proximity of the QTF surface [125], QTF<sub>1</sub> resonance frequency and Q-factor were monitored at different distances of the resonator with respect to the waveguide. Starting from the closest position (namely Position A) shown in Figure 3.16, the QTF was moved away

with 1 mm increments to three additional different positions (namely Position B, C, and D) not shown in Figure 3.16.

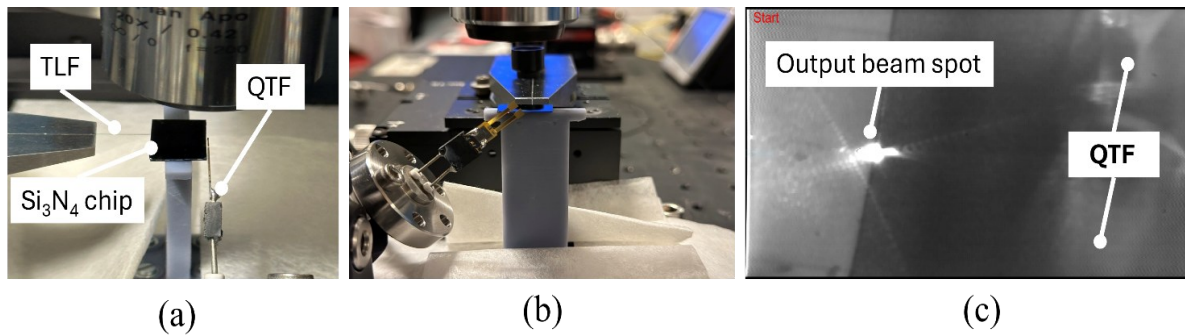


Figure 3.17: Photonic integrated chip to QTF coupling (a) Normal view (b) cross-sectional view (c) NIR microscopic camera view showing the output spot in the sample and the QTF nearby.

A QTF<sub>1</sub> with a resonance frequency of 8.12462 kHz and the calculated Q-Factor is 11390, as discussed in section 1.3.1. The side, cross sectional and top views of the experimental setup and IR camera view are shown in Figure 3.17. The experimental QEPAS results for water vapor detection are presented in Figure 3.18 (a). The signal is optimized through precise alignment, with the highest signal intensity achieved when the QTF is positioned closest to the spot. As the QTF moves away from the optimal position, the signal decreases. This is due to the divergence of the beam in the Y-position, which results in a weaker interaction between the light and the gas, leading to a lower signal strength. The closest position to the spot ensures the most efficient light-matter interaction, maximizing the signal for QEPAS detection. The fitted signals and the relative residuals shown in Figure 3.18 (b) demonstrate the effectiveness of this fitting procedure.

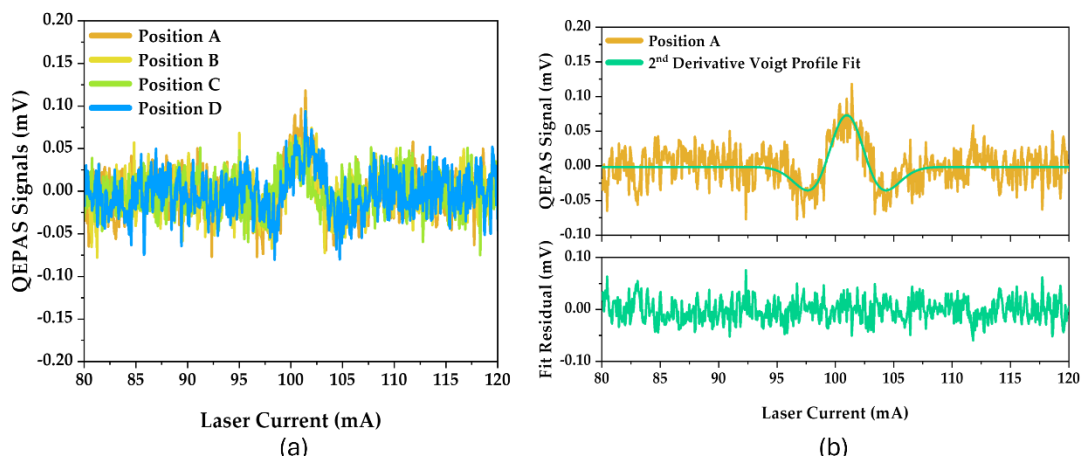


Figure 3.18: (a) Water vapor QEPAS signal, when Si<sub>3</sub>N<sub>4</sub> photonics chip is brought close to the QTF. (b) Second-derivative Voigt profile fitting of the QEPAS signals at QTF Position A. Green curves show the optimized fits to the experimental data (orange curves). In the lower panels the residual of the fit is reported for both techniques.

### 3.3.2 Si<sub>3</sub>N<sub>4</sub> Chip Coupling with QTF for LITES Applications

This section explores the integration techniques of Si<sub>3</sub>N<sub>4</sub> chips with LITES systems. The goal of this integration is to use the chip to guide light and enhance the path length for light interaction directly on the chip. The initial step involves using a straight waveguide on the Si<sub>3</sub>N<sub>4</sub> chip. The light emitted from the waveguide is precisely focused on the base of the QTF, ensuring optimal interaction between the light and the gas in the region between the prongs of the QTF for effective thermoelastic signal generation.

The experimental setup involves the use of a Si<sub>3</sub>N<sub>4</sub> sample to guide the light into the QTF, where the light's path length and interaction occur directly on the chip. The waveguide on the chip has a width of 3 μm and a thickness of 300 nm, which is optimized for the integrated laser mode profile. The device is non-cladded to allow efficient interaction with the analyte. QTF<sub>1</sub> is mounted on a three-axis stage for precise adjustments to align the light beam. The proximity of the QTF to the Si<sub>3</sub>N<sub>4</sub> chip and the output beam spot are aligned using an IR camera to ensure accurate light coupling. A schematic of the experimental setup is shown in Figure 3.19.

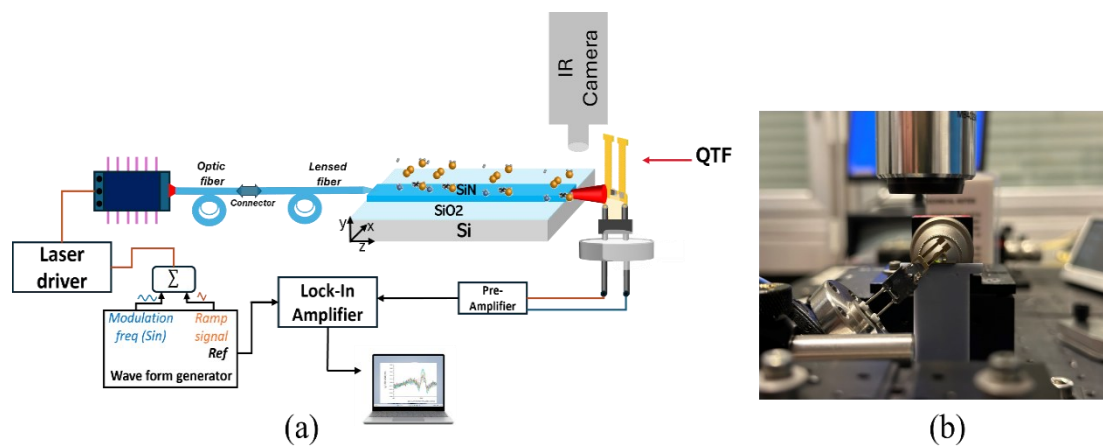


Figure 3.19: Schematic of the experimental setup for the Si<sub>3</sub>N<sub>4</sub> Photonic chip to QTF integration for the LITES scheme. (b) The experimental arrangement of the chip to QTF a cross-sectional view.

The alignment process is optimized to achieve the highest signal intensity when the QTF is positioned closest to the output beam spot. As the QTF moves further from the optimal alignment, the signal increases due to the new path length between the QTF and the chip. The more far gives a lower signal as the beam spot is no longer collimated or hitting the QTF. Which weakens the interaction between the light and the gas, thus leading to a reduced signal. The closest position to the beam spot ensures maximum light-matter interaction, optimizing the LITES signal.

These experimental results, detailed in Figure 3.20 (a), demonstrate the feasibility of integrating the  $\text{Si}_3\text{N}_4$  chip for on-chip light interaction and its effectiveness in generating LITES signals. The fitted signals and the relative residuals shown in Figure 3.20 (b) demonstrate the effectiveness of this fitting procedure.

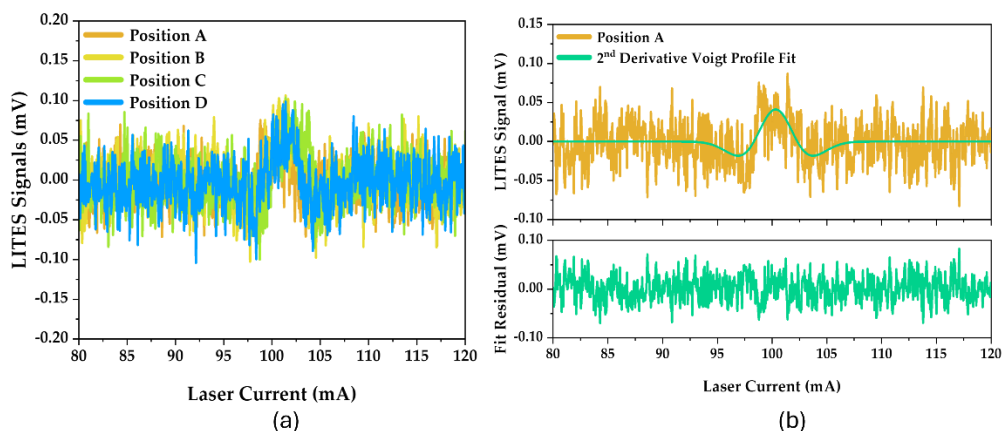


Figure 3.20: (a) water vapor LITES signal, when  $\text{Si}_3\text{N}_4$  photonics chip is brought close to the QTF. (b) Second-derivative Voigt profile fitting of the LITES signals at QTF Position A. Green curves show the optimized fits to the experimental data (orange curves). In the lower panels the residual of the fit is reported for both techniques.

The distance from the sample to QTF with respective SNR values is shown in Table 3.1. These experimental results demonstrate the feasibility of integrating  $\text{Si}_3\text{N}_4$  chips with the QTF and highlight its effectiveness in generating QEPAS signals. The integration proves to enhance the system's performance, facilitating more efficient signal generation from  $\text{Si}_3\text{N}_4$  waveguide for gas sensing applications. The peak values at different QTF positions (A through D) were extracted from the fitted signals for both QEPAS and LITES measurements and the resulting SNR values are presented in Table 2.

**Table 3. 1: SNRs calculated using peak values extracted from fitted signals for both QEPAS and LITES techniques at different QTF positions (A through D)**

	A	B	C	D
QEPAS	3.2	2.7	1.9	2.9
LITES	1.6	2.8	2.5	2

The SNR values presented in Table 3.1 demonstrate that both QEPAS and LITES techniques achieve comparable detection performance. The highest SNR was achieved using QEPAS at Position A (3.2), while LITES showed its best performance at Position B (2.8), but both techniques maintained effective detection capability across the entire tested distance range, with

SNRs consistently above 1.5 with a low optical power of  $\sim 300 \mu\text{W}$ , thus showing both good mechanical and optical stability. Low coupled power is a limitation; it is primarily due to the free space laser optical setup, it could be overcome with spot size converters, integrated sources and higher power diodes lasers available in the NIR range.

SPF-based sensing is highly suitable for long-distance gas detection. Water vapor and methane detection were performed to validate the evanescent field interaction-based sensing method. Additionally, TLF was employed as the sensing architecture to efficiently deliver light, enhancing the compactness of the spectroscopic system and enabling a robust, self-assembled design. To further improve the robustness and compactness of the spectroscopic systems, PICs were utilized. The experimental results demonstrate the successful coupling of  $\text{Si}_3\text{N}_4$  waveguide technology and custom-designed QTF exploiting both QEPAS and LITES detection techniques for gas sensing applications. This semi-integrated architecture represents a significant step toward miniaturized optical gas sensors, particularly for deployment in challenging environments where traditional approaches may be impractical. The comparable SNR values obtained for both QEPAS (1.9-3.2) and LITES (1.6-2.8) techniques suggest that either method can be effectively implemented with the reported semi-integrated platform. The slight performance advantage observed in QEPAS measurements, particularly at QTF Position A (SNR = 3.2), is also related to lower noise levels, thus indicating that it is easier to align the beam at the output of the waveguide between the QTF prongs. For the LITES case, the small light-molecules interaction volume considered, localized around the polished region of the optical lensed fiber and around the waveguide core-cladding interface, limited the performance. However, the consistent detection capability across all positions (up to 3 mm far from the waveguide output) demonstrates the robustness of both techniques and provides flexibility in sensor design and implementation.

# Chapter 4 - High Contrast Grating Hollow Core Waveguide

A promising solution for enhancing integration possibilities and enabling low-cost automated assembly, without relying on lenses and fibers, is the use of an integrated photonic chip. This chapter presents the design and numerical validation of a high-contrast grating (HCG) hollow-core waveguide (HCW) optimized for compactness and cost-effective chip-scale photonic integration. The waveguides incorporate a reflective inner surface to ensure high optical transmission, while their sidewall-less design enables gas to flow, making them especially well-suited for enhanced light-matter interaction.

## 4.1 Introduction to PIC based Hollow core waveguide

The HCW operates differently from conventional waveguiding systems, where the core consists of a low-refractive-index material, such as air, surrounded by a highly reflective cladding. Hollow-core fibers (HCF) represent an emerging field in photonics, with promising applications in biosensing and high-speed communication. For example, a fiber-optic Mach–Zehnder interferometer (MZI) employing a hollow-core photonic crystal fiber (HC-PCF) can detect carbon dioxide (CO<sub>2</sub>) concentrations in air, subsurface soil, and aqueous environments [126], [127]. However, HCFs are limited by the need for concurrent light and gas injections, bulkiness, limited manufacturing scalability, nonlinear effects, and limited bandwidth. Major losses in optical fibers stem from direct band-edge absorption, free-carrier absorption, and interactions with optical phonons [128], [129].

Chip-scale HCWs offer a promising route toward low-cost, integrated photonic systems, with the ability to seamlessly incorporate light sources, sensors, and electronic circuits onto a single platform. Chip-scale HCWs provide several advantages over solid-core counterparts, such as high-power laser delivery, simplified fabrication through a single etching process, potentially lower costs, and reduced nonlinear effects. Their low insertion loss results from the absence of Fresnel reflections when coupling light from free space into the air core. HCWs also exhibit high laser-damage thresholds, minimal end reflections, and low beam divergence. Gases or fluids can be introduced through side openings, not just from the ends. However, chip-scale HCWs may experience increased bending losses and have a limited numerical aperture [130], [131]. Reported integrated chip-scale HCWs include systems using materials like silicon

V grooves coated with metals, distributed Bragg reflectors, and anti-resonant reflection layers [132], [133]. However, these approaches face issues such as poor reflection from surrounding surfaces, multi-layer fabrication challenges, and difficulties in achieving a compact and integrated solution with LITES.

A novel HCW design is proposed, incorporating a silicon metasurface (i.e. a high-contrast grating (HCG) structure). The configuration consists of two chips aligned face-to-face, with the HCGs positioned opposite each other to form the waveguide. Light propagation is guided by the tailored HCG structure, optimized for specific target wavelengths. This thesis focuses on the design of HCWs for gas sensing applications, specifically targeting the detection of ammonia at 1550 nm (referred to as HCW<sub>1</sub>) and methane at 3270 nm (referred to as HCW<sub>2</sub>). A schematic representation of the design is provided in Figure 4.1. Transverse guidance within the waveguide structure is achieved through reflections from the high-contrast grating (HCG), while lateral confinement is realized by varying the HCG dimensions laterally, altering the effective refractive index. The methodological framework employed in this study uses the BPM, ensuring straightforward and intuitive design of long grating waveguides.

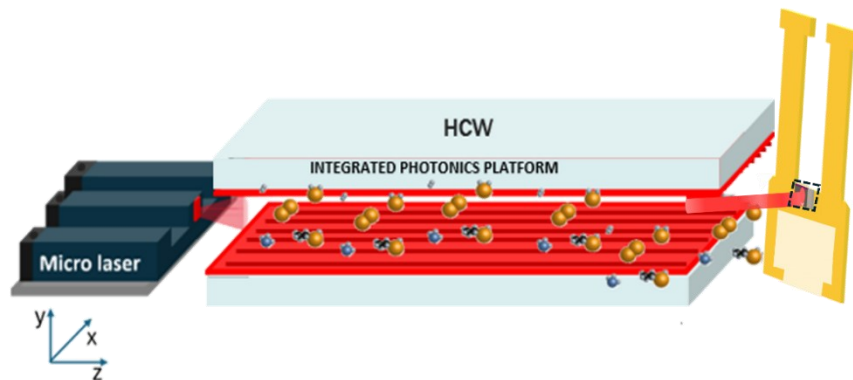


Figure 4.1 : Schematic diagram of HCG HCW-based gas spectroscopy.

A modulated laser beam is focused on the HCG-HCW. The distance between the chip platforms is denoted as ' $d$ ', with a total length of ' $L$ '. Within HCW, the incident light undergoes multiple reflections, facilitating interaction with gas molecules. Subsequently, the light that has interacted with gas molecules is directed toward the base of the QTF. For characterization purposes, a camera and photodetector are positioned downstream of the HCW to capture and analyze the transmitted light. The entire setup is housed within a gas chamber to enable gas sensing.

### 4.1.1 Theory and background

Metasurface gratings are artificial subwavelength structures designed to precisely control light by exploiting engineered resonances and diffraction effects. These ultrathin optical devices consist of periodic arrangements of nanostructures that can manipulate amplitude, phase, and polarization of light at scales smaller than the wavelength. One of the key physical phenomena enabling their functionality is guided-mode resonance (GMR), which occurs when incident light couples with the guided modes of an integrated waveguide layer through phase matching conditions [134], [135]. GMR arises from the interplay between two fundamental mechanisms: diffraction by the periodic grating structure and waveguiding in a high-refractive-index dielectric layer. In a typical configuration (Figure 4. 2), a nanostructured grating is fabricated on top of a planar waveguide (high-index material like Si or TiO<sub>2</sub>) sandwiched between lower-index materials (such as SiO<sub>2</sub> or air). When light interacts with this structure, the grating diffracts light into the waveguide layer where it excites guided modes that subsequently leak back out due to the periodic perturbation, creating strong resonant effects.

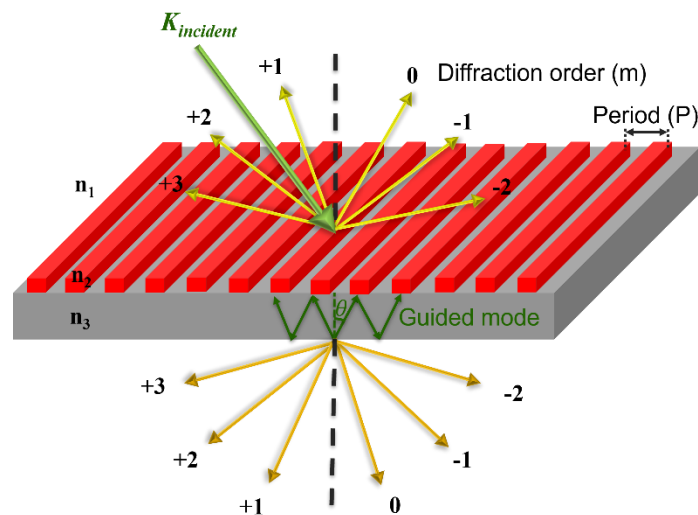


Figure 4. 2 : A sketch of a diffraction grating having a period  $P$  placed on a slab waveguide. The refractive index of the waveguide layer  $n_2$  is greater than the refractive index of the cladding layer  $n_1$  and the substrate  $n_3$ .

GMR is applicable when the grating  $P \lesssim \lambda$ , allowing light to couple into waveguide modes such as the fundamental transverse electric modes ( $TE_0$  and  $TE_1$ ). Under the phase matching conditions, incident light excites these guided modes, resulting in resonant interactions. Due to the periodic nature of the grating, these modes form supermodes—hybrid combinations of  $TE_0$  and  $TE_1$ —which exhibit symmetric field distributions. Among these, even symmetric supermode, which is in-phase at the center of the grating but out-of-phase with the incident light at

the same point, plays a crucial role. For example, A slab waveguide consists of a layer of high refractive index material ( $n_2$ ) sandwiched between two lower index materials ( $n_1$  and  $n_3$ ). It guides light using total internal reflection, which occurs when light travels from a higher to a lower refractive index and the angle of incidence exceeds the critical angle ( $\theta$ ), as defined by Snell's Law. For light to remain confined within the slab, the round-trip phase shift of the ray must equal an integer multiple of  $2\pi$ , allowing only specific propagation angles. This leads to discrete modes, and the ray tracing method can be used to derive the propagation constant for each mode. According to the ray tracing analysis only certain angles are allowed and the propagation constant ( $\beta$ ) of a supported mode by the slab waveguide is given as:

$$\beta_m = k_0 n_{eff} = k_0 n_2 \sin[\theta(m)] \quad (4.1)$$

The angles of the diffracted orders can be calculated from the grating equation which is given below.

$$n_2 \sin[\theta(m)] = n_1 \sin\theta_{incident} - m \frac{\lambda_0}{P} \quad (4.2)$$

Under phase matching conditions, the effective refractive index of the guided modes can be deduced from Equations (4.1) and (4.2),

$$n_{eff} = n_1 \sin\theta_{incident} - m \frac{\lambda_0}{P} \quad (4.3)$$

For a guided mode, the  $n_{eff}$  has the following constraints,

$$\max[n_1, n_3] \leq n_{eff} < n_2 \quad (4.4)$$

When a diffraction grating and a slab waveguide are brought into close proximity, and the angle of a diffracted mode aligns with that of a guided mode, the combined condition for guided-mode resonance is,

$$\max[n_1, n_3] \leq \left| n_1 \sin\theta_{incident} - m \frac{\lambda_0}{P} \sin\theta \right| < n_2 \quad (4.5)$$

The P at normal incidence for wavelength  $\lambda_0$  is,

$$P = \lambda_0 \left( \frac{2m}{n_2 + \max[n_1, n_3]} \right) \quad (4.6)$$

This phase relationship leads to constructive interference in the reflected field, resulting in high reflectivity. Thus, the coupling and interference of guided modes under GMR principles form the basis for the strong reflectivity observed in subwavelength gratings. GMR-based metasurface gratings remain highly effective for applications requiring narrowband filtering, enhanced light-matter interaction, or precise wavefront control [136], [137], [138].

## 4.2 HCG mechanism for Ultra-High Reflectivity

An ultra-high reflecting surface is achieved using a high-contrast grating (HCG) structure. This consists of a single layer of grating made from a high refractive-index material, such as silicon, on a SOI platform, which is fully surrounded by a low refractive-index material like air, as shown in Figure 4.3. In this 1D case, the structure is infinite in  $y$  and infinitely periodic in  $x$ .

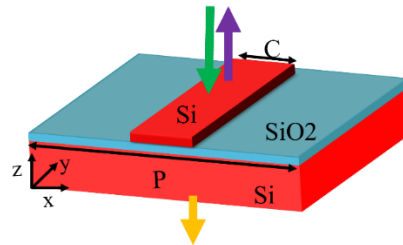


Figure 4.3: Unit cell configurations in 2D simulations of structures exhibiting periodicity along a single axis.

To calculate the complex reflection coefficient ( $r$ ) of the HCG, RCWA method is utilized. By fine-tuning the width, thickness, and period of the subwavelength grating, can match the  $k$ -vector of the incident light to achieve reflection for the fundamental diffraction order. HCGs give high reflectivity for surface-normal incident light. In this process, calculate the complex reflection coefficient 'r' of the HCG using RCWA. Consider a vertical incidence of the electric field, indicating a pure transverse mode within the HCG where the longitudinal component of the electric field is negligible. For constructive interference to occur, the phase difference between the reflected modes at the air/Silicon interface and after emerging from the SiO<sub>2</sub> layer must be equal to  $\delta m = 2m\pi$ , where  $m$  is an integer representing the order of the interference ( $m = 1, 2, 3, \dots$ ). This mode coupling similarly occurs at the input plane upon completing one round trip. Following these modes through one full trip allows for the attainment of a reflective solution. Moreover, at both input and exit planes, these modes transmit into low-index media or air, given the HCG's near-wavelength period in this medium. Notably, only the 0th diffraction order, represented by plane waves, carries energy in both reflection and transmission, a crucial feature contributing to the HCG's extraordinary properties. Interestingly, if the two modes experience complete destructive interference at the HCG output plane, transmission vanishes, yielding 100% reflectivity. This intriguing phenomenon stems from the interference of the two waveguide-array modes at the HCG input and exit planes. Furthermore, this underscores that the HCG effect transcends mere grating or photonic crystal effects, as longitudinal HCGs, with beam propagation orthogonal to the periodicity direction, exhibit analogous behavior to transverse ones.

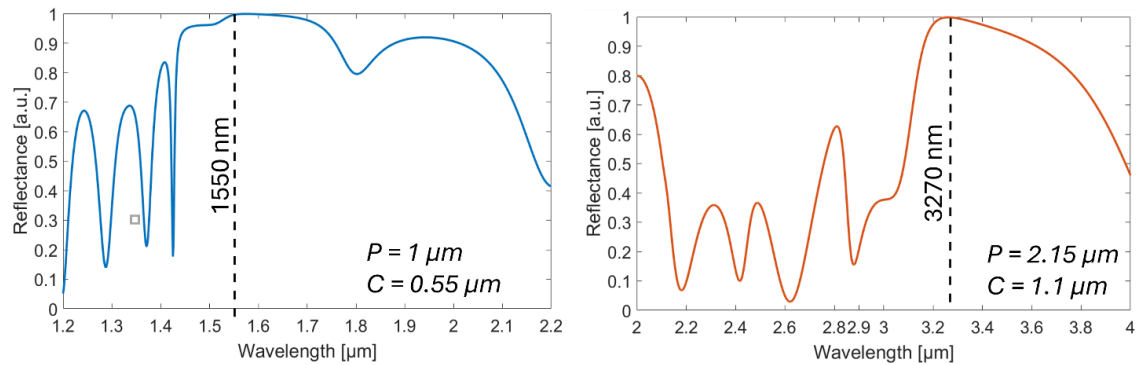


Figure 4.4: Reflectance spectra as a function of wavelength for a unit cell at a fixed period and duty cycle, (a) targeting 1550 nm and (b) targeting 3270 nm.

The unit cell has a fixed bulk silicon substrate with a thickness of 550  $\mu\text{m}$ , a 3  $\mu\text{m}$   $\text{SiO}_2$  layer on top, and a grating thickness of 220 nm. Figure 4.4 are the separate reflectance plots for the optimized design parameters that achieve ultra-high reflectance at the spectroscopically relevant wavelengths: 1550 nm (fixed period: 1  $\mu\text{m}$ , grating width: 0.55  $\mu\text{m}$ ) and 3270 nm (fixed period: 2.15  $\mu\text{m}$ , grating width: 1.1  $\mu\text{m}$ ), respectively. The achieved reflectance is more than 99.9%.

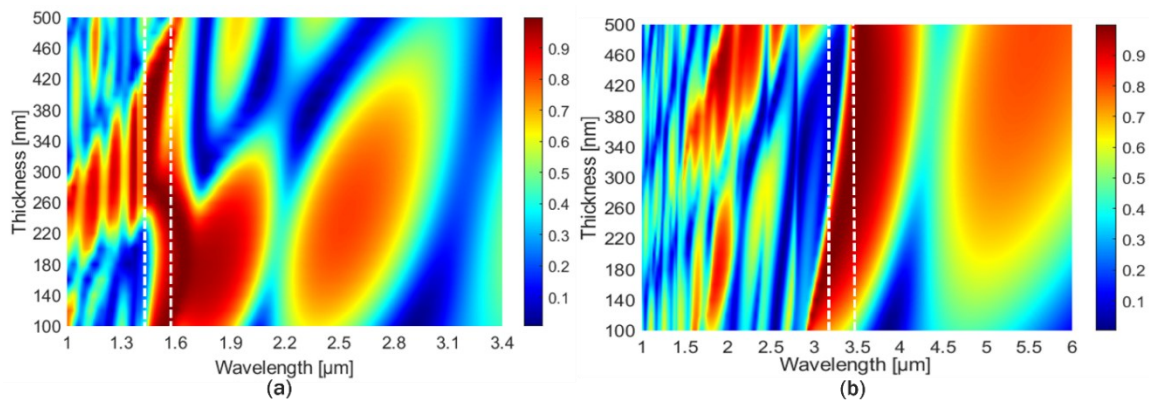


Figure 4.5: Reflectivity contour of HCGs as a function of wavelength and grating thickness, optimized for (a) 1550 nm (b) 3270 nm.

A numerical analysis was performed to examine how reflectance varies with wavelength for a range of thicknesses values for the grating structure. A strikingly orderly, checkered pattern is observed across both HCG cases upon plane wave incidence, influenced by wavelength and grating dimensions, exciting only a select few waveguide-array modes. The Figure 4.5 provided illustrates the substantial dependence on wavelength and HCG thickness ( $T$ ), emphasizing the interference effect. Notably, three distinct waveguide regimes emerge within the plotted data: the Deep Subwavelength Regime, Near-Wavelength Regime, and Diffraction Regime. As waves propagate through the HCG thickness, individual propagating waveguide-array

modes accrue distinct phases. Upon reaching the exit plane, a significant mismatch prompts reflection back to themselves and coupling into each other.

### 4.3 Design Principle of HCG-HCW

Figure 4.6 presents the schematic diagram of the HCG-HCW design, illustrating grating structures based on silicon configured parallel to the propagation direction of light (into the plane). These structures are situated on top of a silicon dioxide substrate, which, in turn, is placed on a silicon box wafer. The thickness of the grating elements is fixed at 220 nm. The design comprises two main sections: the uniform period structure section and the chirped grating section. In the uniform period structure section, the width of the grating structure is denoted as ' $C$ ', and the period of the uniform grating is represented by ' $P_{core}$ '. The number of uniform periods in this section is denoted as ' $N_{core}$ '. At the transition to the chirped section, the width of the grating is gradually varied from ' $W_f$ ' (initial width) to ' $W_i$ ' (final width), accompanied by a corresponding change in the period from ' $P_{chirp}$ '. The number of elements in this chirped section is denoted as ' $N_{chirp}$ '. The overall width of the substrate is represented by ' $W$ '. In simulation, a Gaussian beam is utilized to excite the HCG-HCW. The parameters of the Gaussian beam include length ( $G_L$ ) and width ( $G_W$ ).

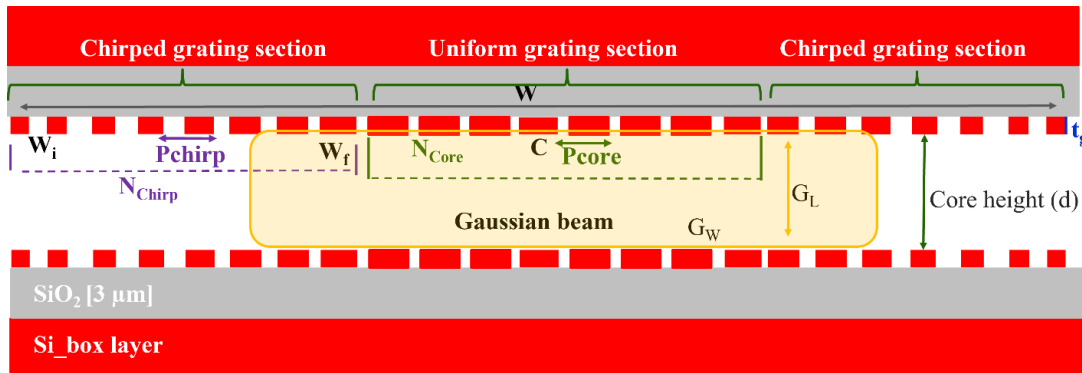


Figure 4.6: The cross schematic of a 2D HCG HCW, light propagates parallel grating bars. The core and cladding are defined by different HCG parameters to provide lateral confinement.

The theoretical framework underlying the propagation of optical beams through HCW involves guiding the beam through the air via multiple reflections in the cladding mirrors. The effective confinement of the optical beam within the core is primarily attributed to the constructive interference of multiple grating harmonics within a sub-wavelength periodic structure. This constructive interference pattern ensures that the optical beam remains confined within the core region, preventing its spread into the surrounding medium. The chirped section in the waveguide design serves a critical role in providing transverse confinement by inducing

a variation in the  $n_{eff}$ . This alteration in  $n_{eff}$  facilitates enhanced mode confinement within the HCW structure, contributing to improved light guidance and reduced propagation losses. Notably, in HCW<sub>2</sub>, optimized for operation at higher wavelengths, the overall width is nearly doubled compared to HCW<sub>1</sub>. This augmentation is necessitated by the absence of modes within a narrower width regime. For higher wavelength regimes, guided modes tend to exhibit larger spatial extents and require wider waveguide structures to accommodate their propagation.

Two optimized designs, designated as HCW<sub>1</sub> for 1550 nm wavelength and HCW<sub>2</sub> for 3.27  $\mu\text{m}$  wavelength, have been developed. For HCW<sub>1</sub>, key parameters include a core period ( $P_{core}$ ) of 1  $\mu\text{m}$ , grating element width ( $C_1$ ) of 0.5  $\mu\text{m}$ , and chirped grating period ( $P_{chirp}$ ) of 1  $\mu\text{m}$ . Additionally, the transition from uniform to chirped sections is governed by widths ( $W_f$ ,  $W_i$ ) of 0.5  $\mu\text{m}$  and 0.3, respectively. A total of 56 uniform periods ( $N_{core}$ ) and 20 chirped periods ( $N_{chirp}$ ) are employed, ensuring optimal light confinement. The dimensions of the HCW are characterized by a diameter ( $D$ ) of 6  $\mu\text{m}$ , Gaussian beam width ( $GW$ ) of 55  $\mu\text{m}$ , and length ( $GL$ ) of 5.2, within a substrate width ( $W$ ) of 100  $\mu\text{m}$ . Conversely, HCW<sub>2</sub>, optimized for 3.27  $\mu\text{m}$ , features parameters tailored to its longer wavelength. Parameters for HCW<sub>2</sub> include  $P_{core}$  of 2.15  $\mu\text{m}$ ,  $C_1$  of 1.55  $\mu\text{m}$ , and  $P_{chirp}$  of 2.15  $\mu\text{m}$ . Transition widths ( $W_f$ ,  $W_i$ ) are set at 1.55  $\mu\text{m}$  and 0.8, respectively, with 20 uniform periods ( $N_{core}$ ) and 33 chirped periods ( $N_{chirp}$ ). The HCW<sub>2</sub> dimensions comprise a diameter ( $D$ ) of 12  $\mu\text{m}$ , Gaussian beam width ( $G_w$ ) of 115  $\mu\text{m}$ , and length ( $GL$ ) of 8.3, within a substrate width ( $W$ ) of 226  $\mu\text{m}$ .

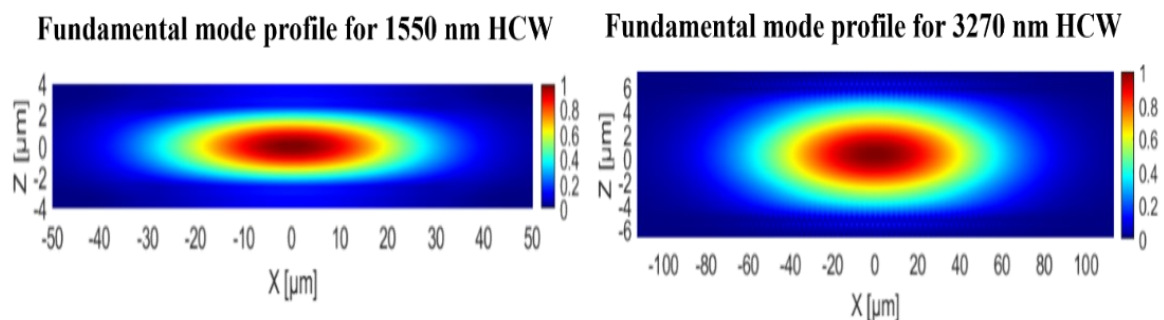


Figure 4.7: Computed fundamental mode profile of HCG-HCW optimized for 1550 nm and 3270 nm.

Figure 4.7 presents the mode profiles of both wavelengths, illustrating the spatial distribution of guided light within the (HCW), specifically showcasing the simulated mode profile of the fundamental mode for wavelengths 1550 nm and 3270 nm, respectively. For 1550 nm, the core width and the width of the chirped region are 56  $\mu\text{m}$  and 22  $\mu\text{m}$  on each side, respectively. In contrast, for 3270 nm, the core width and the width of the chirped region are 52  $\mu\text{m}$  and 85.8  $\mu\text{m}$  on each side, respectively. The excitation of these waveguides results in a  $n_{eff}$  of 0.9938 at

1550 nm wavelength and 0.9908 at 3270 nm wavelength. Importantly, this waveguide configuration ensures single-lateral mode operation.

To gain a comprehensive understanding of the relationship between the period and width of grating elements, Figure 4.8 provides an insightful depiction. In this representation, the plot focuses on 1000  $\mu\text{m}$  long HCWs. A discernible trend emerges, revealing that HCW<sub>1</sub> is notably more sensitive to variations in dimensions compared to HCW<sub>2</sub>. The optimized chosen grating element width ( $C$ ) is of 0.5 and a period ( $P$ ) of 1, aimed at a wavelength of 1.55  $\mu\text{m}$ . In Figure 4.8 (b), the grating element width selected ( $C$ ) is 1.55 and a period ( $P$ ) of 2.15, targeted at a wavelength of 3.27  $\mu\text{m}$ . This sensitivity characteristic is already elucidated through unit cell analysis, where these dimensions yield ultra-high reflectivity.

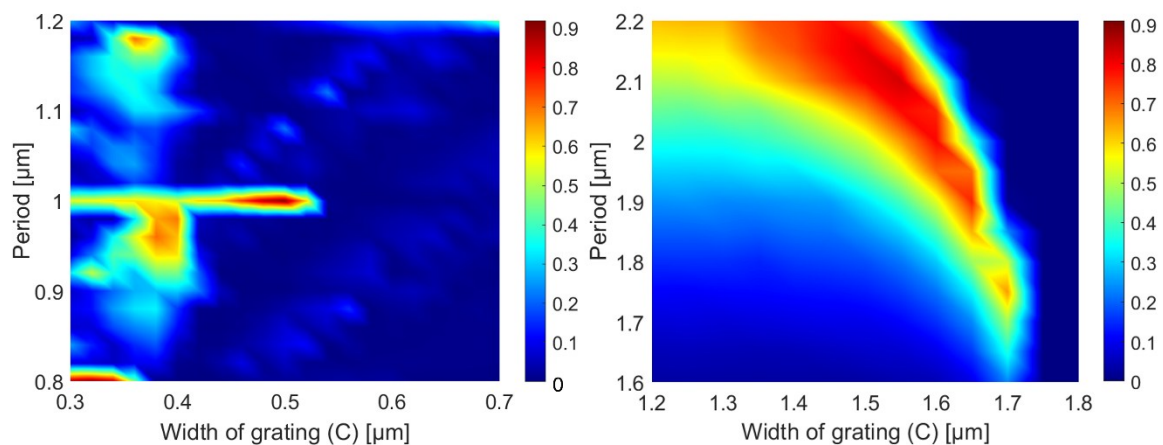


Figure 4.8: 3D reflectance color bar plot for  $p$  and  $c$ , optimized for wavelengths (a) 1550 nm and (b) 3270 nm.

Figure 4.9 (a) illustrates the loss in dB as a function of wavelength for the HCW<sub>1</sub> and HCW<sub>2</sub> designs. The lower X-axis represents wavelengths corresponding to HCW<sub>1</sub>, with a reference wavelength of 1550 nm where the loss is -0.458 dB. Conversely, the upper X-axis corresponds to wavelengths for HCW<sub>2</sub>, with a reference wavelength of 3270 nm where the loss is -0.410 dB. This ultra-low-loss characteristic is indicative of the excellent performance of both devices. Notably, HCW<sub>2</sub>, optimized for higher wavelength operation, exhibits a flat response across a wide range of wavelengths, indicating minimal variation in loss. In contrast, HCW<sub>1</sub> displays a more sensitive response to changes in wavelength, with loss values fluctuating more significantly, which is observed also in the unit cell section. Figure 4.9 (b) represents the optimized height of the core region for both HCW<sub>1</sub> and HCW<sub>2</sub> devices. In HCW<sub>1</sub>, the core height is optimized to be 6  $\mu\text{m}$ , whereas for HCW<sub>2</sub>, the core height is 12  $\mu\text{m}$ . Both devices exhibit a similar trend in core height optimization, showing an initial increase in light confinement as core height

increases and the need for a minimum threshold of height. However, beyond a certain threshold height, further increases in core height may not significantly improve light confinement.

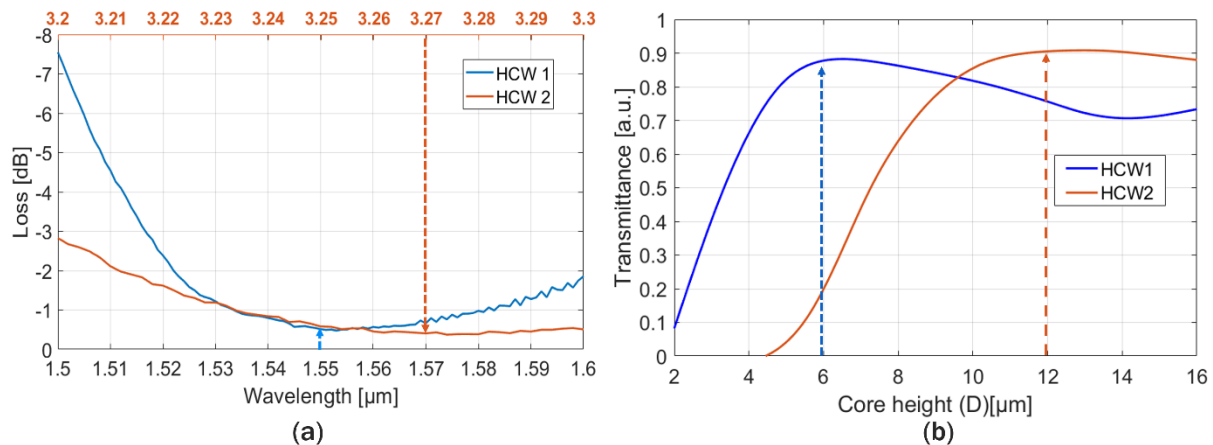


Figure 4.9: Depicts HCW over a 1 cm length of the waveguide, (a) loss spectrum of the plotted against wavelength and (b) the transmittance corresponding to distance between the two HCW chips (d).

To enhance the performance of HCWs incorporating HCGs, careful optimization of both the grating design and the waveguide geometry is essential. Such optimization enables reduced propagation losses, lower bending radii, and the possibility of extending the overall waveguide length without compromising transmittance. A critical factor in this design process is the chirping profile of the HCG. By varying the grating period along the propagation axis, light confinement and reflection characteristics can be finely tuned. In this study, different chirping profiles were analyzed, with a focus on a simple linear chirp applied after a uniform grating section. This approach demonstrated strong confinement properties while maintaining a straightforward implementation. One of the primary goals in engineering such structures is to broaden the low-loss operational bandwidth within the optical domain, a key requirement for practical on-chip photonic applications. The spectral position of this low-loss region can be precisely tuned by adjusting the grating parameters. This tuning capability stems from the resonance-based nature of HCGs, which rely on guided-mode resonance to achieve high reflectivity. However, due to their resonant behavior and the significant refractive index contrast between materials like silicon and air, these structures typically exhibit sharp spectral responses with limited bandwidth.

#### 4.4 Light Guiding in HCG-HCW Coupler

The optical functionality of HCWs is demonstrated, showing that light can remain guided through various coupler configurations using the sidewall-less HCW waveguides. Figure 4.10

illustrates the electric field distribution of HCW-based MMIs and DCs. By extending the waveguide width to accommodate multimode propagation, the number of grating elements increases to 200 for wavelength equals to 1550 nm design. A Gaussian beam is injected at the left corner of the MMI, where the self-imaging of the input mode is regenerated at a length of 2244  $\mu\text{m}$  for a general MMI. Similarly, for a symmetric MMI, the self-imaging occurs at 900  $\mu\text{m}$ . Additionally, in a 90  $\mu\text{m}$  wide HCW, a directional coupling mechanism is enhanced. The evanescent field extends into the adjacent waveguide through a two-sided chirped waveguide structure, enabling complete coupling of the input mode to the adjacent waveguide at a coupling length of 15300  $\mu\text{m}$ .

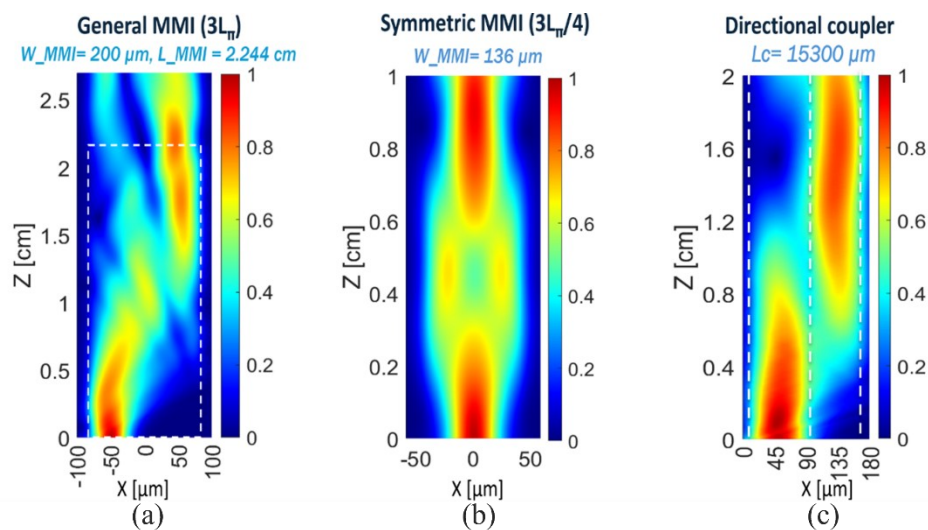


Figure 4.10: Electric field propagation profile of HCW based coupler (a) general MMI (b) symmetric MMI and (c) directional coupler.

These optical functions demonstrate the efficiency and operational flexibility of HCW as a versatile optical coupler, similar to conventional waveguide systems. Incorporating multiplexing and resonators within the HCW system can facilitate multi-gas sensing applications while significantly increasing the optical path length for enhanced light-matter interaction.

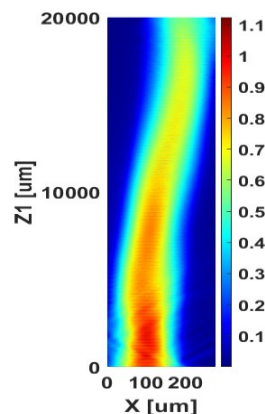


Figure 4.11: Electric field propagation profile of HCW for bend waveguide.

Light can also remain guided around curves using these sidewall-less waveguides. Figure 4.11 illustrates an S-bend curved HCW waveguide, demonstrating light propagation through the bend. When light is launched at the input power, 30% of the input power is observed at the output. In the bending section, the mode profile remains similar to that of a straight waveguide but shifts toward the waveguide edge farther from the center of the curvature. This behavior is comparable to that of a solid-core curved waveguide utilizing conventional index guiding. The loss for various bending radii has been extracted, and Figure 4.11 shows a 40  $\mu\text{m}$  lateral displacement from input to output for a 2000  $\mu\text{m}$ -long waveguide. These results indicate that the bending HCW structure is not ideal or is inherently limited for efficient waveguiding.

The demonstration of lateral confinement in planar HCG- HCW represents a pioneering strategy in waveguide engineering, utilizing surface phase manipulation. By maintaining a fixed thickness for the HCG while adjusting the periods and grating bar widths, diverse reflection phases can be generated while ensuring high reflectance. The HCW are specially designed to target gases of ammonia and methane at 1550 nm and 3270 nm. The effect of distance between the PIC platform is optimized to 6  $\mu\text{m}$  and 12  $\mu\text{m}$ , respectively. The device fabrication are ongoing with masked stepper photolithography. Achieving precise alignment is fundamental for the low loss light propagation, several characterization setup and alignment procedure are discussed in future and conclusion chapter. This compact and integration-friendly design holds great promises for enabling the development of portable, high-precision, and real-time multi-gas sensing devices for applications from industrial, agricultural to environmental monitoring.

# Chapter 5 - Future Work and Conclusion

This chapter outlines the ongoing development of three key research activities. The first section focuses on advances in duplexer development, aimed at integrating laser sources and a GRIN lens into a fully functional, ready-to-use device. This work supports the PASSEPARTOUT project's goal of developing portable smart sensing solutions. The second and third sections present numerical analysis followed by experimental characterization of HCG-HCW and Fabry-Perot resonators designed on a silicon metasurface. Finally, the conclusion discusses the ultimate goal of this thesis: developing a complete spectroscopic system integrating a multiplexer, on-chip lasers, and high-efficiency interaction pathways, such as HCG-HCWs.

## 5.1 Laser Integration a proof of principle

Building on the primary goal of this thesis to achieve low-cost, compact solution for multi-gas detection, two diode lasers are integrated into a DC-based duplexer chip. The optimized DC duplexer, with coupling length of  $640\ \mu\text{m}$  and gap  $275\ \text{nm}$ , was fabricated multiple times to optimize coupling efficiency. To have a uniform and precise facet the, chips were cleaved using laser dicing method. The chip was designed to accommodate both lasers and was subsequently bonded onto a glass substrate. A U-shaped chip was designed to accommodate both lasers and was subsequently bonded onto a glass substrate using a UV-curable adhesive. During integration, the  $1530\ \text{nm}$  laser chip was aligned first and its output power optimized before initiating the UV curing to secure it in place. The same procedure was followed for the  $1654\ \text{nm}$  laser. The contacts were wire-bonded using silver epoxy. Figure 5.1 (a) displays the laser duplexer edge, while Figure 5.1 (b) illustrates the fully integrated chip.

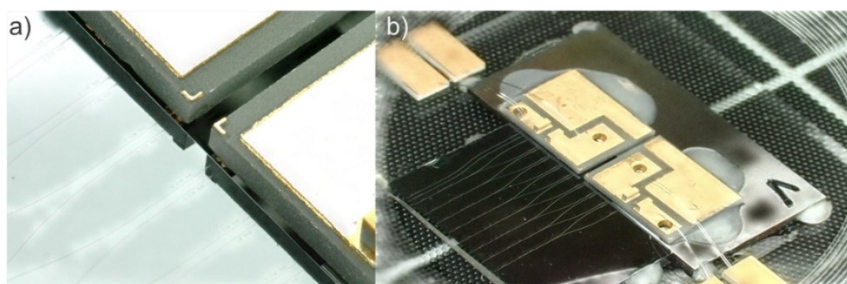


Figure 5.1: (a) Focus on the laser-chip coupling and (b) integrated duplexer device with electrical connections.

The measured output power is  $0.25\ \text{mW}$  (laser-chip-lens). The corresponding value for the bare laser was  $0.9\ \text{mW}$ , resulting in a high coupling efficiency of  $27.8\ \%$ . This efficiency is

consistent with the expected 3 dB losses from bare laser-chip coupling and the propagation losses. Moreover, the results agree with the 80% and 83% duplexer coupling efficiencies for wavelengths 1530 nm and 1654 nm, respectively. Table 5.1 summarizes the power measurements for dual-laser integration. A 1 mm GRIN lens is aligned on the second module to collimate the duplexer output beam. The beam images (Figure 5. 2) are obtained by alternating laser switching. An InGaAs camera is positioned 12 cm from the GRIN lens to capture these images.

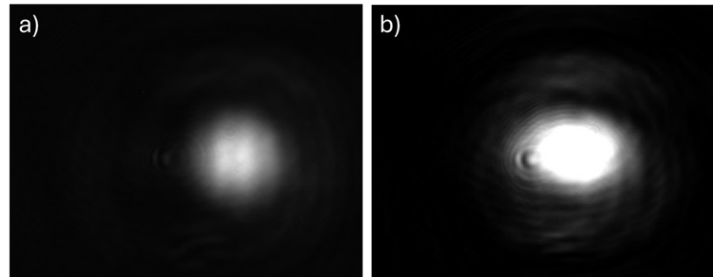


Figure 5. 2: InGaAs camera image of the collimated output beams at 12 cm for the (a) 1530 nm laser and (b) for the 1654 nm laser.

Table 5. 1: The output powers detected from the different integrated devices.

Laser Wavelength	Laser Power at 30mA [mW]	Power after chip integration [mW]	Laser-chip coupling efficiency [%]	Power output after GRIN lens [ $\mu$ W]
1530 nm	1.852	0.290	15.7	29
1654 nm	2.210	0.450	20.4	93

To integrate the third wavelength for carbon dioxide at 2003 nm, a triplexer configuration using cascaded directional couplers will be utilized. Integrating micro-lasers into multiplexers and seamlessly connecting photonic integrated circuits (PICs) to quartz tuning forks (QTFs) are critical steps toward a compact, portable, and cost-effective gas spectroscopy system. The system will first be validated using QEPAS in a controlled laboratory setup, with the ultimate goal of deploying drones for agricultural sensing of ammonia, methane, and carbon dioxide.

### 5.12 Expected sensitivity of duplexer device

For the 1530 nm laser, the output power increases from 1.825 mW at 30 mA to 12 mW at 110 mA. After passing through the duplexer, the output power is reduced to 0.29 mW at 30 mA and is calculated to be approximately 1.90 mW at 110 mA, based on the scaling factor (12/1.825). From literature the minimum detection limit (MDL) for ammonia is 449 ppb at an optical power of 35.2 mW [139]. Using this reference, the expected MDL for the 1530 nm

integrated PIC device is estimated by scaling the MDL to the lower duplexer power:  $(35.2 / 1.90) \times 449 \approx 8.32$  ppm. Similarly, for the 1654 nm laser, the output ranges from 2.21 mW at 30 mA to 15 mW at 110 mA. The corresponding duplexer output is 0.45 mW at 30 mA and calculated to be 3.05 mW at 110 mA. From literature, the MDL for methane is 0.76 ppm at 12 mW output power [140]. Scaling this to the integrated duplexer output, the expected MDL for the 1654 nm PIC device is  $(12 / 3.05) \times 0.76 \approx 3$  ppm. These results demonstrate the feasibility of achieving ppm-level detection sensitivity with integrated dual-laser photonic devices.

## 5.2 Characterization Techniques for HCW

The HCW, discussed in the preceding sections, is being fabricated using stepper photolithographic methods, which is suitable for large-area fabrication with a feature size of 0.6  $\mu\text{m}$ . The planar structure of the waveguide simplifies fabrication processes significantly. By maintaining a constant HCG thickness, it requires only single etching process. Although the waveguides presented here are composed of two separate pieces of HCG chips, serving as a proof-of-concept, monolithic integration can be achieved through flip-chip bonding or processing on a multi-stack silicon oxide wafer.

The silicon device layer thickness across the SOI wafer will be measured using an ellipsometer. The two pieces of patterned HCG chips will be meticulously mounted onto two translation stages. These translation stages enable precise control and alignment of the chips, facilitating the formation of the waveguide. Figure 5. 3 shows the characterization setup for HCW.

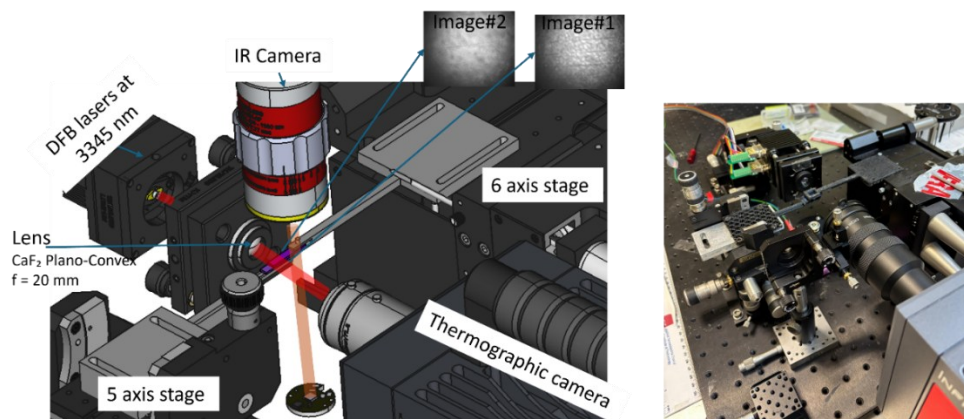


Figure 5. 3: (a)Schematic of characterization setup of HCW (b) Progressing HCW characterization setup.

The experimental validation of light guiding within the HCG - HCW will be conducted using a 3270 nm DFB laser beam. The beam will be focused through a Thorlabs CaF<sub>2</sub> plano-convex lens, which operates in the mid-IR range, onto the input facet of the HCW waveguide.

The intensity profile at the output facet will be measured using a similar lens. Before injecting light, the experimental setup requires a crucial alignment process between the two chips, which is fundamental for achieving low-loss HCW operation. The chip-to-chip alignment must be optimized in all degrees of freedom, including angle and facet positioning. Several alignment methods have been proposed, including alignment trenches incorporated during device fabrication. These trenches can be visualized using an output-side camera to distinguish the HCW and the confined mode. Since the operating wavelength is 3270 nm, a thermographic camera is used to detect the output mode and ensure proper alignment of the two grating edges. Additionally, to fine-tune the angle and distance between the two chips, a 1550 nm LED is passed from beneath the chips and captured using an objective lens and a fixed camera. Different images of the sample can be obtained at various metasurface planes, enabling precise adjustments of the angle and spacing between the chips.

The alignment method includes using a metasurface-based Fabry-Perot (FP) resonator as a sensing device. When light is launched from one surface of the device to the other, it undergoes multiple reflections within the cavity, forming a FP resonance. The transmitted output spectrum exhibits characteristic transmission peaks, and the free spectral range (FSR) can be utilized to determine the cavity length, which corresponds to the distance between the two chips.

### **5.3 Design of a Metasurface Based FP Cavity**

Ultra-high reflecting surfaces are ideal for FP based gas sensing applications [141], [142]. This future work section focuses on the design of an HCG-based FP resonator, with applications aimed at enhancing acoustic wave detection in QEPAS systems. The designs proposed for future work are specifically tailored for detecting methane gas, which exhibits a strong absorption peak at 3270 nm. Integrated photonic chip-based FP resonators are typically based on BDR. However, their fabrication involves multiple layers and integrating them with QTF presents significant challenges. To overcome these limitations, the designed metasurface is engineered as an ultra-high-reflecting FP resonator.

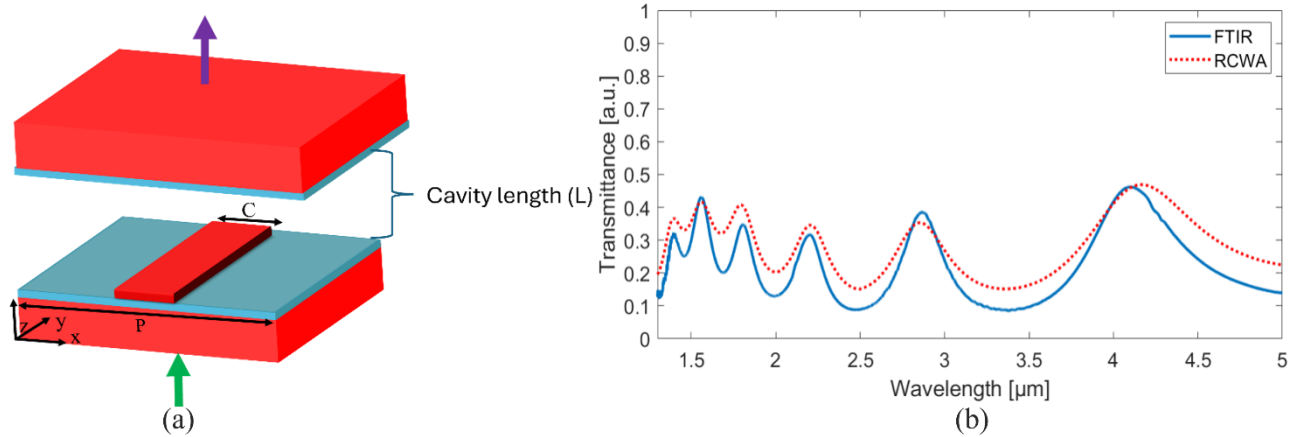


Figure 5. 4: (a) Two surface grating unit cells (b) Comparison of RCWA to FTIR for plane 220 nm silicon layer without grating structures.

The metasurface design is realized using the RCWA method for a FP unit cell. The structure follows a 1D periodic configuration, optimized to function as a FP cavity. A plane wave scan is performed for different wavelengths at two surfaces of the unit cell, corresponding to a cavity length  $L$ . The structural design and its configuration are illustrated in Figure 5. 4 (a). The designed metasurface is similar to the one used in chapter 4 for HCW. An FTIR scan for the plane silicon of 220 nm without grating structure is used to validate the performance of RCWA method. And it is well in agreement, as shown in Figure 5. 4 (b).

Transmission through the cavity was evaluated by launching a broadband wavelength range from the first metasurface to the second, across varying cavity lengths. The resulting resonance peaks, shown in Figure 5. 5 for cavity lengths of 100  $\mu\text{m}$  and 500  $\mu\text{m}$ , demonstrate how the free spectral range (FSR) decreases as the cavity length increases. Additionally, the quality factor (Q-factor) and finesse of the FP resonator designs were calculated. The Q-factor reaches values up to  $10^4$ , with a corresponding finesse of 560, indicating the high performance and tunability of the metasurface-based FP cavities. The  $P$  and  $C$  of the grating structure are identical to those used in the HCW, specifically 2.1  $\mu\text{m}$  and 1.0  $\mu\text{m}$ , respectively. The drop in transmission at the center of the stopband is due to its extremely narrow bandwidth, which exceeds the resolution of the computational mesh.

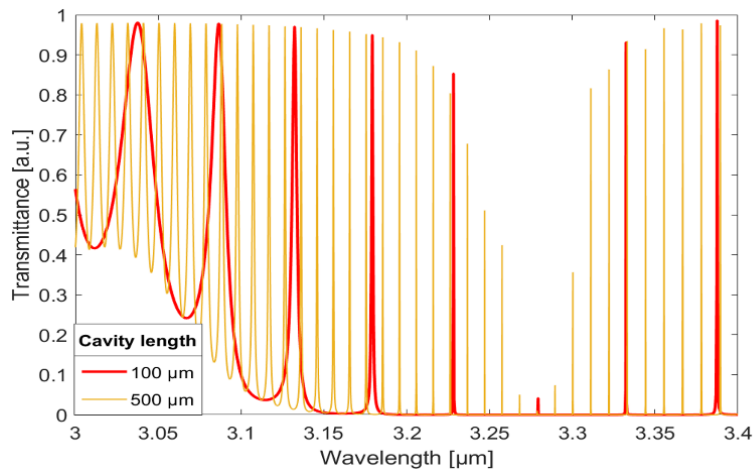


Figure 5. 5: Simulation results of resonance peaks of FP, designed to target 3270 nm for various cavity lengths.

To further develop the design for FP characterization, a laser-diced silicon spacer can be used[143]. However, bumps often form at the edges of the spacer during the dicing process. At this stage, a SEM image is taken to analyze the surface morphology. To ensure a smooth and uniform spacer surface for maintaining a constant cavity length, the spacer undergoes a grinding and polishing process. As one side of the silicon wafer is already polished, a grinding step is initiated for the other side, with 10 minutes at high speed of 50 rpm, and then 5 minutes of medium speed of 30 rpm to achieve better finishing. Initially, 1  $\mu\text{m}$  alumina was observed in the SEM image; however, after the final polishing stage alumina is decreased to 0.2  $\mu\text{m}$ , with improved surface quality. The post-polishing SEM image is shown in Figure 5. 6, demonstrating the improved surface quality.

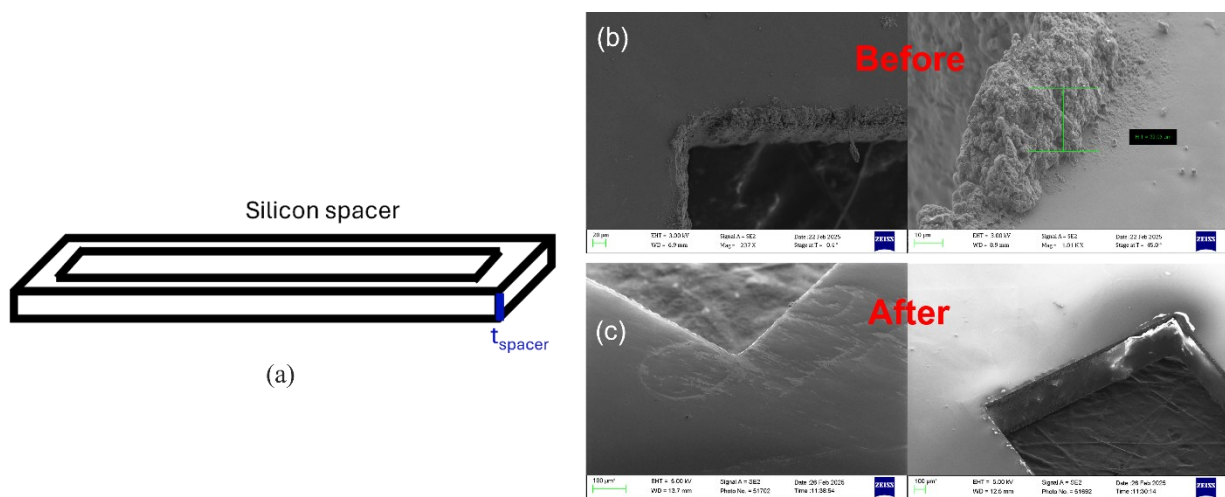


Figure 5. 6: (a) Design of spacer for FP with thickness ( $t_{\text{spacer}}$ ). (b) SEM image of laser diced silicon spacer (a) before polishing (b) after polishing.

This configuration not only serves as an alignment method for HCWs but also enhances the sensitivity of gas sensors on its own. Future work requires a precision characterization setup with high-resolution alignment capabilities, which is crucial for forming a stable FP cavity, given the wavelength sensitivity of HCG structures. After fabrication via stepper photolithography, the HCG metasurface should be characterized using FTIR to optimize the grating parameters for the target wavelength. Subsequently, two samples are bounded with varying spacer thicknesses ( $t_{spacer}$ ), as illustrated in Figure 5. 6 (a). A broadband light source is then passed through the cavity, and the resulting spectrum is collected using an OSA. A resonant optical power buildup inside a high-finesse cavity is used to increase the sensitivity of QEPAS for detecting CO, N<sub>2</sub>O, and H<sub>2</sub>O at a wavelength of 4.59 μm [144]. Compared to conventional QEPAS systems, a metasurface-based FP cavity can provide a compact, portable design with high finesse, leading to significantly enhanced detection sensitivity.

## 5.4 Conclusion

PICs have become incredibly important because of their wide-ranging applications in communication systems, biosensing, and spectroscopy. This thesis describes the design, fabrication, and characterization of PICs based on Si<sub>3</sub>N<sub>4</sub> multiplexers and silicon metasurfaces. The overall target of the thesis is to develop integrated, low-cost and portable multi-gas sensors. The main outcomes of this research are briefly summarized in the following paragraphs.

- A high-performance duplexer based on an on-chip angled MMI configuration was designed and characterized for specific wavelength pairs: 1530–1653.7 nm, 1530–1684 nm, and 1530–2003 nm. The coupling efficiencies were numerically evaluated for various mode profiles, including fundamental, higher-order, and realistic diode-laser modes, across all target wavelengths. Experimental results demonstrate a clear improvement in coupling efficiency, with measured values of 74% at 1530 nm and 80% at 1653.7 nm.
- A compact, DC-based duplexer demonstrated a higher output-power coupling ratio when combining 1530 nm and 1653.7 nm. Coupling efficiencies were thoroughly examined and validated for fundamental, higher-order, and realistic diode-laser modes. Numerical evaluation yield coupling efficiencies of 96%:96% for fundamental modes and 78%:81% for commercially available laser modes. Coupling efficiencies up to 73% (1530 nm) and 77% (1653.7 nm) were experimentally measured. Repeated fabrication and precise laser dicing further improved efficiencies to 85% and 88%, respectively.
- To incorporate a third wavelength corresponding to carbon dioxide, a triplexer based on a cascaded DC structure was extensively investigated. This design offers improved power coupling ratios tailored for the absorption wavelengths of ammonia ( $\lambda_{NH_3}=1530$  nm), methane ( $\lambda_{CH_4}=1653.7$  nm) and carbon dioxide ( $\lambda_{CO_2}=2003$  nm). Various coupler configurations were evaluated, considering both bend and coupling losses. Numerical simulations showed high coupling efficiencies for the fundamental modes: 90% at  $\lambda_{NH_3}$ , 91% at  $\lambda_{CH_4}$ , and 88% at  $\lambda_{CO_2}$ . Experimental measurements further validated these findings, demonstrating coupling efficiencies of 82% at  $\lambda_{NH_3}$ , 73% at  $\lambda_{CH_4}$ , and 91% at  $\lambda_{CO_2}$ .
- The use of the Duplexer or Triplexer will allow a single spectroscopy system to detect multiple gases, eliminating the need for multiple single-wavelength systems. Following the implementation of semi-integration architectures of Si<sub>3</sub>N<sub>4</sub> chip with QTF, the DC-

based duplexer has been successfully combined with laser and GRIN lens components, resulting in a ready-to-use gas sensing module. These improvements are essential for increasing sensitivity and selectivity in multi-gas detection applications.

- Numerical and experimental analyses confirm the effectiveness of the SP-SMF structure for refractive index sensing of analytes such as air, water, and isopropanol. A dedicated experimental setup was developed to validate simulation results, demonstrating strong agreement. This approach highlights SP-SMF's potential as a sensing platform. Future work may optimize core size, taper dimensions, and sensing region design to further enhance performance.
- The effective interaction of the SPF for water vapor and methane gas have been demonstrated, using LITES method. A strict increment in signals is observed when the SPF is exposed to air and 1 % methane. A repeatable signal increase of  $3.9 \times 10^{-4}$  ( $1.5 \times 10^{-4}$  mV) was observed for water vapor (methane), attributed to evanescent field interaction over a 17 mm polished region, confirming effective gas molecule interaction. The setup has applications in remote sensing, where light is carried through fiber to distant areas, allowing for sensing to be performed from a far and harsh environment.
- TLF was employed in QEPAS and LITES techniques to enhance integration and interaction path length for small-volume detection. This configuration enabled ppm-level detection of water vapor in indoor environments, with optimized sensor positioning ensuring stable and precise performance. The system offers sufficient sensitivity to monitor atmospheric water vapor. By eliminating free-space alignment challenges, the TLF-based approach simplifies integration and improves overall sensitivity.
- Successfully demonstrated a proof-of-concept for a novel semi-integrated optical gas sensing architecture that combines a  $\text{Si}_3\text{N}_4$  waveguide with a low-frequency, T-shaped, and custom-designed QTF. The ability of the developed system to operate with both QEPAS and LITES techniques using minimal optical power ( $\sim 300 \mu\text{W}$ ) while maintaining comparable performance (SNRs of 1.6-3.2) for water vapor detection in a laboratory environment. The successful integration of photonic and piezoelectric components represents a significant step toward miniaturized gas sensors. The compact nature of this architecture also suggests potential for multiplexed sensing by integrating multiple waveguide structures and integrated laser sources on a single chip.
- An innovative approach to confining waves in planar HCG-HCW, design achieves a surface that reflects waves effectively while maintaining a structure that allows for high

transmission. The unique side-open waveguide system also allows gas to flow through the sidewalls, making it suitable for gas spectroscopic techniques. The HCW design is specifically tailored for methane gas sensing at a wavelength of  $3.27 \mu\text{m}$ . Numerical analysis shows that the transmittance can reach up to  $-0.41 \text{ dB}$ . These findings demonstrate the potential of high-transmitting hollow-core waveguides for gas sensing, highlighting the effectiveness and cost-efficiency of chip-scale photonic integration. Various coupler configurations of the HCW were numerically validated for both MMI and DC designs, confirming efficient light guidance through a sidewall-less structure.

- The silicon metasurface was numerically validated for optimizing an HCG-based FP structure. Preliminary characterization using the RCWA method showed good agreement with a non-grating structure using FTIR method. The grating period and width were numerically optimized to  $2.1 \mu\text{m}$  and  $1.0 \mu\text{m}$ , respectively, achieving a Q-factor of  $10^4$  and FSR of  $0.01 \text{ nm}$  for a cavity length of  $500 \mu\text{m}$ .

# Reference

- [1] H. Lin *et al.*, “Mid-infrared integrated photonics on silicon: a perspective,” vol. 7, no. 2, pp. 393–420, 2018, doi: doi:10.1515/nanoph-2017-0085.
- [2] P. Muñoz *et al.*, “Silicon Nitride Photonic Integration Platforms for Visible, Near-Infrared and Mid-Infrared Applications,” *Sensors*, vol. 17, no. 9, 2017, doi: 10.3390/s17092088.
- [3] W. Xiong, G. Wang, J. Li, C. Zhao, W. Wang, and H. H. Radamson, “SiN-based platform toward monolithic integration in photonics and electronics,” *Journal of Materials Science: Materials in Electronics*, vol. 32, no. 1, pp. 1–18, 2021, doi: 10.1007/s10854-020-04909-z.
- [4] T. Sharma *et al.*, “Review of Recent Progress on Silicon Nitride-Based Photonic Integrated Circuits,” *IEEE Access*, vol. 8, pp. 195436–195446, Jan. 2020, doi: 10.1109/ACCESS.2020.3032186.
- [5] P. Najafi and A. Ghaemi, “Chemiresistor gas sensors: Design, Challenges, and Strategies: A comprehensive review,” *Chemical Engineering Journal*, vol. 498, p. 154999, 2024, doi: <https://doi.org/10.1016/j.cej.2024.154999>.
- [6] J. Baranwal, B. Barse, G. Gatto, G. Broncová, and A. Kumar, “Electrochemical Sensors and Their Applications: A Review,” *Chemosensors*, vol. 10, Apr. 2022, doi: 10.3390/chemosensors10090363.
- [7] X. Liu, S. Cheng, H. Liu, S. Hu, D. Zhang, and H. Ning, “A Survey on Gas Sensing Technology,” *Sensors*, vol. 12, no. 7, pp. 9635–9665, 2012, doi: 10.3390/s120709635.
- [8] J. Bak and S. Clausen, “FTIR emission spectroscopy methods and procedures for real time quantitative gas analysis in industrial environments,” *Meas Sci Technol*, vol. 13, no. 2, p. 150, 2002, doi: 10.1088/0957-0233/13/2/302.
- [9] M. Nikodem, “Laser-Based Trace Gas Detection inside Hollow-Core Fibers: A Review,” *Materials (Basel)*, vol. 13, Apr. 2020, doi: 10.3390/ma13183983.
- [10] W. Zeller, L. Naehle, P. Fuchs, F. Gerschuetz, L. Hildebrandt, and J. Koeth, “DFB Lasers Between 760 nm and 16  $\mu$ m for Sensing Applications,” *Sensors*, vol. 10, no. 4, pp. 2492–2510, 2010, doi: 10.3390/s100402492.
- [11] Y. Ma *et al.*, “Ultra-high sensitive trace gas detection based on light-induced thermoelastic spectroscopy and a custom quartz tuning fork,” *Appl Phys Lett*, vol. 116, no. 1, Jan. 2020, doi: 10.1063/1.5129014.
- [12] S. Dello Russo *et al.*, “Light-induced thermo-elastic effect in quartz tuning forks exploited as a photodetector in gas absorption spectroscopy,” *Opt Express*, vol. 28, no. 13, p. 19074, Jun. 2020, doi: 10.1364/OE.393292.
- [13] Y. Pan, J. Zhao, P. Lu, C. Sima, and D. Liu, “Recent Advances in Light-Induced Thermoelastic Spectroscopy for Gas Sensing: A Review,” *Remote Sens (Basel)*, vol. 15, no. 1, p. 69, Dec. 2022, doi: 10.3390/rs15010069.

- [14] J. Sun, J. Chang, C. Wang, and J. Shao, "Tunable diode laser absorption spectroscopy for detection of multi-component gas: a review," *Appl Spectrosc Rev*, vol. 59, no. 8, pp. 1086–1107, Sep. 2024, doi: 10.1080/05704928.2024.2302608.
- [15] K. Okamoto, "Chapter 7 - Beam propagation method," in *Fundamentals of Optical Waveguides (Second Edition)*, Second Edition., K. Okamoto, Ed., Burlington: Academic Press, 2006, pp. 329–397. doi: <https://doi.org/10.1016/B978-012525096-2/50008-8>.
- [16] G. R. Hadley, "Wide-angle beam propagation using Padé approximant operators," *Opt. Lett.*, vol. 17, no. 20, pp. 1426–1428, Oct. 1992, doi: 10.1364/OL.17.001426.
- [17] M. Veettikazhy *et al.*, "BPM-Matlab: an open-source optical propagation simulation tool in MATLAB," *Opt. Express*, vol. 29, no. 8, pp. 11819–11832, Apr. 2021, doi: 10.1364/OE.420493.
- [18] D. Yevick and B. Hermansson, "Efficient beam propagation techniques," *IEEE J Quantum Electron*, vol. 26, no. 1, pp. 109–112, 1990, doi: 10.1109/3.44923.
- [19] "Synopsys inc., rsoft products," <https://www.synopsys.com>."
- [20] K. Knop, "Rigorous diffraction theory for transmission phase gratings with deep rectangular grooves," *J. Opt. Soc. Am.*, vol. 68, no. 9, pp. 1206–1210, Sep. 1978, doi: 10.1364/JOSA.68.001206.
- [21] M. G. Moharam and T. K. Gaylord, "Rigorous coupled-wave analysis of planar-grating diffraction," *J. Opt. Soc. Am.*, vol. 71, no. 7, pp. 811–818, Jul. 1981, doi: 10.1364/JOSA.71.000811.
- [22] Ph. Lalanne, M. S. L. Lee, J. C. Rodier, P. Chavel, E. Cambril, and Y. Chen, "Imaging with blazed-binary diffractive elements," in *Diffractive Optics and Micro-Optics*, Optica Publishing Group, 2002, p. DThA2. doi: 10.1364/DOMO.2002.DThA2.
- [23] E. Popov and M. Nevière, "Maxwell equations in Fourier space: fast-converging formulation for diffraction by arbitrary shaped, periodic, anisotropic media," *J. Opt. Soc. Am. A*, vol. 18, no. 11, pp. 2886–2894, Nov. 2001, doi: 10.1364/JOSAA.18.002886.
- [24] C. Baudot *et al.*, "Developments in 300nm silicon photonics using traditional CMOS fabrication methods and materials," *2017 IEEE International Electron Devices Meeting (IEDM)*, pp. 34.3.1-34.3.4, 2017, [Online]. Available: <https://api.semanticscholar.org/CorpusID:1032433>
- [25] S. Iadanza, G. C. R. Devarapu, A. Blake, P. A. Alba, J.-M. Pardini, and L. O'Faolain, "Polycrystalline silicon PhC cavities for CMOS on-chip integration," *Sci Rep*, vol. 12, no. 1, p. 17097, 2022, doi: 10.1038/s41598-022-21578-6.
- [26] B. Shi, Z. Zhou, Y. Chen, X. Wang, and B. Xu, "Preparation and properties of hydrophobic and highly transparent SiO<sub>2</sub> aerogels," *Ceram Int*, vol. 49, no. 16, pp. 27597–27603, 2023, doi: <https://doi.org/10.1016/j.ceramint.2023.06.040>.
- [27] B. W. M. Moeskops, S. M. Cristescu, and F. J. M. Harren, "Sub-part-per-billion monitoring of nitric oxide by use of wavelength modulation spectroscopy in combination with a thermoelectrically cooled, continuous-wave quantum cascade laser," *Opt. Lett.*, vol. 31, no. 6, pp. 823–825, Mar. 2006, doi: 10.1364/OL.31.000823.
- [28] D. S. Bomse, A. C. Stanton, and J. A. Silver, "Frequency modulation and wavelength modulation spectroscopies: comparison of experimental methods using a lead-salt diode laser," *Appl. Opt.*, vol. 31, no. 6, pp. 718–731, Feb. 1992, doi: 10.1364/AO.31.000718.

- [29] M. D. Wojcik, M. C. Phillips, B. D. Cannon, and M. S. Taubman, "Gas-phase photoacoustic sensor at 8.41  $\mu\text{m}$  using quartz tuning forks and amplitude-modulated quantum cascade lasers," *Applied Physics B*, vol. 85, no. 2, pp. 307–313, 2006, doi: 10.1007/s00340-006-2394-8.
- [30] S. Dello Russo *et al.*, "Quartz-enhanced photoacoustic spectroscopy exploiting low-frequency tuning forks as a tool to measure the vibrational relaxation rate in gas species," *Photoacoustics*, vol. 21, p. 100227, 2021, doi: <https://doi.org/10.1016/j.pacs.2020.100227>.
- [31] M. Olivieri *et al.*, "Assessment of vibrational-translational relaxation dynamics of methane isotopologues in a wet-nitrogen matrix through QEPAS," *Photoacoustics*, vol. 31, p. 100518, 2023, doi: <https://doi.org/10.1016/j.pacs.2023.100518>.
- [32] A. Zifarelli *et al.*, "Multi-gas quartz-enhanced photoacoustic sensor for environmental monitoring exploiting a Vernier effect-based quantum cascade laser," *Photoacoustics*, vol. 28, p. 100401, 2022, doi: <https://doi.org/10.1016/j.pacs.2022.100401>.
- [33] W. Feng, Y. Qu, Y. Gao, and Y. Ma, "Advances in fiber-based quartz enhanced photoacoustic spectroscopy for trace gas sensing," *Microw Opt Technol Lett*, vol. 63, no. 8, pp. 2031–2039, 2021, doi: <https://doi.org/10.1002/mop.32841>.
- [34] P. H. Paul and G. Kychakoff, "Fiber-optic evanescent field absorption sensor," *Appl Phys Lett*, vol. 51, no. 1, pp. 12–14, Jul. 1987, doi: 10.1063/1.98888.
- [35] C. Pendão and I. Silva, "Optical Fiber Sensors and Sensing Networks: Overview of the Main Principles and Applications," *Sensors*, vol. 22, no. 19, 2022, doi: 10.3390/s22197554.
- [36] A. Annunziato, F. Anelli, P. L. P. Du Teilleul, S. Cozic, S. Poulain, and F. Prudenziario, "Fused optical fiber combiner based on indium fluoride glass: perspectives for mid-IR applications," *Opt. Express*, vol. 30, no. 24, pp. 44160–44174, Nov. 2022, doi: 10.1364/OE.471090.
- [37] Y. Luo, Y. Yu, M. Ye, C. Sun, and X. Zhang, "Integrated dual-mode 3 dB power coupler based on tapered directional coupler," *Sci Rep*, vol. 6, no. 1, p. 23516, 2016, doi: 10.1038/srep23516.
- [38] R. Marchetti, C. Lacava, L. Carroll, K. Gradkowski, and P. Minzioni, "Coupling strategies for silicon photonics integrated chips [Invited]," *Photonics Res*, 2019.
- [39] Y. Hu, R. M. Jenkins, F. Y. Gardes, E. D. Finlayson, G. Z. Mashanovich, and G. T. Reed, "Wavelength division (de)multiplexing based on dispersive self-imaging," *Opt. Lett.*, vol. 36, no. 23, pp. 4488–4490, Dec. 2011, doi: 10.1364/OL.36.004488.
- [40] L.-W. Chung, S.-L. Lee, and Y.-J. Lin, "Principles and application of reduced beat length in MMI couplers," *Opt. Express*, vol. 14, no. 19, pp. 8753–8764, Sep. 2006, doi: 10.1364/OE.14.008753.
- [41] M. Paparella *et al.*, "Analysis of the Optical Coupling Between GaSb Diode Lasers and Passive Waveguides: A Step Toward Monolithic Integration on Si Platforms," *IEEE Photonics J*, vol. 14, no. 5, pp. 1–6, 2022, doi: 10.1109/JPHOT.2022.3203593.
- [42] H. R. Philipp, "Optical Properties of Silicon Nitride," *J Electrochem Soc*, vol. 120, no. 2, p. 295, Feb. 1973, doi: 10.1149/1.2403440.
- [43] I. H. Malitson, "Interspecimen Comparison of the Refractive Index of Fused Silica,†," *J. Opt. Soc. Am.*, vol. 55, no. 10, pp. 1205–1209, Oct. 1965, doi: 10.1364/JOSA.55.001205.
- [44] P. Saha, M. S. Rasel, and K. T. Ahmmed, "A review of higher-order mode pass filtering techniques," *Heliyon*, vol. 8, no. 11, p. e11705, 2022, doi: <https://doi.org/10.1016/j.heliyon.2022.e11705>.

- [45] A. Thottoli *et al.*, “Design and Fabrication of Angled MMI-Based Duplexer for Sensing Applications,” in *2023 Conference on Lasers and Electro-Optics Europe & European Quantum Electronics Conference (CLEO/Europe-EQEC)*, 2023, p. 1. doi: 10.1109/CLEO/Europe-EQEC57999.2023.10232273.
- [46] J. Mu, S. A. Vázquez-Córdova, M. A. Sefunc, Y.-S. Yong, and S. M. García-Blanco, “A Low-Loss and Broadband MMI-Based Multi/Demultiplexer in Si<sub>3</sub>N<sub>4</sub>/SiO<sub>2</sub> Technology,” *Journal of Lightwave Technology*, vol. 34, no. 15, pp. 3603–3609, 2016, doi: 10.1109/JLT.2016.2578463.
- [47] H. Li, X. Dong, E. Li, Z. Liu, and Y. Bai, “Design Optimization and Comparative Analysis of Silicon-Nanowire-Based Couplers,” *IEEE Photonics J*, vol. 4, pp. 2017–2026, 2012, [Online]. Available: <https://api.semanticscholar.org/CorpusID:44226439>
- [48] S. Hassan and D. Chack, “Design and analysis of polarization independent MMI based power splitter for PICs,” *Microelectronics J*, vol. 104, p. 104887, 2020, doi: <https://doi.org/10.1016/j.mejo.2020.104887>.
- [49] J.-K. Hong and S.-S. Lee, “PLC-Based Novel Triplexer With a Simple Structure for Optical Transceiver Module Applications,” *IEEE Photonics Technology Letters*, vol. 20, no. 1, pp. 21–23, 2008, doi: 10.1109/LPT.2007.911006.
- [50] H. Khalilzadeh, A. Bahrami, and H. Badri Ghavifekr, “MMI-based all-optical four-channel wavelength division demultiplexer,” *Photonic Network Communications*, vol. 36, no. 2, pp. 217–223, 2018, doi: 10.1007/s11107-018-0771-y.
- [51] F. Wang, X. Xu, C. Sun, and J. Zhao, “Ultracompact 1310/1550 nm wavelength demultiplexer based on subwavelength grating-assisted multimode interference coupler,” *Optical Engineering*, vol. 60, Nov. 2021, doi: 10.1117/1.OE.60.8.087104.
- [52] J. Menahem and D. Malka, “1 × 4 Wavelength Demultiplexer C-Band Using Cascaded Multimode Interference on SiN Buried Waveguide Structure,” *Materials*, vol. 15, no. 14, 2022, doi: 10.3390/ma15145067.
- [53] R. K. Gupta, S. Chandran, and B. K. Das, “Wavelength-Independent Directional Couplers for Integrated Silicon Photonics,” *Journal of Lightwave Technology*, vol. 35, no. 22, pp. 4916–4923, 2017, doi: 10.1109/JLT.2017.2759162.
- [54] Y. Akihama and K. Hane, “Single and multiple optical switches that use freestanding silicon nanowire waveguide couplers,” *Light Sci Appl*, vol. 1, no. 6, pp. e16–e16, 2012, doi: 10.1038/lsa.2012.16.
- [55] J. H. Song *et al.*, “Angled-MMI-based wavelength splitters on silicon nitride waveguide platforms for fluorescence sensing,” *Appl. Opt.*, vol. 56, no. 29, pp. 8055–8060, Oct. 2017, doi: 10.1364/AO.56.008055.
- [56] H. F. Talbot, “LXXVI. Facts relating to optical science. No. IV,” *Philosophical Magazine Series 1*, vol. 4, pp. 112–114, 1834, [Online]. Available: <https://api.semanticscholar.org/CorpusID:124078504>
- [57] L. B. Soldano and E. C. M. Pennings, “Optical multi-mode interference devices based on self-imaging: principles and applications,” *Journal of Lightwave Technology*, vol. 13, no. 4, pp. 615–627, 1995, doi: 10.1109/50.372474.

- [58] T. D. Bucio, A. Z. Khokhar, G. Z. Mashanovich, and F. Y. Gardes, "N-rich silicon nitride angled MMI for coarse wavelength division (de)multiplexing in the O-band," *Opt. Lett.*, vol. 43, no. 6, pp. 1251–1254, Mar. 2018, doi: 10.1364/OL.43.001251.
- [59] K. Luke, Y. Okawachi, M. R. E. Lamont, A. L. Gaeta, and M. Lipson, "Broadband mid-infrared frequency comb generation in a Si<sub>3</sub>N<sub>4</sub> microresonator," *Opt. Lett.*, vol. 40, no. 21, pp. 4823–4826, Nov. 2015, doi: 10.1364/OL.40.004823.
- [60] X. Jiang, H. Wu, and D. Dai, "Low-loss and low-crosstalk multimode waveguide bend on silicon," *Opt Express*, vol. 26, p. 17680, Jun. 2018, doi: 10.1364/OE.26.017680.
- [61] M. Pollock Clifford R. and Lipson, "Introduction and Overview," in *Integrated Photonics*, Boston, MA: Springer US, 2003, pp. 1–7. doi: 10.1007/978-1-4757-5522-0\_1.
- [62] D. Lv, L. Wu, C. Liu, A. Li, R. Wang, and A. Wu, "Broadband and Low-Loss Silicon Photonic Directional Coupler for Signal Power Tapping on the 3  $\mu\text{m}$  SOI Waveguide Platform," *Photonics*, vol. 10, no. 7, 2023, doi: 10.3390/photonics10070776.
- [63] G. F. R. Chen, J. R. Ong, T. Y. L. Ang, S. T. Lim, C. E. Png, and D. T. H. Tan, "Broadband Silicon-On-Insulator directional couplers using a combination of straight and curved waveguide sections," *Sci Rep*, vol. 7, no. 1, p. 7246, 2017, doi: 10.1038/s41598-017-07618-6.
- [64] S.-H. Hsu, "Signal power tapped with low polarization dependence and insensitive wavelength on silicon-on-insulator platforms," *J. Opt. Soc. Am. B*, vol. 27, no. 5, pp. 941–947, May 2010, doi: 10.1364/JOSAB.27.000941.
- [65] H. Yun, L. Chrostowski, and N. A. F. Jaeger, "Ultra-broadband 2  $\times$  2 adiabatic 3 dB coupler using subwavelength-grating-assisted silicon-on-insulator strip waveguides," *Opt. Lett.*, vol. 43, no. 8, pp. 1935–1938, Apr. 2018, doi: 10.1364/OL.43.001935.
- [66] Z. Zhang, X. Hu, and J. Wang, "On-chip optical mode exchange using tapered directional coupler," *Sci Rep*, vol. 5, no. 1, p. 16072, 2015, doi: 10.1038/srep16072.
- [67] Y. Ding, J. Xu, F. Da Ros, B. Huang, H. Ou, and C. Peucheret, "On-chip two-mode division multiplexing using tapered directional coupler-based mode multiplexer and demultiplexer," *Opt. Express*, vol. 21, no. 8, pp. 10376–10382, Apr. 2013, doi: 10.1364/OE.21.010376.
- [68] J. Chen and Y. Shi, "An Ultracompact Silicon Triplexer Based on Cascaded Bent Directional Couplers," *J. Lightwave Technol.*, vol. 35, no. 23, pp. 5260–5264, Dec. 2017, [Online]. Available: <https://opg.optica.org/jlt/abstract.cfm?URI=jlt-35-23-5260>
- [69] J. Chen, "A broadband wavelength demultiplexer assisted by SWG-based directional couplers," *Optik (Stuttg)*, vol. 202, p. 163602, 2020, doi: <https://doi.org/10.1016/j.ijleo.2019.163602>.
- [70] M. S. Rouified *et al.*, "Ultra-compact MMI-based beam splitter demultiplexer for the NIR/MIR wavelengths of 1.55  $\mu\text{m}$  and 2  $\mu\text{m}$ ," *Opt Express*, vol. 25 10, pp. 10893–10900, 2017, [Online]. Available: <https://api.semanticscholar.org/CorpusID:30530670>
- [71] N. Bin and J. Xiao, "Ultracompact silicon-based wavelength diplexer for 1.55/2  $\mu\text{m}$  using subwavelength gratings," *Opt Lett*, vol. 44, pp. 2775–2778, Apr. 2019, doi: 10.1364/OL.44.002775.
- [72] J. Zhang *et al.*, "High-Extinction-Ratio and Compact 1310/1550 nm Wavelength Diplexer on SOI Platform Based on an SWG-Structured Two-Mode Interference Coupler," *IEEE Photonics J*, vol. 14, no. 2, pp. 1–6, 2022, doi: 10.1109/JPHOT.2022.3149998.

- [73] L. Liu, Q. Deng, and Z. Zhou, "An Ultra-Compact Wavelength Diplexer Engineered by Subwavelength Grating," *IEEE Photonics Technology Letters*, vol. 29, no. 22, pp. 1927–1930, 2017, doi: 10.1109/LPT.2017.2743109.
- [74] H. Xu and Y. Shi, "On-Chip Silicon Triplexer Based on Asymmetrical Directional Couplers," *IEEE Photonics Technology Letters*, vol. 29, no. 15, pp. 1265–1268, 2017, doi: 10.1109/LPT.2017.2721738.
- [75] W.-P. Huang, "Coupled-mode theory for optical waveguides: an overview," *J. Opt. Soc. Am. A*, vol. 11, no. 3, pp. 963–983, Mar. 1994, doi: 10.1364/JOSAA.11.000963.
- [76] B. Saleh and M. Teich, *Fundamentals of Photonics, 3rd Edition*. 2019.
- [77] "Guided-Wave Optics," in *Fundamentals of Photonics*, John Wiley & Sons, Ltd, 1991, ch. 7, pp. 238–271. doi: <https://doi.org/10.1002/0471213748.ch7>.
- [78] A. Thottoli *et al.*, "Highly efficient and selective integrated directional couplers for multigas sensing applications," *Sci Rep*, vol. 13, no. 1, p. 22720, 2023, doi: 10.1038/s41598-023-49889-2.
- [79] Y. Fu, T. Ye, W. Tang, and T. Chu, "Efficient adiabatic silicon-on-insulator waveguide taper," *Photon. Res.*, vol. 2, no. 3, pp. A41–A44, Jun. 2014, doi: 10.1364/PRJ.2.000A41.
- [80] A. R. Nelson, "Coupling optical waveguides by tapers," *Appl. Opt.*, vol. 14, no. 12, pp. 3012–3015, Dec. 1975, doi: 10.1364/AO.14.003012.
- [81] G. Kurczveil, P. Pintus, M. J. R. Heck, J. D. Peters, and J. E. Bowers, "Characterization of Insertion Loss and Back Reflection in Passive Hybrid Silicon Tapers," *IEEE Photonics J*, vol. 5, no. 2, p. 6600410, 2013, doi: 10.1109/JPHOT.2013.2246559.
- [82] L. O'Faolain *et al.*, "Hybrid lasers using CMOS compatible nanostructures," *2019 IEEE 8th International Conference on Advanced Optoelectronics and Lasers (CAOL)*, pp. 1–4, 2019.
- [83] J. Li, L. O'Faolain, S. A. Schultz, and T. F. Krauss, "Low loss propagation in slow light photonic crystal waveguides at group indices up to 60," *Photonics Nanostruct*, vol. 10, no. 4, pp. 589–593, 2012, doi: <https://doi.org/10.1016/j.photonics.2012.05.006>.
- [84] G. Menduni *et al.*, "Fiber-Coupled Quartz-Enhanced Photoacoustic Spectroscopy System for Methane and Ethane Monitoring in the Near-Infrared Spectral Range," *Molecules*, vol. 25, no. 23, 2020, doi: 10.3390/molecules25235607.
- [85] K. Ahmed, M. J. Haque, M. A. Jabin, B. K. Paul, I. S. Amiri, and P. Yupapin, "Tetra-core surface plasmon resonance based biosensor for alcohol sensing," *Physica B Condens Matter*, vol. 570, pp. 48–52, Oct. 2019, doi: 10.1016/J.PHYSB.2019.05.047.
- [86] K. Ahmed, B. K. Paul, F. Ahmed, M. A. Jabin, and M. S. Uddin, "Numerical demonstration of triangular shaped photonic crystal fibre-based biosensor in the Terahertz range," *IET Optoelectronics*, vol. 15, no. 1, pp. 1–7, Feb. 2021, doi: 10.1049/OTE2.12006.
- [87] M. M. Bilal, S. López-Aguayo, M. Szczerska, and H. A. Madni, "Multi-functional sensor based on photonic crystal fiber using plasmonic material and magnetic fluid," *Appl. Opt.*, vol. 61, no. 35, pp. 10400–10407, Dec. 2022, doi: 10.1364/AO.456519.
- [88] B. K. Paul *et al.*, "The design and analysis of a dual-diamond-ring PCF-based sensor," *J Comput Electron*, vol. 19, no. 3, pp. 1288–1294, 2020, doi: 10.1007/s10825-020-01509-2.

- [89] L. Liu, Z. Liu, Y. Zhang, and S. Liu, "Side-Polished D-Type Fiber SPR Sensor for RI Sensing With Temperature Compensation," *IEEE Sens J*, vol. 21, no. 15, pp. 16621–16628, 2021, doi: 10.1109/JSEN.2021.3080290.
- [90] M. M. Bilal, S. Lopez-Aguayo, and A. Thottoli, "Numerical Analysis of Solid-Core Photonic Crystal Fiber Based on Plasmonic Materials for Analyte Refractive Index Sensing," *Photonics*, vol. 10, no. 10, 2023, doi: 10.3390/photonics10101070.
- [91] D. Li, W. Zhang, H. Liu, J. Hu, and G. Zhou, "High Sensitivity Refractive Index Sensor Based on Multicoating Photonic Crystal Fiber With Surface Plasmon Resonance at Near-Infrared Wavelength," *IEEE Photonics J*, vol. 9, no. 2, pp. 1–8, 2017, doi: 10.1109/JPHOT.2017.2687121.
- [92] R. Yu, Y. Chen, L. Shui, and L. Xiao, "Hollow-Core Photonic Crystal Fiber Gas Sensing," *Sensors*, vol. 20, no. 10, 2020, doi: 10.3390/s20102996.
- [93] W. Jin *et al.*, "Highly sensitive temperature sensing probes based on liquid cladding elliptical micro/nanofibers," *Opt. Express*, vol. 28, no. 14, pp. 20062–20073, Jul. 2020, doi: 10.1364/OE.393491.
- [94] N. Luan, R. Wang, W. Lv, and J. Yao, "Surface plasmon resonance sensor based on D-shaped microstructured optical fiber with hollow core," *Opt. Express*, vol. 23, no. 7, pp. 8576–8582, Apr. 2015, doi: 10.1364/OE.23.008576.
- [95] R. Xu *et al.*, "An All-Optical Vector Magnetic Field Sensor Based on Magnetic Fluid and Side-Polished Hollow-Core Optical Fiber," *IEEE Sens J*, vol. 21, no. 19, pp. 21410–21416, 2021, doi: 10.1109/JSEN.2021.3092216.
- [96] S. F. A. Z. Yusoff, C. S. Lim, S. R. Azzuhri, H. Ahmad, and R. Zakaria, "Studies of Ag/TiO<sub>2</sub> plasmonics structures integrated in side polished optical fiber used as humidity sensor," *Results Phys*, vol. 10, pp. 308–316, 2018, doi: <https://doi.org/10.1016/j.rinp.2018.06.008>.
- [97] C. F. Twomey *et al.*, "Evanescent wave quartz-enhanced photoacoustic spectroscopy employing a side-polished fiber for methane sensing," *Photoacoustics*, vol. 36, p. 100586, 2024, doi: <https://doi.org/10.1016/j.pacs.2024.100586>.
- [98] A. Patnaik and K Senthilnathan, "Graphene-based conducting metal oxide coated D-shaped optical fiber SPR sensor," *IEEE Photonics Technology Letters*, vol. 27, no. 23, pp. 2437–2440, 2015.
- [99] X. Wang, X. Wang, H. Deng, and L. Yuan, "Ultra-high sensitivity SPR temperature sensor based on a helical-core fiber," *Opt Express*, vol. 29, no. 14, pp. 22417–22426, 2021, doi: 10.1364/OE.428199.
- [100] S. Yusoff, C. Lim, S. Azzuhri, H. Ahmad, and R Zakaria, "Studies of Ag/TiO<sub>2</sub> plasmonics structures integrated in side polished optical fiber used as humidity sensor," *Results in Physics*, vol. 10, pp. 308–316, 2018.
- [101] R. Xu, G. Niu, Y. Xue, C. Ke, H. Deng, and S Deng, "An All-Optical Vector Magnetic Field Sensor Based on Magnetic Fluid and Side-Polished Hollow-Core Optical Fiber," *IEEE Sensors Journal*, vol. 21, no. 19, pp. 21410–21416, 2021.
- [102] J. Tang *et al.*, "All-fiber-optic VOC gas sensor based on side-polished fiber wavelength selectively coupled with cholesteric liquid crystal film," *Sens Actuators B Chem*, vol. 273, pp. 1816–1826, 2018, doi: 10.1016/J.SNB.2018.06.105.

- [103] C. Teng *et al.*, “Side-Polish Plastic Optical Fiber Based SPR Sensor for Refractive Index and Liquid-Level Sensing,” *Sensors*, vol. 22, no. 16, p. 6241, 2022, doi: 10.3390/s22166241.
- [104] J. Yang *et al.*, “High sensitivity humidity sensor based on gelatin coated side-polished in-fiber directional coupler,” *Sens Actuators B Chem*, vol. 305, p. 127555, 2020, doi: 10.1016/J.SNB.2019.127555.
- [105] V. Matějček, M. Chomát, M. Pospíšilová, M. Hayer, and I. Kašík, “Optical fiber with novel geometry for evanescent-wave sensing,” *Sens Actuators B Chem*, vol. 29, no. 1, pp. 416–422, 1995, doi: [https://doi.org/10.1016/0925-4005\(95\)01717-8](https://doi.org/10.1016/0925-4005(95)01717-8).
- [106] G. Pandraud, T. M. Koster, C. Gui, M. Dijkstra, A. van den Berg, and P. V Lambeck, “Evanescent wave sensing: new features for detection in small volumes,” *Sens Actuators A Phys*, vol. 85, no. 1, pp. 158–162, 2000, doi: [https://doi.org/10.1016/S0924-4247\(00\)00367-8](https://doi.org/10.1016/S0924-4247(00)00367-8).
- [107] Z. Li *et al.*, “Infrared Evanescent Wave Sensing Based on a Ge<sub>10</sub>As<sub>30</sub>Se<sub>40</sub>Te<sub>20</sub> Fiber for Alcohol Detection,” *Sensors*, vol. 23, no. 10, 2023, doi: 10.3390/s23104841.
- [108] D. Sanchez. Lopez, “ELEMENTS OF PHOTONICS,” vol. Volume II..
- [109] K. Kinjalk *et al.*, “Highly selective and sensitive detection of volatile organic compounds using long wavelength InAs-based quantum cascade lasers through quartz-enhanced photoacoustic spectroscopy,” *Appl Phys Rev*, vol. 11, no. 2, p. 021427, Jun. 2024, doi: 10.1063/5.0189501.
- [110] A. Zifarelli *et al.*, “All-fiber-coupled mid-infrared quartz-enhanced photoacoustic sensors,” *Opt Laser Technol*, vol. 176, p. 110926, 2024, doi: <https://doi.org/10.1016/j.optlastec.2024.110926>.
- [111] R. B. Skeie, Ø. Hodnebrog, and G. Myhre, “Trends in atmospheric methane concentrations since 1990 were driven and modified by anthropogenic emissions,” *Commun Earth Environ*, vol. 4, no. 1, p. 317, 2023, doi: 10.1038/s43247-023-00969-1.
- [112] Y. Chen, T. Liang, S. Qiao, Y. He, and Y. Ma, “Highly sensitive detection of methane based on LITES and H-LITES techniques,” *Infrared Phys Technol*, vol. 140, p. 105370, 2024, doi: <https://doi.org/10.1016/j.infrared.2024.105370>.
- [113] A. Zifarelli *et al.*, “Methane and ethane detection from natural gas level down to trace concentrations using a compact mid-IR LITES sensor based on univariate calibration,” *Photoacoustics*, vol. 29, p. 100448, 2023, doi: <https://doi.org/10.1016/j.pacs.2023.100448>.
- [114] D. R. Rivera, C. M. Brown, D. G. Ouzounov, W. W. Webb, and C. Xu, “Use of a lensed fiber for a large-field-of-view, high-resolution, fiber-scanning microendoscope,” *Opt. Lett.*, vol. 37, no. 5, pp. 881–883, Mar. 2012, doi: 10.1364/OL.37.000881.
- [115] J. Song, HarendraN. J. Fernando, B. Roycroft, B. Corbett, and F. H. Peters, “Practical Design of Lensed Fibers for Semiconductor Laser Packaging Using Laser Welding Technique,” *J. Lightwave Technol.*, vol. 27, no. 11, pp. 1533–1539, Jun. 2009, [Online]. Available: <https://opg.optica.org/jlt/abstract.cfm?URI=jlt-27-11-1533>
- [116] Z. Hu, J. Wang, and J. Liang, “Manipulation and arrangement of biological and dielectric particles by a lensed fiber probe,” *Opt. Express*, vol. 12, no. 17, pp. 4123–4128, Aug. 2004, doi: 10.1364/OPEX.12.004123.
- [117] L. S. Rothman *et al.*, “The HITRAN2012 molecular spectroscopic database,” *J Quant Spectrosc Radiat Transf*, vol. 130, pp. 4–50, 2013, doi: <https://doi.org/10.1016/j.jqsrt.2013.07.002>.

- [118] Y. He *et al.*, “Long distance, distributed gas sensing based on micro-nano fiber evanescent wave quartz-enhanced photoacoustic spectroscopy,” *Appl Phys Lett*, vol. 111, no. 24, p. 241102, Dec. 2017, doi: 10.1063/1.5003121.
- [119] G. Maire *et al.*, “High efficiency silicon nitride surface grating couplers,” *Opt Express*, vol. 16, no. 1, p. 328, 2008, doi: 10.1364/OE.16.000328.
- [120] J. Hong, A. M. Spring, F. Qiu, and S. Yokoyama, “A high efficiency silicon nitride waveguide grating coupler with a multilayer bottom reflector,” *Sci Rep*, vol. 9, no. 1, p. 12988, Sep. 2019, doi: 10.1038/s41598-019-49324-5.
- [121] M. De Carlo, G. Menduni, A. Sampaolo, F. De Leonardis, V. Spagnolo, and V. M. N. Passaro, “Modeling and Design of a Semi-Integrated QEPAS Sensor,” *Journal of Lightwave Technology*, vol. 39, no. 2, pp. 646–653, Jan. 2021, doi: 10.1109/JLT.2020.3030682.
- [122] D. Marcuse, “Length optimization of an S-shaped transition between offset optical waveguides,” *Appl Opt*, vol. 17, no. 5, p. 763, Mar. 1978, doi: 10.1364/AO.17.000763.
- [123] I. E. Gordon *et al.*, “The HITRAN2020 molecular spectroscopic database,” *J Quant Spectrosc Radiat Transf*, vol. 277, p. 107949, Jan. 2022, doi: 10.1016/j.jqsrt.2021.107949.
- [124] M. Olivieri *et al.*, “Influence of Air Pressure on the Resonance Properties of a T-Shaped Quartz Tuning Fork Coupled with Resonator Tubes,” *Applied Sciences*, vol. 11, no. 17, 2021, doi: 10.3390/app11177974.
- [125] H. Lin *et al.*, “Ppb-level gas detection using on-beam quartz-enhanced photoacoustic spectroscopy based on a 28 kHz tuning fork,” *Photoacoustics*, vol. 25, p. 100321, 2022, doi: <https://doi.org/10.1016/j.pacs.2021.100321>.
- [126] F. Ahmed *et al.*, “Monitoring of Carbon Dioxide Using Hollow-Core Photonic Crystal Fiber Mach-Zehnder Interferometer,” *Sensors*, vol. 19, no. 15, 2019, doi: 10.3390/s19153357.
- [127] Q. Nie *et al.*, “Review on Hollow-Core Fiber Based Multi-Gas Sensing Using Raman Spectroscopy,” *Photonic Sensors*, vol. 14, no. 4, p. 240412, 2024, doi: 10.1007/s13320-024-0730-4.
- [128] Y. Saito, T. Kanaya, A. Nomura, and T. Kano, “Experimental trial of a hollow-core waveguide used as an absorption cell for concentration measurement of NH<sub>3</sub> gas with a CO<sub>2</sub> laser,” *Opt. Lett.*, vol. 18, no. 24, pp. 2150–2152, Dec. 1993, doi: 10.1364/OL.18.002150.
- [129] F. Benabid, J. C. Knight, G. Antonopoulos, and P. St. J. Russell, “Stimulated Raman Scattering in Hydrogen-Filled Hollow-Core Photonic Crystal Fiber,” *Science (1979)*, vol. 298, no. 5592, pp. 399–402, 2002, doi: 10.1126/science.1076408.
- [130] R. Bicknell *et al.*, “Fabrication and characterization of hollow metal waveguides for optical interconnect applications,” *Applied Physics A*, vol. 95, no. 4, pp. 1059–1066, 2009, doi: 10.1007/s00339-009-5206-2.
- [131] T. Miura, F. Koyama, and A. Matsutani, “Modeling and Fabrication of Hollow Optical Waveguide for Photonic Integrated Circuits,” *Jpn J Appl Phys*, vol. 41, no. 7S, p. 4785, Jul. 2002, doi: 10.1143/JJAP.41.4785.
- [132] R. Bernini, S. Campopiano, and L. Zeni, “Silicon micromachined hollow optical waveguides for sensing applications,” *IEEE Journal of Selected Topics in Quantum Electronics*, vol. 8, pp. 106–110, 2002, [Online]. Available: <https://api.semanticscholar.org/CorpusID:122766155>

- [133] D. Yin, H. Schmidt, J. P. Barber, and A. R. Hawkins, "Integrated ARROW waveguides with hollow cores," *Opt. Express*, vol. 12, no. 12, pp. 2710–2715, Jun. 2004, doi: 10.1364/OPEX.12.002710.
- [134] G. Quaranta, G. Basset, O. J. F. Martin, and B. Gallinet, "Recent Advances in Resonant Waveguide Gratings," *Laser Photon Rev*, vol. 12, no. 9, p. 1800017, 2018, doi: <https://doi.org/10.1002/lpor.201800017>.
- [135] S. S. Wang and R. Magnusson, "Theory and applications of guided-mode resonance filters," *Appl. Opt.*, vol. 32, no. 14, pp. 2606–2613, May 1993, doi: 10.1364/AO.32.002606.
- [136] S. Geschwindner, J. F. Carlsson, and W. Knecht, "Application of Optical Biosensors in Small-Molecule Screening Activities," *Sensors*, vol. 12, no. 4, pp. 4311–4323, 2012, doi: 10.3390/s120404311.
- [137] H. N. Daghestani and B. W. Day, "Theory and Applications of Surface Plasmon Resonance, Resonant Mirror, Resonant Waveguide Grating, and Dual Polarization Interferometry Biosensors," *Sensors*, vol. 10, no. 11, pp. 9630–9646, 2010, doi: 10.3390/s101109630.
- [138] Y. Fang, "Label-Free Cell-Based Assays with Optical Biosensors in Drug Discovery," *Assay Drug Dev Technol*, vol. 4, no. 5, pp. 583–595, 2006, doi: 10.1089/adt.2006.4.583.
- [139] R. De Palo *et al.*, "Quartz-Enhanced Photoacoustic Sensors for Detection of Eight Air Pollutants," *Adv Photonics Res*, vol. 4, no. 6, p. 2200353, 2023, doi: <https://doi.org/10.1002/adpr.202200353>.
- [140] G. Menduni *et al.*, "Measurement of methane, nitrous oxide and ammonia in atmosphere with a compact quartz-enhanced photoacoustic sensor," *Sens Actuators B Chem*, vol. 375, p. 132953, 2023, doi: <https://doi.org/10.1016/j.snb.2022.132953>.
- [141] I. Y. Abe, A. Mazzeo, A. S. Ferlauto, M. I. Alayo, and E. G. Melo, "Inverse design of distributed bragg reflector targeting a sharp reflectivity spectrum," *Photonics Nanostruct*, vol. 57, p. 101183, 2023, doi: <https://doi.org/10.1016/j.photonics.2023.101183>.
- [142] G. Wachter *et al.*, "Silicon microcavity arrays with open access and a finesse of half a million," *Light Sci Appl*, vol. 8, no. 1, p. 37, 2019, doi: 10.1038/s41377-019-0145-y.
- [143] H. Cao *et al.*, "Laser dicing of semiconductor wafers: Research status and current challenges," *Opt Lasers Eng*, vol. 186, p. 108786, 2025, doi: <https://doi.org/10.1016/j.optlaseng.2024.108786>.
- [144] J. Hayden, M. Giglio, A. Sampaolo, V. Spagnolo, and B. Lendl, "Mid-infrared intracavity quartz-enhanced photoacoustic spectroscopy with pptv – Level sensitivity using a T-shaped custom tuning fork," *Photoacoustics*, vol. 25, p. 100330, 2022, doi: <https://doi.org/10.1016/j.pacs.2022.100330>.